UNIVERSITA' DEGLI STUDI DI NAPOLI "FEDERICO II"

Department of Chemical, Materials and Industrial Production Engineering

POLYTECHNIC AND BASIC SCIENCES SCHOOL

PhD in "Industrial Product and Process Engineering"

XXXI cycle

Photo-responsive oil core based polymer nanocapsules

Supervision:

Prof. Dr. Paolo Antonio Netti

Advisor:

Dr. Ing. Raffaele Vecchione

Coordinator:

Prof. Giuseppe Mensitieri

PhD student:

Chiara Di Cicco

Academic year 2017/2018

Table of Contents.

Chapter 1

State of art

1.1 Nanomedicine: O/W drug delivery systems

The application of nanotechnology to clinical treatments brings to the birth of nanomedicine. Nanomedicine's main aims are early diagnostics and targeted therapies in several human diseases, such as cancer therapy.[1] The fusion between nanotechnology and biomedicine developed novel materials with highly specific and unique therapeutic properties. Compared to traditional therapies, nanotechnology devices offer new advantages, such as targeted delivery, controlled drug release, and improvement of cell barrier crossing.[2,3]

Over the past decades, nanotechnology world, engineering nano-scaled devices, has led to the development of a lot of particle systems, such as gold nanoparticles (NPs), silica NPs, liposomes, and polymeric NPs. Drug delivery systems' aim is to obtain a particle design to improve drug specificity to the desired site of action, so higher efficacy and fewer adverse effects.[4] In fact, literature strongly underlines that the use of polymeric nanocarriers to transport active compounds like small-molecular drugs, peptides, or genes found an increased attention throughout the different fields of natural sciences. Not only these nanocarriers enhance the properties of already existing drugs in terms of solubility, bioavailability, and prolonged circulation times, furthermore they can be tailor-made in such a manner that they selectively release their cargo at the desired site of action.[3,5] It is known that thanks to drugs' encapsulation, we can protect not only the cargo but also the living cells from the possible toxic effect of cargo. So we insist on the fact that nanomedicine could contribute with appropriated biocompatible multifunctional systems, to avoid these unwished effects. Structured nano-devices are able to navigate into living cells and can be activated for the local release of their cargo, increasing drug's bioavailability too.[2,6]

In the early 1990s, Decher and co-workers were the first to develop Layer-by-Layer (LbL) thin films (Figure 1.1).[1] Their protocol consists in the preparation of multilayer ultrathin organic films by alternated deposition of oppositely charged polyelectrolytes on a charged solid subrate. So this technique is based on the electrostatic attractions polyanions and polycations. One of the advantages of LbL films is that the film thickness can be precisely tuned at the nanometer level by changing the number of deposited layers.[2,4,7] In 1998, LbL technique was transferred from planar films to spherical colloidal particles by Donath and co-workers, referring to the strategy on planar substrate.[1] Since their introduction in 1998, LbL capsules have obtained an increasing interest, largely because of the possibility to tailor their properties, such as size, composition, porosity, stability, surface functionality, colloidal stability (Figure 1.2). In addition, the LbL technique has a special protocol which enables to engineer new materials introducing unprecedented structure and function.[3] The variety of templates and materials has given rise to an ever-expanding catalogue of LbL-assembled multi-layered particles varying in sizes, shapes, and chemical compositions. A main feature of the

LbL technique is the precision of the final particles. Thanks to such versatility, multilayered particles have become a powerful platform for drug encapsulation and triggered drug release.[4]

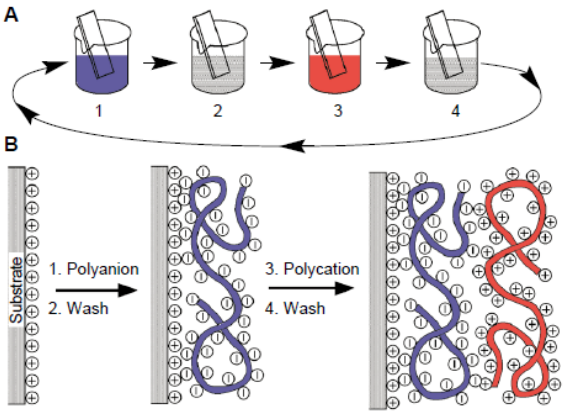

Figure 1.1. (A) Schematic of the film deposition process. Steps 1 and 3 represent the adsorption of a polyanion and polycation, respectively, and steps 2 and 4 are washing steps. The four steps are the basic sequence for the simplest film architecture. (B) Simplified molecular picture "model" of the first two adsorption steps, starting with a positively charged substrate. Counter ions are omitted for clarity.[8]

The LbL NPs were first reported by Caruso and his group. In their protocol they prepared via LbL some polyelectrolyte nanocapsules around a solid template, when obtained monodisperse emulsions by filling them with oil.[9,10] So more in general, LbL technology is about polymeric nanocapsules and takes advantage of the charge–charge interaction between substrate and monolayers of polyelectrolytes to create multiple layered nano-architecture held together by electrostatic forces. The formation of LbL systems are attributed to electrostatic interactions, hydrogen bonding, hydrophobic interactions and van der Waals forces.[5]

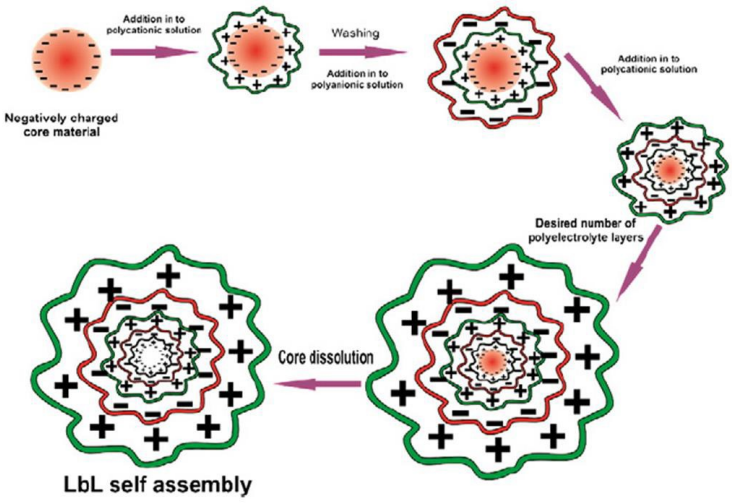

Figure 1.2. Example of layer by layer adsorption of two or more oppositely charged polyelectrolyte.[11]

In 2014, our team developed biodegradable oil-in-water (O/W) nano-emulsions coated with a molecular layer of biodegradable polyelectrolytes. In dependence of the polymer concentration, they controlled the level of coating that resulted in a tunable stability. Our O/W nano-emulsions consists of a biocompatible formulation: small lipidic droplets with soybean oil and Lipoid E80 lecithin dispersed in an aqueous medium. They have the ability to dissolve large quantities of hydrophobic drugs and protect their cargo from hydrolysis and enzymatic degradation. The stability over time and good behaviour of these systems, strictly connected to their monodisperisity, were obtained using a high-pressure homogenizer.[10] In 2016, a protocol to obtain optimized liquid–liquid interfaces capable to sustain multiple depositions of biodegradable polymers has also been developed in our lab. With this protocol, it was possible to perform around the oil core of the nanoemulsions, progressive depositions of the natural polymers shells via the classical LbL technique but with control almost at the molecular scale (Figure 1.3).[12]

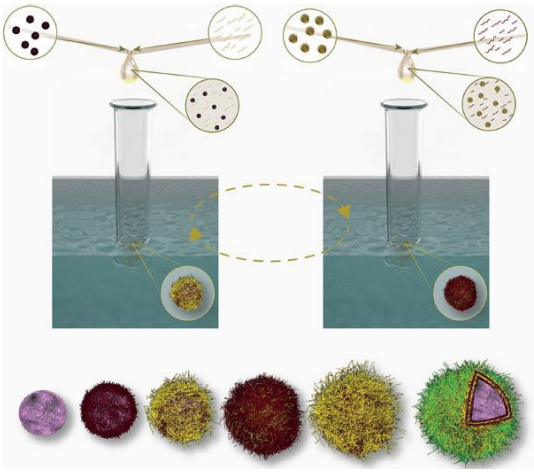

Figure 1.3. Example of controlled deposition of polymeric multilayer film on oil core based nanocapsules.[12]

In drug delivery field, from a circulation point of view, another important point, respected by our formulations, is that the ideal size of drug carriers is in a range below 200 nm.[6,10] In fact, bigger capsules can obstruct the smallest blood capillaries and cannot reach the specific tissue.[6] On the other hand, the selective delivery of a drug loaded nanocapsule through systemic administration routes is often attributed to passive targeting *via* the "enhanced permeability and retention" (EPR) effect which is mainly a molecular size-based phenomenon (Figure 1.4). This EPR effect is the basis for development of macromolecular anticancer therapy which was first introduced by Matsumura and Maeda in 1986. They showed that most solid tumors have blood vessels with defective architecture. This effect is attributed to poor tumor vascularization and lymphatic drainage. So most solid tumors exhibit enhanced vascular permeability, which will ensure a sufficient supply of nutrients and oxygen to tumor tissues for rapid growth. The EPR effect is a unique anatomical–pathophysiological nature

of tumor blood vessels that facilitates transport of macromolecules into tumor tissues. In this way the nanocapsules manage to accumulate themselves within the tumor tissue. In contrast, this EPR effect-driven drug delivery does not occur in normal tissues.[4,13]

In addition to passive targeting, recent studies have demonstrated that cell selectivity *in vitro* can be improved conjugating targeting ligands to multilayer nanoparticles. This is called "active" targeting, because to promote specific interaction, nanocapsules can be decorated with functional ligands which recognize the tumor tissue, to delivery and release their drug selectively. This strategy can be an effective approach to complement the EPR effect.[4] More in general, surface modifications are helpful not only to deliver the nanocapsules in specific sites but also to prevent the body from recognizing the capsules as foreign material.[3]

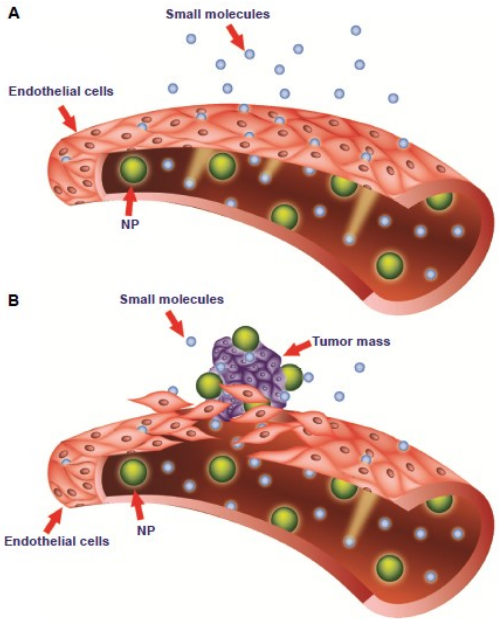

Figure 1.4. Targeting of nanomedicines by the enhanced permeability and retention (EPR) effect. Notes: (A) normal and (B) tumor vessels.[14]

For all said above, LbL polyelectrolytes deposition on nanoemulsion has emerged as one of the best techniques to deposit ultrathin polymer layers. However, it is known that electrostatic interactions are weak and easily breakable in physiological environment.[15] To improve emulsion stability a strategy is the cross-linking between the polymer shells by click chemistry.[10,16] In a previous work of our group, it has been shown that the stability of biopolymer multilayers (glycol chitosan and heparin) obtained *via* layer by layer can be enhanced introducing a covalent bonds among layers by means of a metal catalyst-free, light initiated 'click' reaction, namely the thiol-ene reaction. In particular, the reaction involves a thiol moiety on glycol chitosan and an allylic moiety on heparin. Interestingly, the reaction resulted effective even without a photoinitiator, mainly due to the high degree of

modification of the biopolymers, proving a completely non-cytotoxic final product (Figure 1.5). Cross-linked multilayers resulted in more stable systems than those stabilized with just electrostatic forces. In addition, the application of this approach to biopolymers surrounding an O/W nanoemulsion demonstrated that thiol-ene cross-linkage can be nicely exploited in the field of completely biocompatible and biodegradable nanocarriers.[15]

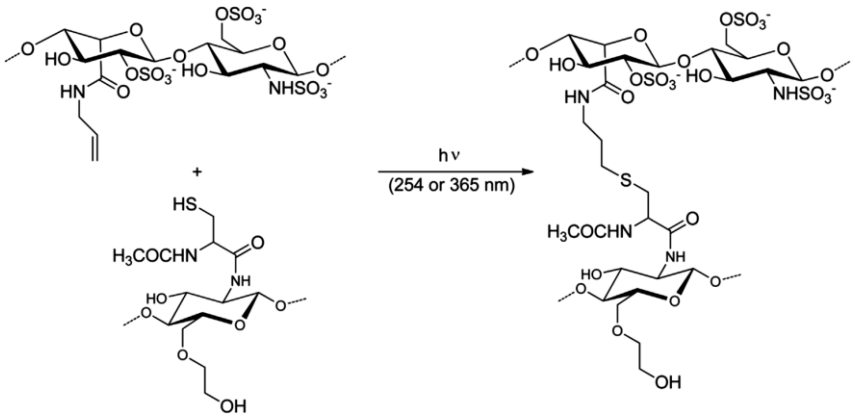

Figure 1.5. Thiol-ene reaction between allylated heparin and thiolated glycol chitosan. Reaction was triggered throughout UV irradiation.[15]

1.2 Endogenous and exogenous stimuli-responsive nanocarriers.

Conventional chemotherapy is far from successful because of the lack of tumor selectivity, or toxicity of the drugs. So it is of extreme importance the development of highly selective systems for tumors, to reduce drug toxicity and enhance the therapeutic purpose.[13,17] We have just discussed above about the EPR effect-based drug delivery connected to pathophysiological heterogeneity of the tumors. However, EPR effect is absent in the central area of metastatic cancers, and so there the accumulation is lower than in other parts.[13]

Considering the difference between normal and pathological tissues, the design of stimuli-responsive nanocarriers is a promised approach for the future to improve the therapeutic effects in the tumor tissues and reduce the undesired ones in the healthy cells. The use of stimuli-responsive drug delivery nanocapsules could improve the cellular uptake and intracellular stability. According to the diagnostic or therapeutic purpose, these systems can include different organic and inorganic materials, such as polymers, liposomes, nanoemulsions, dendrimers and so on.[18]

In the 1970s stimuli-responsive drug delivery was introduced with the use of thermosensitive liposomes for a controlled release of drugs through hyperthermia. Since then, stimuli-responsive nanocarriers for drug delivery became of particular interest.[19]

About stimuli-responsive nanocarriers, Keun Sang Oh et.al. were the first to introduce LbL nanocarrier for cancer-targeting. First of all, the LbL approach improves the target ability by

prolonging the nanocarries systemic circulation.[20] LbL nanocapsules surface can be modified with the aim to prevent the recognition of these materials as foreign for the body and to deliver them to specific tissue by targeting. The application of micro-/nanocapsules as drug delivery vehicles shows great promise.[3]

The easy of the preparation process and the variety of applications in drug delivery have recognized the stimuli-sensitive LbL systems as a promising approach .[11]

Typically, stimuli-responsive mechanisms to release the drugs can be of two types (Figure 1.6): endogenous stimuli (e.g., pH, enzymes, redox potential, glucose concentration, ions) or exogenous stimuli (temperature, magnetic fields, electrical fields, ultrasound and light). The choice of release mechanism is connected to the desired application. Intracellular mechanisms are the basis of the endogenous stimuli mainly used to release the encapsulated drugs from biodegradable coated nanocarriers. Indeed, exogenous stimuli are mainly used for a remoted control of the opening of the nanocarries with external source.[1,3,6] Among the variety of nanocarriers, polyelectrolytes LbL systems is a powerful method because of their versatility in shape, size, modulated swelling capacity.[21]

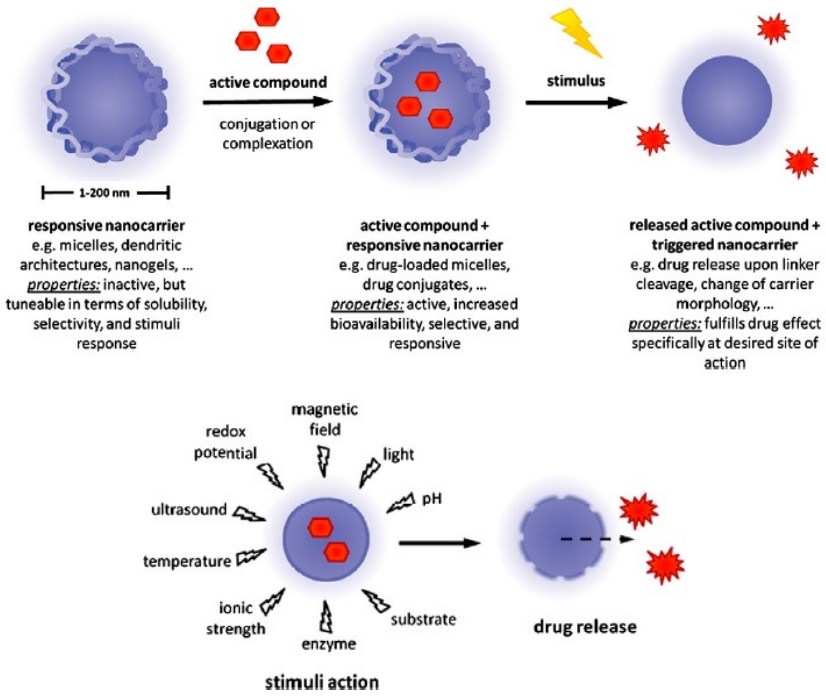

Figure 1.6. On top: General scheme of a stimuli-responsive nanocarrier for the transport of active compounds. On bottom: General scheme of stimuli-responsive release of a drug from a nanocarrier.[5]

Before introducing the nucleus of this PhD project, which is based on a photo-responsive LbL O/W nanoemulsion, we carry on a brief summary of the different stimuli.

pH stimuli-responsive systems. In these systems the triggering of the drugs is based on the different pH gradient between the tumor tissues (pH 5.7-6.8) and the extracellular environment (pH 7.4), and the acid pH of endosomal and lysosomal compartments.[18,22] So pH stimuli-responsive systems are based on pH sensitive polymeric materials. The change in pH environment lead to some changes in nanocapsules' permeability with the followed release of the drugs.[20] Typical pH-stimuli responsive polymers reported in literature include poly(acrylamide) (PAM), poly(acrylic acid) (PAA), poly(methacrylicacid) (PMAA), poly(diethylaminoethylmethacrylate) (PDEAEMA), poly(dimethylaminoethyl methacrylate) (PDMAEMA), polymers with phosphoric acid derivates, and some natural polymers such as albumin and gelatin.[17] An example for pH-responsive nanocarriers was reported by Liang et al. In their studies the capsules were based on poly(2-diisopropylaminoethyl methacrylate) (PDPA). They combined PDPA with a minor component of lauryl methacrylate ($PDPA_{C12}$). In this way they obtained the endocytic pH-induced degradation of their capsules. Their multilayers containing C12 groups in the PDPA increased the overall hydrophobicity, and so a non-covalent stabilization of the multilayers at pH 7.4. On the other hand, the capsules degraded for the cellular pH shift.[23]

Redox potential stimuli-responsive systems. Between the extracellular and intracellular compartments there is a different redox potential. In fact, the extracellular space is oxidative while the intracellular is reductive. This is due to the different concentration of glutathione (GSH) in these two compartments (~2–10 μM in the extracellular part and ~2–10 mM in the intracellular one) and in tumor tissues as compared to healthy ones.[5,18,19] So the release of the drug in the cytosol can be triggered by this different redox potential.[19] Since disulphide bonds can be cleavaged by reducing agent (GSH) and the thiol groups can return to disulphide by oxidation, it is possible to built redox-sensitive carriers by incorporating disulphide bonds which release the drug as a consequence of the redox potential triggering.[24] An example of redox potential stimuli-responsive nanocarrier was reported by Lee and co-workers. Their synthesized biocompatible polymer micelles with disulfide bonds in their shells responded to the typical reduced conditions of the cancer environment.[25]

Enzyme stimuli-responsive systems. In pathological states, such as cancer or inflammation, the expression of vary enzymes (e.g. protease, phospholipases or glycosidases) is altered. So in those sites, it is possible to design drug delivery systems acting via specific enzyme-mediation.[19,24] For example, literature studies demonstrated that esterases or proteases can promote the cleavage of esters or short peptide sequences contained in the enzyme-responsive nanocarriers.[5] Other examples of enzymes used for trigger are proteases, glucuronidase, or carboxylesterases, which are expressed differentially in the normal and tumor cells. To promote recognition of the nanocarriers by these

enzymes, specific enzyme substrates are encapsulated into the nanocarriers or linked to external segments containing the drugs and bonded to the nanocarriers.[5]

Ion stimuli-responsive systems. In the case that there are coordinative bonds between the nanocarrier and the guest, it is possible to trigger the release by competitive ligands or ions. For example, in literature, it was reported that micelles based on PEG-PAsp and PEG-PGlu and loaded with *cis* platin coordinated to the carboxyl groups in the core of the micelle, did not show release in absence of competitive ligands. Instead, in a phosphate buffered saline, 50% of *cis* platin was released after 24 h in the case of PEG-PAsp based micelles and after 72 h in the case of PEG-PGlu ones, this because chloride ions in the buffer were favorited ligands for *cis* platin than carboxyl groups.[5]

Glucose stimuli-responsive systems. The introduction of enzymes such as catalase (CAT) and glucose oxidase (GOx) in the nanocapsules brings to the development of glucose stimuli-responsive systems. Generally, as reported by Qi et. al., these nanocarriers were loaded with insulin and were assembled by LbL depositions. Their shells contained imine bonds. The treatment with a glucose solution caused the conversion of glucose to gluconic acid. In fact, Qi et al.in 2009 noticed that CAT/GOD in the shells interaction with the glucose solution was responsible of a pH reduction in the microenvironment, connected to H^+ production. In that acid conditions there was the cleavage of the imine bonds, an increase of capsules' permeability and so insulin release.[5,20]

Thermo stimuli-responsive systems. A thermosensitive polymer is characterized by a lower critical solution temperature (LCST) in aqueous solution. Such polymer is water soluble below its LCST and becomes water insoluble above that temperature.[18] The behaviour of thermosensitive polymers is generated by the balance of hydrophilic and hydrophobic moieties constituted the amphiphilic polymer chain. It is known that there is a higher temperature of 1-2°C in the tumor microenvironment than that of normal tissue. So when the thermos-stimuli-responsive nanocarrier is in the tumor tissue, its thermal responsive polymers change their phase form into a hydrophobic collapsed one with the consequent release of the drug.[24] For the past 20 years the study of hyperthermia to improve radiation or chemotherapy therapies, has grown. In addition, tumor cells exhibit more sensibility to heat-induced damage than normal cells. So for example, in different clinical studies, liposomes and nanoparticles containing iron oxide particles were used to localize the tumor tissue by the magnetic properties of the iron oxide and to heat the specific tissue. Another advantage of the thermo responsive drug delivery systems is the creation of micro-emboli in the tumor vasculature, the lower intake of oxygen and nutrients into the tumor mass.[18]

Magneto stimuli-responsive systems. A magnetic field can have different uses and provide different applications. A permanent magnetic field can be a magnetic guidance, an alternating magnetic field can increase temperature, or it is possible to have both the effects when both the strategies are

alternately used. So the same magnetic stimuli-responsive drug delivery system can be used for diagnostics and therapy within a single system (the so-called theranostic approach).[19] For example, in literature studies the magnetic control of permeability of the nanocapsules was obtained by the introduction of ferromagnetic gold-coated cobalt in nanocarriers' shells. Applying an oscillating magnetic fields, the rotation of the embedded nanoparticles caused the distortion of the nanocapsules' structure and so an increase of their permeability. In addition, for nanocapsules based on polyelectrolytes, lipid bilayers, and magnetic nanoparticles, a local heating could be induced by the magnetic field. This changes the membranes phase and brings to an easier release of the encapsulated drugs.[26] Lu et al. study is an example of magneto responsive drug delivery systems based on LbL assembly, where the magnetic field changed the permeability of the polyelectrolyte shells.[17] Hu et al. studied LbL nanocapsules containing magnetic nanoparticles in their shells under a high-frequency magnetic field to trigger the release of the drug. They demonstrated that the magnetic field proved nanocavities in the shells and consequently the nanocapsules rupture.[11]

Electrical stimuli-responsive systems. When an electrical stimulus is applied to a charged drug or to polyelectrolyte multilayers, an influx of counterions and solvent molecule takes place. These influxes increase the osmotic pressure between the shells and so bring to a volumetric expansion. The osmotic pressure is balanced by polymers' deformation and swelling.[11,20] Electro-sensitive polymers are generally polyelectrolytes. Only few natural polymers show this behaviour in non-conducting media. Typically in such systems it is necessary the functionalization with charged or polarizable component which respond to an electric field. For example, a lightly cross-linked poly(dimethyl siloxane) gel containing electrosensitive colloidal TiO_2 particles was synthesized by Zrinyi and co-workers. TiO_2 particles were trapped in the matrix. So the gel deformation was obtained by the electrical force acting on these particles which was transferred to the polymer.[25]

Photo stimuli-responsive systems. Photo-responsive polymers present specific functional groups which are light sensitive. So upon light irradiation of appropriate wavelength, these polymers change their structural properties. An important aspect is that the use of light is a non-invasive mechanism. Some examples of photo stimuli-responsive groups incorporated into polymer structures are azobenzene, spiropyran, cinnamate, which present a light-induced isomerization behaviour. Other groups have a photo-labile behaviour, i.e. light cleavages them changing their polarity, such as some photo-labile esters.[25] Also metal nanoparticles, such as silver, platinum, gold and gold sulfide or magnetite are incorporated within polyelectrolyte multilayer capsule walls. These nanoparticles absorb light and dissipate adsorbed energy as heat. This behaviour causes irreversible changes in the shells integrity/permeability and capsules' shell rupture.[3,6,26] An example of photo stimuli-responsive polyelectrolyte capsules for a remote release of the encapsulated drugs is based on two different

components introduced into the polyelectrolyte shells. Either Ag nanoparticles or IR dyes adsorb light. Under laser illumination with a low-power near-infrared continuous-wave diode, the capsules containing Ag nanoparticles or IR dye were deformed or cut. In this way, with a remote control, there was the release of the encapsulated materials.[27] Being our systems based on a photo-stimuli linker, in the next paragraph we are going to deepen more this typology of stimuli-responsive nanocarriers.

Ultrasound stimuli-responsive systems. Ultrasound application in drug delivery is highly advantageous because it is non-invasive and has a good penetrating deep into the body. Moreover it can be focused and controlled by frequency, power, density, time of application and duty cycles.[17] Ultrasound mechanism is connected to the cavitation phenomena, which is activated by ultrasound. Cavitation is the alternating growth and shrinkage of microbubbles that means alternation of high and low pressure waves. When these microbubbles implode, generate local waves that perturb and can disrupt the polymeric shells of the capsules. Typical ultrasound stimuli-responsive polymeric systems are generally based on gels, polymeric micelles, LbL coated microbubbles. Moreover, cavitation and microbubble implosion can mediate enhancement of vessel permeability to facilitate the nanocarriers' encapsulation. This process is known as "sonoporation".[19,25] An example of ultrasound stimuli-responsive systems by Nelson et al. was based on micelles which released doxorubicin (Dox) upon application of low-frequency ultrasound in an *in vivo* rat model of a colon carcinoma. They demonstrated that ultrasound induced a selective release of doxorubicin at the tumor site providing a reduction of the tumor volume as compared to the noninsonated tumors.[28]

1.3 The *o*-nitrobenzyl ether as photocleavable linker.

The world of photo-cleavable linker and the research in this field have found a great interest in these years in particular when applied to drug delivery systems. Now, we wish to introduce the photo-cleavable linker which has been adopted in this project, but before, by appropriate examples, we want to explain better the world of photo-trigger molecules and systems describing the variety of photo-responsive linkers, their versatility, their fields of application and their advantages as shown in literatures.

First of all, as just said previously, the use of an external stimulus on drug delivery systems brings benefits such as protection of the drugs until they enter into the desired site and reduction of side effects. Among the external stimuli, light is of particular interest for its clinical relevance and the advantage to ensure a spatio-temporal control that enhance efficiency and minimize toxicity. The light-tissue interactions are mainly scattering and absorption, whose attenuate surface power density of the light beam. The attenuation coefficient and the penetration depth of light are inversely proportional where the attenuation coefficient depend from the absorption and scattering coefficients,

i.e. from the light wavelength and the type of tissue. Using NIR, penetration depth of light is in the order of centimetre scale. The penetration depth decreases going towards visible and UV light. Phototoxicity to tissues is connected to photochemical reaction or photothermal effects which are involved by the emission phenomena that rise when a tissue is irradiated. The maximum permissible exposure (MPE) depends on wavelengths and irradiation time. In general, even a photon of light can carry out a reaction through photo-responsive nanoparticles. Example of these photochemical reactions are: photo-isomerization, photo-cleavage, photo-crosslinking (Figure 1.7). These photochemical reactions can only be initiated by UV/vis radiation because of their higher energy but suffers from disadvantages like lower penetrating power. While lower wavelength radiations in NIR region have deeper penetration capabilities but are not energetic enough to initiate the reaction. The use of two-photon absorption is a strategy to combine the deeper penetration power of NIR and the high energy of UV/vis radiation to trigger chemical reaction. Photo-responsive groups, such as *o*-nitrobenzyl and coumarin, absorb two NIR photons which are converted in single UV/vis photons.[29,30] This could be a good opportunity since there are very few organic chromophores which absorb in NIR region, while the majority just responds to UV light.[31]

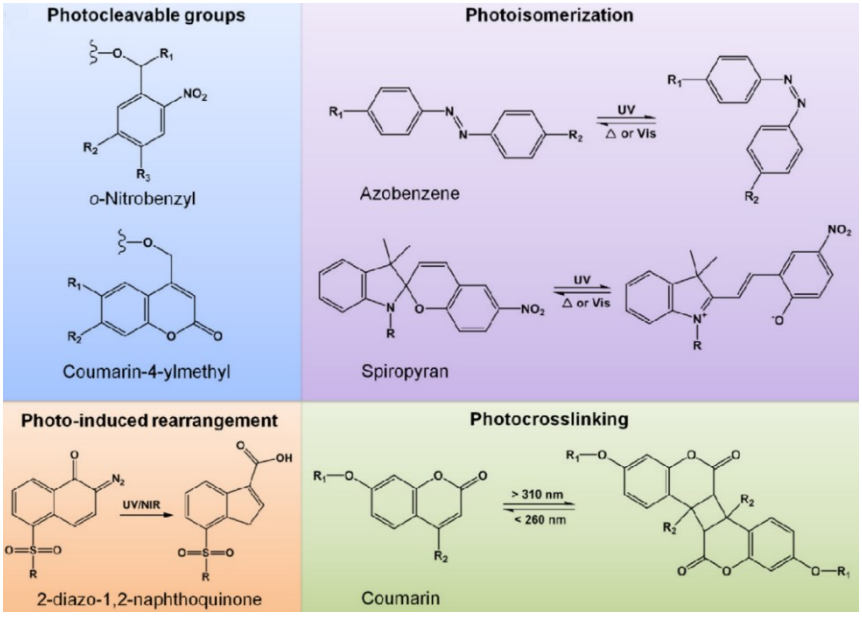

Figure 1.7. Examples of photo-responsive groups used in photochemical reactions, such as photo-cleavage, photo-isomerization, photo-induced rearrangement, and photo-crosslinking.[29]

Yan et al. demonstrated the multiphoton effect of core-shell lanthanide-doped upconverting nanoparticles (UCNPs) in a photosensitive hybrid hydrogel of biomedical interest. The UV light generated by the UCNPs induces the photo-cleavage of a photolinker present in the structure of the hydrogel, the *o*-nitrobenzyl moieties.[32,33] Another example of photodegradable hydrogels is formed

by the self-assembly of short peptides modified with a photo-responsive biaryl-substituted tetrazole moiety (Figure 1.8). This moiety, upon mild light irradiation, forms a fluorescent pyrazioline by a rapid intramolecular photoclick ligation. This photo intramolecular transformation, disturbing the system interaction, induces the disassembly of the hydrogel.[34]

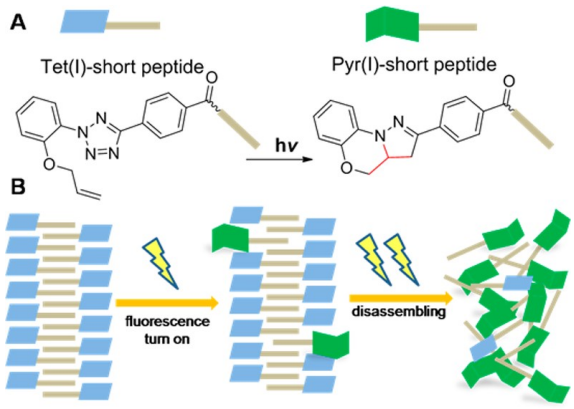

Figure 1.8. (A) Components of the photo-responsive hydrogel. (B) Photo-response mechanism.[34]

Also inorganic materials are used for photo-based applications, such as titanium oxide nanotubes, calcium phosphosilicate, nanoscintillators, copper selenide nanoparticles and silica-cored gold nanoparticles.[30] For example, a photo-responsive protein delivery system, studied by Luo and co-workers, used TiO_2 nanoparticles containing hydroxyl. They covalently attached hemoglobin onto the surface of TiO_2 nanoparticles by 3,4-dihydroxyl benzoic acid (DB). Visible light triggered the controlled release of Hb by the cleavage of the coordination bonds between DB and TiO_2 surfaces[24] Another example of photo-responsive linker used in drug delivery system was the perylene-3-ylmethanol (Figure 1.9). In biological studies, this linker contained in chlorambucil, nanoparticles exhibited good biocompatibility, cellular uptake and it was efficient in photo-responsive anticancer therapy. Perylene-3-ylmethyl is an efficient fluorescent photo-trigger for carboxylic acids and alcohols in aqueous media under visible light.[35]

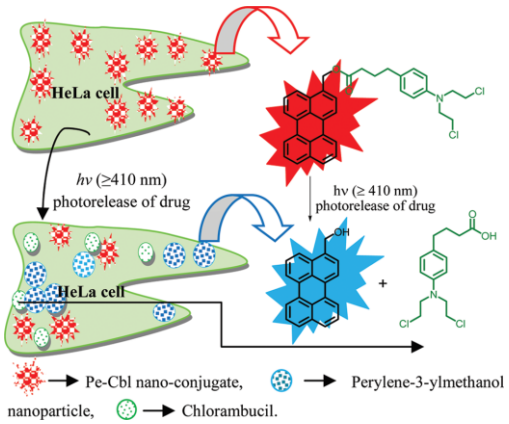

Figure 1.9. Photo-responsive nanoparticles containing perylene-chlorambucil moiety.[35]

In literature, they are also shown photo-responsive nano drug delivery system based on fluorescent carbon dots and a photo-responsive 7-methoxy quinoline moiety. In a work on HeLa cells, carbon dots were used for their fluorescence *in vitro* cellular imaging application, while quinolone for controlled photo-induced anticancer drug release upon both one-photon and two-photon excitation.[36] Some studies report examples of photo-responsive polymers introduced into nanocarriers. An examples is the bis(4-dimethylamino)phenylmethyl leucocyanide. Under UV irradiation it dissociates into ion pairs producing triphenyl methyl cations. The introduction of this photo-responsive linker in hydrogels brought to a swelling into the hydrogel via UV irradiation due to the formation of the cyanide ions after UV irradiation increasing the osmotic pressure within the gel.[17]

A widely used photo-responsive linker for its photo-isomerization property is azobene. Its *trans-cis* photo-triggered transition opens the possibility of a controlled release of the molecules encapsulated in the nanocarrier that contains this photo-linker. *Trans-cis* isomerization is activated by UV irradiation while the return to *trans* form is originated by visible light irradiation or heating.[37] Azobene was used, for example, in UV-light responsive cross-linked polyamide nanocapsules obtained by O/W miniemulsion interfacial polycondensation. In this study, it was shown that the smaller the capsule size, the faster the achieved release. Moreover here, an azobenzene acyl chloride acted as co-surfactant and as crosslinking agent.[1,38] In a study on hydrogel, Peng and coworkers attached azobenzene groups to dextran decorated with a cyclodextrin. *Trans*-azobenzene fit into the cavities of the cyclodextrin but when the hydrogel was irradiated, *cis*-azobenzene did not fit into the cyclodextrin. This mechanism dissociated the cross-linking points and the encapsulated guest were released.[5] Photo-isomerization property are typical of stilbene moieties too. In comparison with azobene, *trans-cis* photo-isomerization requires a shorter wavelength and *cis* form has a higher thermal stability. On the other hand, azosulfonate, diphenyliodonium-2-carboxylate, and pyrenylmethyl ester give photolysis and are applied in photo-responsive hydrogel systems. Coumarin, cinnamylidene acetate, nitrocinnamate, anthracene, and poly(cinnamic acid) group have been used as a reversible crosslinking point. They have been used for hydrogel formation by photo-dimerization as photo-reversible crosslinking points.[37]

Among the myriad of photo-cleavable protecting groups which have been studied, the *o*-nitrobenzyl group is certainly the predominant one since it enables the caging of a wide range of functionalities, such as carboxy, amine, hydroxy, and thiol. Furthermore, the precise positioning of *o*-nitrobenzyl groups in polymer chains has allowed for the controlled alteration of polymer properties upon light stimulus.[39] The *o*-nitrobenzyl moiety, variously functionalized, was studied in a lot of fields of applications. An interesting feature of *o*-nitrobenzyl, over its biocompatibility,[37] is that its photo-cleavage can be obtained either by one-photon absorption of UV light or via two-photon absorption

of near infrared.[40] It has been employed in photo-responsive amphiphilic block copolymer (BCP) micelles,[40,41] in photo-responsive hydrogel systems for biomedical applications,[37] dendrons,[42] dendrimers,[43] functionalized mesoporous silica nanospheres (MSNs),[44] and so on.

So the *o*-nitrobenzyl group is one of the most extremely studied photo-responsive linker because of its versatility of application, its biocompatibility, the possibility to modify its structure with desired functionalities thanks to its functional groups, its capacity to respond to UV by also two-photons irradiation and so the possibility to improve the depth of penetration in tissue applications. For all these properties, it is clear that it is not a case if it is the most studied photo-responsive linker, as emerged by literature studies. In this PhD project, as far as we know, for the first time, the *o*-nitrobenzyl moiety has been employed in a LbL O/W nanoemulsion and not only as photo-trigger but also as component of a free initiator thiol-ene '*click'* reaction. In our strategy, we started from a work on polymer-based hydrogels by DeForest et al., in which they studied a reversible strategy based on the combination of two orthogonal and biocompatible photoreactions. Visible light (λ=490–650 nm) and eosin Y as photoinitiator triggered the thiol-ene reaction involving the radical-mediated addition of a thiol to an alkene. Indeed UV light (λ=365 nm) was the trigger of the photoscission of the *o*-nitrobenzyl ether, which gives a nitrous compound and an acid by-product. They synthesized a biological molecule containing both the thiol group (adding that function on a starting azide by reaction with a N-acetyl cysteine) for the thiol-ene reaction and the photo-labile *o*-nitrobenzyl moiety (Figure 1.10). In this way the thiol-ene and photo-cleavage reactions was used to attach and subsequently remove covalently bound bioepitopes in hydrogel networks, respectively. Because of these reactions are photo-mediated with different wavelengths, by light both the introduction and the removal of relevant biomolecules could be controlled in space and time, indipendently.[45] Furthermore, both the reactions could be initiated by multiphoton irradiation (λ=860 nm for addition, 740 nm for cleavage). In this paper, DeForest et al. showed a useful chemistry performable in the presence of cells because the wavelengths, exposure times, and intensity of light are all cytocompatible.[45]

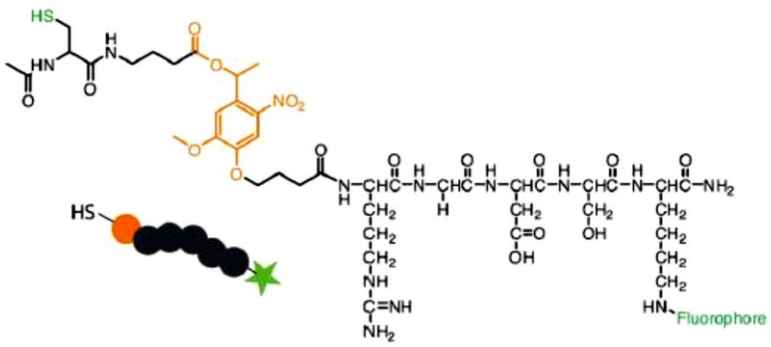

Figure 1.10. The photoreversible *o*-nitrobenzyl ether patterning agent used by DeForest et al.

1.4 Nanotechnology for nutraceuticals.

In this PhD project we focused on nutraceutical drugs encapsulated and stabilized in O/W nanoemulsions. In the simplest case, such nanoemulsion, possibly coated with chitosan, can be used as oral delivery system to prevent or support oncological patients during the clinical treatment. In this scenario, we studied lycopene and curcumin as cardio-protectors for chemotherapies. For this reason, starting from literature, we want to introduce the nutraceuticals world, its advantages in various therapeutic fields and its behaviour when associated with nanotechnologic systems, i.e. oral delivery systems.

"Let food be your medicine and medicine be your food" asserted Hippocrates 2000 years ago. In 1989 Dr Stephen DeFelice coined the term "Nutraceutical" combining the terms "Nutrition" and "Pharmaceutical". Any substance (food or part of it) with medical or health benefits is considered a "nutraceutical" (Figure 1.11).[46] So, nutraceuticals have been regarded as an emerging method for preventing chronic diseases. Moreover, being natural, most of the nutraceuticals exhibit relatively less toxicity and less secondary side effects than drugs used in similar pathological states.[47]

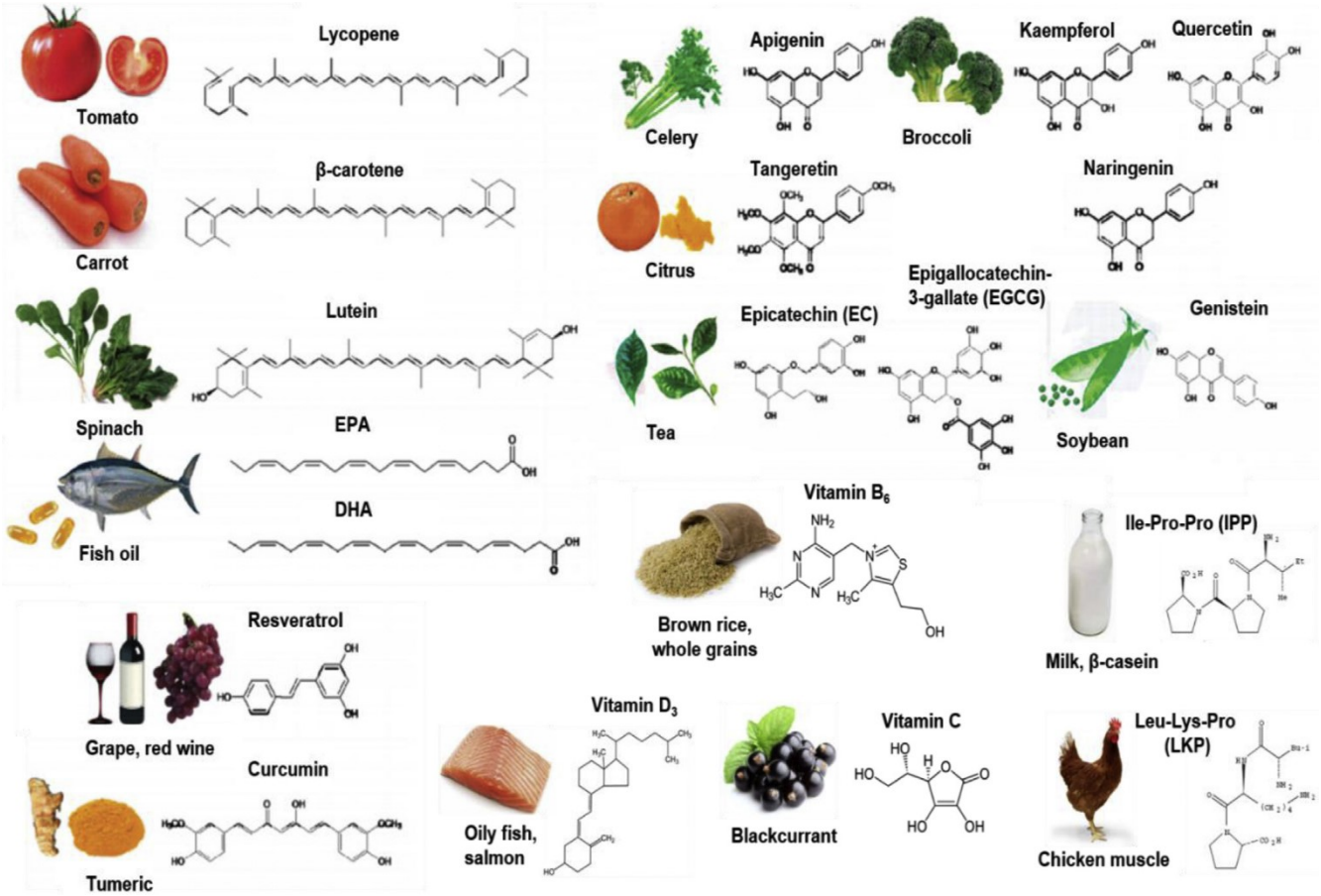

Figure 1.11. Some food-derived bioactive compounds applied in nutraceutical treatments.[48]

The limit of a lot of nutraceuticals is their low bioavailability *in vivo* mainly caused by their lipophilic nature and thus low solubility. So they are poorly absorbed by human body. Moreover, when nutraceuticals arrive in the gastrointestinal (GI) tract, because of various physiochemical transformations, they may lose their bioactivities. Thus it is very interesting to combine nutraceutical drugs with oral delivery systems to improve nutraceuticals bioavailability of phytochemicals changing their pharmacokinetics and biodistribution.[47,48,49,50] On the other hand, some delivery systems are modified to improve the intestinal absorption, for example chitosan is employed as a positively-charged muco-adhesive polymer which increases the absorption of lipophilic compounds, interacting in a specific manner with the intestinal membrane.[47,51]

In literature nutraceuticals were encapsulated and studied in different nanocarriers, such as nanoemulsions,[50] phospholipid based delivery systems, liposomes, phytosomes, solid lipid nanoparticles, self-emulsified drug delivery systems.[47,52]

In delivery systems, different nutraceuticals with chemoprevention and anti-inflammatory properties, had been encapsulated, such as curcumin, green tea polyphenols, coenzyme Q, quercetin, thymoquinone, ajoene, allicin, allyl isothiocyanate, anethole, apigenin, capsaicin, carnosol, caryophyllene, cinnamaldehyde, diallyl sulphide eugenol, [6]-gingerol, humulene, kaempferol, limonene, myrcene, [6]-paradol, perillyl alcohol, phytic acid, piperine, sulforaphane, ursolic acid, zingerone and so on.[46,49] Plant polyphenols (that is, curcumin, resveratrol, epigallocatechin gallate, and so on) and carotenoids (that is, lycopene, ß-carotene, lutein, zeaxanthin, and etc.), have been studied largely. In 2005, studying the polyphenol oral bioavailability, Manach and others showed that proanthocyanidins, galloylated tea catechins, curcumin, and the anthocyanins are the least absorbed pholyphenols. After that, oil-soluble lycopene, phytosterols, ω-3 fatty acids, coenzyme Q10, and so on were studied to improve their solubilities. Moreover, the improvement of oral bioavaibility by nanoemulsion was confirmed by dibenzoylmethane (DBM) nanoemulsion. DBM, a beta-diketone similar to curcumin, is found as a minor constituent in the root of licorice. It is a natural phytochemical with anticancer activities.[50] Resveratrol (trans-3,4,5-trihydroxystilbene) is another example of natural polyphenolic compound. It is abundant in grapes, peanuts, red wine, and a variety of other food sources, and has been reported to have a lot of anticancer properties. However, it has low bioavailability, low water solubility, and instability. These limits have been overcame by active targeting of resveratrol on chitosan nanoparticles.[49] Recently the interest in phenolic compounds in general, and flavonoids in particular, has increased for their use in treatment and prevention of cancer, cardiovascular disease and other pathological disorders.[46] Quercetin (3,3',4',5,7-pentahydroxyflavone) is a natural flavonoid and is a derivative of a flavone (2-phenylchromen-4-one). It contains five hydroxyl groups, the reason for its biological activities and derivative

diversification. Mainly quercetin is found as glycosides in the edible parts of plants, in berries, tea leaves, onion, broccoli and other fruits and leafy vegetable, but is mostly extracted from *Sophoro japonica L*. Besides, quercetin is rich in red wine, black tea and other fruit juices. Quercetin is well known for possessing potent antioxidant activity with anticancer activities. However, its use is limited by its poor bioavailability, hydrophobic nature and low solubility. Thus, biodegradable and biocompatible carriers as delivery systems have been studied to enhance the therapeutic effect of quercetin. Examples of well-studied delivery systems used for quercetin are based on liposomes, PLGA, PLA, chitosan and silica, with good results both in vivo and in vitro studies.[47,53]

In literature herbal drugs have become increasingly popular in particular in the treatment of liver diseases. Toxic chemicals (such as certain antibiotic, chemotherapeutic agents, paracetamol, carbon tetrachloride, thioacetamide etc., excessive alcohol consumption and microbes) have been studied as cause of liver cell injury. In these cases, synthetic drugs often damage more the liver. So formulations containing herbal drugs are becoming popular. For example, curcumin, from *Curcuma longa*, was studied also for its hepatoprotective activity.[54]

As just said, curcumin has interesting anti-inflammatory as well as chemopreventive properties. However, its use in oral administration is limited by its low bioavailability because of its lipophilic nature and its poor stability in aqueous solutions. In our group, O/W nanoemulsions encapsulating curcumin have been proposed to improve curcumin bioavailability in oral delivery systems.[55] In 2016, the behaviour of curcumin encapsulated in our O/W nanoemulsions, co-delivering curcumin and piperine (the alkaloid responsible for the pungency of black pepper and long pepper), has also been studied with the aim to improve the biodistribution of curcumin. In this study it was demonstrated an enhanced anti-inflammatory action of curcumin delivered *in vivo* by oral delivery.[56] In a more recent study, we investigated the interaction of a similar nanocarrier, having just some chemical modifications in the polymer shell, with intestinal epithelial cells CaCo-2 in Transwell culture. The human CaCo-2 cells were used as a model that reproduces the intestinal barrier for *in vitro* prediction of drug performance. The results demonstrated that our nanocarriers could be used to obtain an efficient release of unstable and lipophilic drugs. Furthermore, we demonstrated the beneficial properties of curcumin in treatment and prevention of different inflammatory diseases.[55]

In this PhD project, we focused our studies on anti-inflammatory and cardioprotection properties of natural drugs, such as curcumin and lycopene encapsulated in our chitosan coated O/W nanoemulsion. Moreover in this project, about curcumin we also studied its anti-inflammatory and anticancer properties on photo-responsive LbL O/W trilayer. About lycopene, it is a natural pigment extracted from tomatoes peers. Lycopene is a type of carotenoid,[57] and among carotenoids, lycopene is the most potent antioxidant because of its high number of conjugated dienes.[58] The anti-

inflammatory and cardioprotective effects of lycopene are reported in literature.[57] In an *in vivo* study on rats, it was demonstrated reduced myocardial injury by suppression of oxidative stress.[58]
Combining the already cited advantages of nanotechnology formulations (bioavailability and prolonged circulation time) and natural lipophilic drugs leads to a new category of food supplements to support the oncology patient. Curcumin and lycopene are two of these drugs which can give cancer prevention, attack the inflammatory states and perform cardio-protection activities.[59,60,61,62]

1.5 Ferric oxide nanocubes as contrast agents in MRI.

In this PhD we also focused on diagnostic applications, in particular in Magnetic Resonance Imaging (MRI) of LbL O/W nanoemulsions encapsulating cubic iron oxide nanoparticles. As for the drugs, also in this case we engaged in the use of contrast agents that can be considered safe. So here we want to give an overview of MRI fields and its typical contrast agents, reported in literature.
The nanoscale of LbL nanocarriers is the reason of their goodness diagnostic applications. Among the different imaging modalities, such as X-ray computed tomography (CT), positron emission tomography (PET), single photon emission computed tomography (SPECT), bioluminescence imaging (BLI), fluorescence imaging (FLI), and ultrasound imaging, MRI stands out for its safety and very high spatial resolution for soft tissue, giving not only anatomic but also important functional information. So it is a non-invasive powerful diagnostic technique in medical science, and in particular in cancer diagnosis. However, its sensitivity is lower than PET, SPECT, and optical imaging methods. On the other hand, image contrast can be improved by the introduction of contrast media. MRI contrast agents approved for clinical applications are gadolinium (Gd) or manganese (Mn) as paramagnetic molecules, and superparamagnetic iron oxide (SPIO) as nanoparticles. Their diagnostic capability can be enhanced when they are combined with advanced and multifunctional imaging probes. To this aim, a wide range of nanosystems have been used such as dendrimers, carbon nanotubes, fullerenes, viral capsids, liposomes and micelles. Among these nanosystems, LbL polyelectrolyte nanocarriers, encapsulating contrast agents, have shown great applications. For *in vivo* applications, their biocompatibility and stability are two important aspects. The biosafety mainly depends on the imaging component and capsule materials.[63] As said previously, various polyelectrolytes are biocompatible and biodegradable polymers. However, some interesting contrast agents, such as gadolinium, can be toxic. Nanocarriers improve the circulation time of drugs/contrast agents and so their accumulation in the target site, limiting in this way the amount of contrast agent and therefore the toxicity. In this contest, PEGylation on LbL capsule surface is a simple method to preserve nanocarriers' cargo from unspecific cellular uptake and leading to a prolonged blood circulation time.[64,65]

Magnetic contrast agents can be divided into two categories: paramagnetic and super-paramagnetic ones. They are characterized by either longitudinal or transverse proton relaxation time and thus give higher image contrast.[64] The paramagnetic compounds are composed by metal ions with unpaired electrons (including lanthanides like gadolinium, Gd^{3+} or manganese Mn^{2+}), and mainly reduce the longitudinal (T1) relaxation property. When the metal is chelated with ligands, such as diethylene triamine pentaacetic acid, DTPA, it is less toxic because the chelating ligand avoid the binding between the metal ion and the body. The super-paramagnetic magnetic nanoparticles (such as iron oxides) have a strong effect on the transversal (T2) relaxation properties. The super-paramagnetic nanoparticles have much higher magnetic moments, are non-toxic and rapidly cleared from the organism. So they are preferred to the Gd complexes as contrast agents. Moreover, in comparison with paramagnetic agents, which require the close contact between metal center and water molecules, super-paramagnetic agents do not necessarily need the direct contact.[64] Among the different super-paramagnetic contrast agents, such as magnetite, maghemite, cobalt ferrite, gadolinium ferrite, chromium dioxide, carbonyl iron, nickel, cobalt, neodymium–iron–boron or some other cobalt systems, magnetite is the favourite one. It has been well-studied and shows a very low toxicity. In fact, super-paramagnetic iron oxide nanoparticles are much safer than other ones, because the human body has a big iron pool and the degradation of those nanoparticles lead them in that iron pool to participate physiological iron homeostasis.[64,65,66] So nanomedicine combined with magnetic iron oxide nanoparticles offer a lot of advantages such as easy and precise synthesis procedures, high magnetic response, tunable morphologies, enhancing patient safety and combining good magnetic properties and very reduced toxicity. Iron oxide nanoparticles can be a safer replacement to iodine or gadolinium tracers which are hazardous for patients. The US Food and Drug Administration (FDA) and the European Medicines Agency (EMA) have approved the medical use of some iron oxide nanoparticle formulations.[67] An example of iron oxide nanoparticles application as MRI contrast agent is a work by Chertok et al. They studied the *in vivo* MRI detection of brain tumors in rats using iron oxide nanoparticles. In accordance with other studies, their work show as magnetic nanoparticles can be retained at tumor sites applying a locally external magnetic field. Moreover since the strong T2 relaxation of the iron magnetic nanoparticles, they confirmed as MRI is non-invasive detection tool.[68] Another example is a work by Prévotet et al. about super-paramagnetic iron oxide nanoparticles loaded in O/W nanoemulsions decorated with specific monoclonal antibody as contrast agents for atherosclerosis Magnetic particle imaging (MPI) and MRI. They results showed that their nanoemulsions could selectively image atherosclerosis. Moreover these nanoparticles were biocompatibility and biodegradability so able to use in *in vivo* applications.[69]

In 2016, our group published a work in which biocompatible, multifunctional and multicompartment nanocarriers consisted of an oil-core/hybrid polymer/silica-shell. To stabilize additionally our nanocapsules, the outer silica shell was coated with polyethyleneglycol (PEG). It is known that silica is one of the few inorganic materials recognized as 'safe' by the US FDA. In this work Nile Red (a lipophilic molecule) was encapsulated in those nanocapsules as drug model and CdSe (an inorganic nanoparticles), as a contrast agent model, with no variation in the expected size.[70]

In 2017, we studied O/W nanoemulsion loaded with cobalt ferrite oxide ($Co_{0.5}Fe_{2.5}O_4$) nanocubes (21 nm) for photo-acoustic and magnetic resonance dual imaging in cancer therapy. We performed *in vitro* and *in vivo* studies. The proposed O/W systems showed no significant cytotoxicity and a high values of r2/r1, it could be use as T2 weighted image contrast agents. In this work we introduce the use of photo-acoustic, also called laser optoacoustic (LO) imaging, which is a new non-invasive and non-ionized diagnostic too, with high sensitivity and excellent resolution. In our nanocarriers, even if the cobalt, the concentration of the nanocubes was sufficiently low to avoid significant toxicity, but able to provide MRI and PA response.[71]

Returning to the safer iron oxide nanoparticles and the said advantages brought by our O/W nanoemulsions, we studied photo-acoustic *in vitro* and MRI *in vitro* and *in vivo* responses of nanocubic iron oxide nanoparticles encapsulated in oil-core-PEG shell nanocarriers. This study had been object of this PhD work. In this way, we have surpassed the problem of toxicity connected to cobalt. Moreover, as iron oxide nanocubes are smaller than cobalt-ferrite ones, we were able to scale our nanoemulsions dimensions encouraging their internalization in the tumor tissue.

1.6 Brief mention on nano-'theranostic' delivery systems.

We have just discussed about the advantages given by engineered nanoparticles in therapeutic and diagnostic fields, such as enhanced permeation, specific release and enhanced medical imaging. Theranostics is the fusion of the words 'therapy' and 'diagnosis'.[30] 'Theranostic' nanoparticles combines therapeutic compounds and diagnostic agents in a single tool and so they have been particular interest in science research for their highly beneficial applications. The preparation of theranostic nanoparticles requires a multidisciplinary context of studies and investigation (Figure 1.12).[72] Theranostic nanoparticles give the possibility to develop more specific and individualized therapies for various diseases. Furthermore, the co-delivery of therapeutic and imaging functions permit to monitor the imaging also during the treatment.[73] In cancer therapy, the research has a particular interest to implement theranostic nanoparticles with safer and more efficacious diagnostic and therapeutic agents.[74,75] The use of the nanocarriers in theranostics could bring several advantages. The nano-size of the nanocarriers provides various advantages due to EPR effect first of all, for the

theranostic applications. So the nanocarriers can be localized in the cancer and inflammatory tissues. Moreover, the typical large surface area-volume ratio of the nanocarriers permit a higher loading capacity and the nanocarriers can be functionalized with multiple functionalities.[77] As known, the nanoparticles' surfaces can be modified to improve their biocompatibility and in the inner of the capsules, different drugs or contrast agents can be encapsulated (Figure 1.13). Thus for example, using super-paramagnetic iron oxide nanoparticles in a theranostic nanoparticles, we can not only use that in MRI for in vivo imaging but also manipulate the capsules by the iron oxide nanoparticles to carry drugs in the specific tissues by magnetic fields.[72,73]

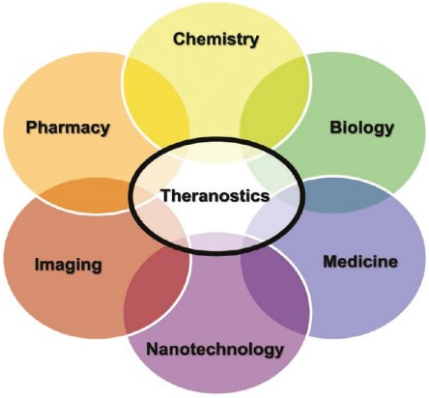

Figure 1.12. Schematic representation of the multidisciplinary research field of (nano)theranostics.[76]

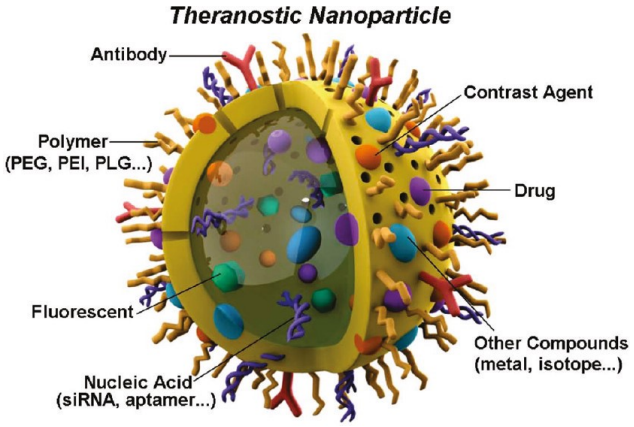

Figure 1.13. Example of theranostic nanoparticles with different component to functionalize the surface. In the inner core, various compounds can be encapsulated such as nucleic acids, imaging contrast agents, drugs, and fluorescent material for different theranostic purposes.[72]

For what said, theranostic nanocapsules are able to detect diseases and at the same time release the therapeutic drugs with a *spatio-temporal* control. In this context, LbL polyelectrolyte nanocapsules are particularly interesting because of the possibility to be engineered with different functionalities,

for their low cost, ease of preparation and versatility.[1] Theranostic nanoparticles are becoming an important growing area of research. With an accurate choice of materials, these nanoparticles could provide less invasive tools for diagnostic and therapy, with more accuracy and safer for the patients.[30]

1.7 Aim of the PhD project

The following PhD project regards the field of the drug delivery systems. In particular, the aim of this project is the study of chemical modifications useful to activate photo-stimuli-responsive oil core polymer nanocapsules as theranostic delivery system. Mainly, we will focus the attention on layer by layer (LbL) polymer based nanocapsules loaded with natural drugs and safe contrast agents.

In the tumor treatment context, our main purpose is the use of safe nanocarriers to reduce the side effects for the patient, improving the therapy efficacy and the bioavailability of the drugs. So in this PhD project we study systems which can enhance the clinical performance and the cancer detection exploring chemical modifications in the polymeric compositions and/or in the oil core formulations. To this aim we focused the attention on highly versatile nanocapsules built around an oil core and made of completely biocompatible natural polymers employable for therapeutic and diagnostic purposes. Chemical functionalization of nanoemulsions' shells is studied to engineer a photo-responsive nanocarrier with *spatio-temporal* control in the release of the drug.

In **Chapter 2** a LbL O/W cross-linked photo-responsive nanoemulsion, loaded with a natural drug, curcumin, is explained. As just demonstrated in our group, it is possible to functionalize the polymers deposited on the oil core, such as glycol chitosan and heparin, with a thiol moiety and an allylic moiety respectively, and then create a covalent bond between the polymeric shells *via* a biocompatible photoinitatior free thiol-ene '*click'* reaction, to improve the nanosystem's stability.[15] Starting from this strategy to obtain a stable cross-linked LbL systems, we introduced a photolabile chemical linker, based on a modified N-acetyl cysteine-*o*-nitrobenzyl moiety,[45] between the polymeric materials of LbL. Functionalized the glycol chitosan with this thiol-photo-responsive moiety and the heparin with an allyl one, we were able to perform the cross-linkage and to stabilize our LbL O/W nanoemulsion multilayer shell by the photoinitiator free thiol-ene '*click'* reaction. Interestingly, the photo-responsive linker gave us the possibility to trigger a controlled destabilization of the nanocarriers to release the drug by single or multi-photon UV light (365 nm or 740 nm). After the chemical modifications of the nanocarriers and its characterizations in terms of stability and conditions of release, we performed biological studies of uptake and cell viability on melanoma cells.

In **Chapter 3** it is reported a recent published article which is part of this PhD project. It regards an oral delivery application of our nanoemulsions encapsulating nutraceutical drugs, such as curcumin and lycopeneand the study of their cardioprotection and anti-inflammatory effects. These properties

have been assessed by i*n vitro* tests performed on cardiomyoblasts (H9C2 cells) in presence of doxorubicin.

In **Chapter 4** we report another possibility concerning the modification of the oil core formulation of the nanoemulsions, using an inorganic compound, in particular cubic iron oxide nanoparticles as contrast agents. We prepared oil-core-PEG shell nanocarriers encapsulating nanocubic iron oxide nanoparticles to study how these systems respond to *in vitro* photoacoustic and *in vitro* and *in vivo* magnetic resonance imaging.

Final conclusion and future perspectives are presented and discussed in **Chapter 5**. Each part of this work can be seen distinctly or in a more general point of view. In this case, we can think to engineer a photo-responsive LbL O/W nanoemulsion co-loaded with natural drugs and safe contrast agents to employ as theranostic nanocapsules.

1.8 References

1. L.L. del Mercato et al., *Advances in Colloid and Interface Science* **2014**, 207, 139–154.
2. Y. Yan, G. K. Such, A. P. R. Johnston, H. Lomas, and F. Caruso, *ACSNano,* **2011**, 5(6), 4252-4257.
3. A.P.R. Johnston et al., *Current Opinion in Colloid & Interface Science*, **2006**, 11, 203–209.
4. Y. Yan, M. Björnmalm, and F. Caruso, *Chem. Mater*., **2014**, 26, 452−460
5. E. Fleige et al., *Advanced Drug Delivery Reviews*, **2012**, 64, 866-884.
6. Pilar Rivera Gil et al., *Nanotoday*, **2008**, 3(3-4)
7. E. Donath, G. B. Sukhorukov, F. Caruso, S. A. Davis, and H. Möhwald, *Angew. Chem. Int.,* **1998**, 37 (16)
8. G. Decher, *Science,* **1997**, 277
9. B. J. Cui, Y. Wang, A. Postma, J. Hao, L. Hosta-Rigau and B. J. Cui, Y. Wang, A. Postma, J. Hao, L. Hosta-Rigau and F. Caruso, *Adv. Funct. Mater.,* **2010**, 20, 1625.
10. R. Vecchione, U. Ciotola, A. Sagliano, P. Bianchini, A. Diasproc and P. A. Netti, *Nanoscale*, **2014**, 6, 9300–9307.
11. Prashant K. Deshmukh et al., *Journal of Controlled Release*, **2013**, 166, 294-306.
12. R. Vecchione et al., *Small*, **2016**, 22(12), 3005-3016.
13. J. Fang et al., *Advanced Drug Delivery Reviews,* **2011**, 63, 136–151.
14. G. Bozzuto, A. Molinari, *International Journal of nanomedicine*, **2015**, 10, 975-99.
15. V. Calcagno, R. Vecchione, A. Sagliano, A. Carella, D. Guarnieri, V. Belli, L. Raiola, A. Roviello, P.A. Netti, *Colloids and Surfaces B: Biointerfaces*, **2016**, 142, 281-289.
16. Heng Pho Yap et al., *Adv. Mater.,* **2009**, 21, 4348–4352.
17. P. Bawa, V. Pillay, Y. E Choonara and Lisa C du Toit, *Biomed. Mater.,* **2009**, 4, 022001.
18. S. Ganta et al., *Journal of Controlled Release,* **2008**, 126, 187–204.
19. S. Mura, J. Nicolas and P. Couvreur, *Nature Materials,* **2013**, 12.
20. V.N Gunjkar, S.L. Patwekar and S.P. Dhage, *World Journal of Pharmacy and Pharmaceutical Sciences*, **2015**, 4(6).
21. Younghyun Cho, Jaehoon Lim and Kookheon Char, *Soft Matter*, **2012**, 8, 10271–10278.
22. Y. Ping, J. Guo, H. Ejima, X. Chen, J. J. Richardson, H. Sun, and F. Caruso, *Small,* **2015**, 11(17), 2032–2036.
23. K. Liang, G. K. Such, A. P. R. Johnston, Z. Zhu , H. Ejima, J. J. Richardson, J. Cui, and F. Caruso, *Adv. Mater.,* **2014**, 26, 1901–1905.
24. Y. Lu et al., *Journal of Controlled Release,* **2014**, 194, 1–19.
25. D. Roy et al., *Progress in Polymer Science*, **2010**, 35, 278–301.

26. A. Zhuk and S. A. Sukhishvili, *Soft Matter*, **2013**, 9, 5149–5154.
27. A. G. Skirtach, A. A. Antipov, D. G. Shchukin, and G. B. Sukhorukov, *Langmuir*, **2004**, 20(17), 2004 6989.
28. J. L. Nelson, B. L. Roeder, J. C. Carmen, F. Roloff, and W. G. Pitt, *Cancer Research,* **2002**, 62, 7280–7283.
29. A. Y.Rweia, W. Wanga, D. S. Kohanea, *Nano Today*, **2015**, 10, 451-467.
30. J. U. Menon, P. Jadeja, P. Tambe, K. Vu, B. Yuan, K. T. Nguyen, *Theranostics,* **2013**, 3(3).
31. N. Fomina et al., *Advanced Drug Delivery Reviews,* **2012**, 64, 1005–1020.
32. B. Yan, J.C. Boyer, D. Habault, N. R. Branda, and Y. Zhao, *J. Am. Chem. Soc.,* **2012**, 134, 16558−16561.
33. B. Yan, J.C. Boyer, N. R. Branda, and Y. Zhao, *J. Am. Chem. Soc*,. **2011**, 133, 19714–19717.
34. M. He, J. Li, S. Tan, R. Wang, and Y. Zhang, *J. Am. Chem. Soc.,* **2013**, 135, 18718−18721.
35. Avijit Jana et al., *J. Am. Chem. Soc.,* **2012**, 134, 7656−7659.
36. S. Karthik et al., *Chem. Commun.,* **2013**, 49, 10471—10473.
37. I. Tomatsu et al., *Advanced Drug Delivery Reviews,* **2011**, 63, 1257–1266.
38. V. Marturano et al., *Polymer,* **2015***,* 70, 222-230.
39. Pauloehrl T. et al., *Angew. Chem. Int. Ed*., **2012**, 51, 9181-9184.
40. Y. Zhao, *The Chemical Record*, **2007**, 7, 286–294.
41. E. Cabane et al., *Soft Matter*, **2011**, 7, 9167–9176.
42. Chiyoung Park et al. *Angew. Chem. Int. Ed*., **2008**, 47, 2959 –2963
43. Yan Li et al., *Journal of Polymer Science: Part A: Polymer Chemistry,* **2010**, 48, 551–557.
44. Juan L. Vivero-Escoto et al., *J. Am. Chem. Soc.,* **2009**, 131, 3462–3463.
45. DeForest et al., *Angew. Chem. Int. Ed.,* **2012**, 51, 1816-1819.
46. M. Choudhary and V. Tomer, *Proc Indian Natn Sci Acad* , **2013**, 79(4), 985-996.
47. Yuwen Ting et al., *Journal of functional foods,* **2014**, 7, 112-128.
48. J.P. Gleeson et al., *Trends in Food Science & Technology,* **2016***,* 53, 90-101.
49. H.B. Nair et al., *Biochemical Pharmacology,* **2010**, 80, 1833–1843.
50. Qingrong Huang et al., *Journal of food science,* **2010**, 75(1).
51. M. Yao, D. J. McClements and H. Xiao, *Current Opinion in Food Science,* **2015**, 2, 14–19.
52. D. Ileš et. al., *Strojarstvo,* **2011**, 53(2), 127-136.
53. Ju-Suk Nam et al., *Molecules,* **2016**, 21, 108.
54. Fasalu Rahiman O.M. et al., *International Journal of Pharmaceutical Sciences Review and Research*, **2011**, 8(1).
55. A. Langella et al., *Colloids and Surfaces B: Biointerfaces,* **2018**, 164, 232–239.

56. R. Vecchione et al., *Journal of Controlled Release,* **2016**, 233, 88–100.
57. Xin Wang et al., *J Mol Hist,* **2014**, 45, 113–120.
58. Pankaj Bansal et al., *Molecular and Cellular Biochemistry,* **2006**, 289, 1–9.
59. Gullett A.R. et al., *Semin. Oncol*., **2010**, 37 (3), 258-281.
60. Waliszewski KN. et al., *Salud Publica Mex*, **2010**, 52 (3), 254-265.
61. Trottier G. et al., *Nat. Rev. Urol.,* **2010**, 7(1), 21-30.
62. Giovannucci E. et al., *Journal of the National Cancer Institute,* **2002**, 94(5), 391-398.
63. D.P. Cormode et al., *Advanced Drug Delivery Reviews*, **2010**, 62, 329–338.
64. H. Ai, *Advanced Drug Delivery Reviews,* **2011**, 63, 772–788.
65. H. Shokrollahi, *Materials Science and Engineering C,* **2013**, 33, 4485–4497.
66. U. Ayanthi Gunasekera et al., *Targ Oncol,* **2009**, 4, 169–181.
67. E. Tombácz et al.. *Biochemical and Biophysical Research Communications,* **2015**, 468, 442–453.
68. B. Chertok et al., *Biomaterials,* **2008**, 29, 487–496.
69. G. Prévot et al., *International Journal of Pharmaceutics,* **2017**, 532, 669–676.
70. R. Vecchione, G. Luciani, V. Calcagno, A. Jakhmola, B. Silvestri, D. Guarnieri, V. Belli, A. Costantini and P.A. Netti, *Nanoscale*, **2016**, 8, 8798–8809.
71. R. Vecchione et al., *Nanomedicine: Nanotechnology, Biology, and Medicine,* **2017**, 13, 275–286
72. X. Ma et al., *Accounts of Chemical Research,* **2011**, 44(10), 1114-1122.
73. J. Xie et al., *Advanced Drug Delivery Reviews,* **2010**, 62, 1064–1079.
74. S.M. Janib et al., *Advanced Drug Delivery Reviews,* **2010**, 62, 1052–1063.
75. Yoo et al., *Accounts of Chemical Research,* **2011**, 44(10), 863–874.
76. Lammers et al., *Accounts of Chemical Research*, **2011**, 44(10), 1029–1038.
77. J.H. Ryu et al., *Journal of Controlled Release,* **2014**, 190, 477–484.

Chapter 2

Photo-responsive cross-linked drug delivery systems based on Layer-by-Layer oil-in-water nanoemulsions

Abstract

In the cancer therapy, stimuli-responsive drug delivery systems are of particular interest, managing to reduce the collateral effects in the healthy tissues and improving the selectivity of the drugs in the cancer ones. Here we report the strategy of preparation of a photo-responsive cross-linked trilayer deposited onto an oil-in-water (O/W) nanoemulsion via Layer-by-Layer (LbL) technique. Our systems is made of completely biocompatible materials such as soybean oil as core, egg lecithin as surfactant and polymeric shells of glycol chitosan and heparin. The oil core can be empty or loaded with curcumin as nature based drug. The cross-linkage of the trilayer is performed via a photoinitiator free thiol-ene '*click'* reaction. In particular we introduce an *o*-nitrobenzyl group functionalized with a thiol moiety which can perform both the thiol-ene '*click'* reaction and the reaction of cleavage for the controlled release of drug at specific wavelengths. So, we showed the preparation and characterization of a photo-responsive natural nanocarrier stable in physiological conditions thanks to the thiol-ene cross-linkage. The performance of the system are also studied in biological environment on melanoma cells (A375.S2 cell lines). The results promise for possible future applications in the treatment of skin tumors or in surgery applications considering the penetration limitation of the light stimulus.

2.1 Introduction

Nanomaterials are born from the fusion between nanotechnology and biomedicine and have various advantages compared to traditional therapies (such as targeted delivery, controlled drug release and improvement of cell barrier crossing).[1,2] Among the diverse nanocarriers for cancer drug delivery studied in the last decades, a particular interest is recognized to Layer-by-Layer (LbL) polymeric nanocapsules, based mainly on electrostatic interaction between the polymers, for the precision of the final particles, their high versatility and the possibility to encapsulate different drugs and release them in different manners.[2,3,4] From 2014, our team developed biodegradable O/W nanoemulsions (size < 200 nm),[5] specific for hydrophobics drugs, coated with biodegradable polyelectrolytes via LbL technique, with high monodispersity and stability over time.[6,7] Because of the weakness of the electrostatic interaction, in 2016 we developed a photoinitiation free thiol-ene '*click'* reactions, providing a completely non-cytotoxic final product, to improve the stability of our O/W nanoemulsion by cross-linkage, e.g. a covalent bond, between the polymeric shells.[8,9]

In cancer therapy, for their easy preparation and versatility,[10,11] LbL nanocarriers are interesting platforms to reduce the toxicity of the drugs and improve the selectivity towards the tumor. In particular, the differences between normal and pathological tissues are the start point for the design of stimuli-responsive nanocarriers, that can attack cancer cells without damaging healthy ones.[12] It is

known that there are two types of stimuli for drug's release: endogenous (e.g., pH, enzymes, redox potential, glucose concentration, ions) or exogenous stimuli (temperature, magnetic fields, electrical fields, ultrasound and light). The choice of release mechanism is connected to the desired application.[2,5,13]

Particularly within this project, we focused on light as stimuli source. It is a particularly interesting stimulus for its advantages of not to be invasive and to permit a *spatio-temporal* control in the release.[14] Moreover, the light is strongly absorbed by tissue and can be focused on microscopic spot, determining a controlled opening of the individual capsules. Additionally, light helps to improve the therapeutic benefit and minimize the toxicity, because the active drug is delivered and released in the proximity of the affected tissues. Finally, radiation of UV, near IR and IR frequency are tissue compatible, and so show a quite good biocompatibility in specific conditions.[4,13,15]

Light has been strongly studied in literature introducing photo-responsive molecules in the structure of different nanocarries. Such as *o*-nitrobenzyl moieties,[16,17] biaryl-substituted tetrazole moiety,[18] perylene-3-ylmethanol,[19] azobene,[4,13,20,21] stilbene, azosulfonate, diphenyliodonium-2-carboxylate, pyrenylmethyl ester, coumarin, cinnamylidene acetate, nitrocinnamate, anthracene, poly(cinnamic acid),[20] 7-methoxy quinolone[22] in hydrogels,[4,16,17,18,20,23] carbon dots,[22] inorganic materials,[24] O/W mini-emulsions.[13,21] For a lot of photochemical reaction near infrared (NIR) light is not sufficient but its penetration depth is higher than UV/vis. However, on the other hand, also a single UV/vis photon, manages to achieve a lot of reaction widely applied in photo-responsive nanoparticles. The use of two-photon absorption is a strategy to combine the deeper penetration of NIR and the UV/vis triggered chemical reactions.[24,25] So this could be a good strategy but there are very few organic chromophores which absorb in NIR region, while the majority responds to UV light.[26]

In particular, the *o*-nitrobenzyl group has been our choice and it has been introduced as a photo-responsive linker in the multilayer shell of our O/W nanoemulsions. This because the *o*-nitrobenzyl group has a chemical structure which can be functionalized in the desired manner easy,[27] it is biocompatible,[20] and another important characteristic is that its photo-cleavage can be obtained either by one-photon absorption of UV light or via two-photon absorption of NIR, improving the depth of penetration in tissue application.[28] This photo-cleavable group had been used in a lot of photo-responsive systems such as micelles,[28,29] hydrogel,[20] dendrons,[30] dendrimers,[31] functionalized mesoporous silica nanospheres,[32] and so on.

In this work, we report an O/W core - LbL trilayer shell, which is exposed twice to the light stimulus. Indeed, at the beginning the trilayer is stabilized by a photoinitiator free thiol-ene '*click'* reaction and then it is destabilized by an appropriate wavelength, and both of them involve the *o*-nitrobenzyl group. In this work, we synthetized an *o*-nithobenzyl group with some modification of a strategy shown in

literature.[33] In particular, we introduce a thiol group *via* a N-acetyl cysteine on the *o*-nitrobenzyl group and then by a *coupling* reaction we prepare a glycol chitosan functionalized with this photo-linker. The polymers of the shell are deposited alternately to form a trilayer multishell and are functionalized with the thiolated *o*-nitrobenzyl group and an allyl group respectively. The nanocarrier is then stabilized by the photoinitiator free thiol-ene '*click'* reactions to improve its stability in physiological conditions. On the other hand, using UV light at 365 nm we induce the photo-cleavage of the *o*-nitrobenzyl moiety and the controlled release of the drugs. Such systems is explored in melanoma's cellular vitality tests. The possibility to use two-photons mechanism instead of UV thanks to the *o*-nitrobenzyl group, makes our final photo-responsive system a potentially powerful instrument for the treatment of skin tumors or in the treatment of cancer residual cells during surgery.

2.2 Material and Methods

Soybean oil (density at 20 °C of 0.922 g mL^{-1}) and surfactant Lipoid E80 (egg lecithin powder 80-85% enriched with phosphatidylcholine and 7–9.5% content in phosphatidylethanolamine) were purchased from Lipoid GmbH and used without further purification. For preparation of all nanoemulsions and solutions, Millipore Milli-Q water was used. Curcumin (from *Curcuma longa* Turmeric, powder), heparin sodium salt (from porcine intestinal mucosa), allylamine, 1-hydroxybenzotriazole hydrate (HOBt), 1-(3-dimethylaminopropyl)-3-ethyl-carbodiimide hydrochloride (EDC), 5,5'-dithiobis(2-nitrobenzoicacid) (DTNB, also known as Ellman's reagent), Fluorescein5(6)-isothiocyanate (FITC), Rhodamine B isothiocyanate (RhodB), sodium chloride, N-acetyl-L-cysteine (NAC), Tris(2-carboxyethyl)phosphine hydrochloride (TCEP), Ethyl 4-bromobutyrate, 4-[4-(1-Hydroxyethyl)-2-methoxy-5-nitrophenoxy]butyric acid (Hydroxyethyl photolinker), sodium azide, sodium sulfate, anhydrous pyridine, magnesium sulfate, N,N′-Dicyclohexylcarbodiimide (DCC), N,N′-Diisopropylcarbodiimide (DIC), 4-(Dimethylamino)pyridine (DMAP), anhydrous pyridine, N,N-Diisopropylethylamine (DiPEA), triphenylphosphine, sodium bicarbonate, celite, acetic acid, methanol, sodium hydroxide, hydrochloric acid, deuterium oxide (D_2O), Deuterochloroform ($CDCl_3$), trifluoroacetic acid (TFA), anhydrous and not dimethyl sulfoxide (DMSO), anhydrous and not dichloromethane (DCM), acetone, diethyl ether, anhydrous and not tetrahydrofuran (THF), hexanes, ethyl acetate were purchased from Sigma-Aldrich. Glycol chitosan (GC) was purchased from Wako Chemicals. Carboxyl latex beads (4% w/v, 0.1 μm) was purchased from Invitrogen. Dialysis membranes were purchased from Spectrum Laboratories Inc. PBS tablets (1x) was purchased from MP Biomedicals.

Oil in water nano-emulsion.

As previously described,[6] a 20 wt % oil in water pre-emulsion was prepared. A 5.8 g of Lipoid E 80 was dissolved in 24 mL of soy-bean oil at 60 °C and then added dropwise to the aqueous phase (Milli-Q water) and mixed using the immersion sonicator (Ultrasonic Processor VCX500 Sonic and Materials). The pre-emulsion so obtained, was then homogenized at 2000 bar by a high-pressure homogenizer (110P series microfluidizer) to obtain the final nanoemulsion. The nanoemulsion could be loaded with curcumin by dissolving the drug in the oil phase in the pre-emulsion step, after lecithin (100 mg of curcumin in the oil phase for 15 minutes at 60°C) or with FITC (0.75mg/mL) dissolved in 4 mL of ethanol added always in the pre-emulsion step and drying the ethanol from the mixture with mild heating.

Modification of glycol chitosan with rhodamine B isothiocyanate.

Glycol chitosan (100mg, 0.5 mmol) was dissolved in 10 mL of a 0.1M acetic acid solution. After complete dissolution, a solution of RhodB (5.0 mg in 500 μL of DMSO) was added dropwise. The reaction proceeded overnight at room temperature, protected by light. Sample was then dialyzed (dialysis tubing of 3.5 kDa) against water more times for a couple of days to remove no reacted dye. Finally, the purified product was freeze-dried for 24 h. The degree of functionalization was determined with ^{1}H NMR spectra and it resulted less than 1%.

Modification of heparin with fluorescein isothiocyanate.

As mentioned in a literature procedure,[34] FITC (6.4 mg) was conjugated with heparin (20 mg), both in the case of pure or allylated heparinin sodium bicarbonate buffer (pH 8.5) for 4-6 h at 25°C. Heparin-FITC was precipitated by ethanol. The original protocol was modified adding same centrifugation steps to wash the polymer faster. Three centrifuges (10000 rpm, 10 min, 4°C) were performed, replacing the surfactant with ethanol each time. Then, the polymer was dissolved in water and dialyzed (dialysis tubing of 3.5 kDa) against water for 3 days. The degree of functionalization was determined with ^{1}H NMR spectra and it resulted less than 1%.

Modification of glycol chitosan with N-acetylcysteine.

In a flask, 0.5 mmol of glycol chitosan (M_v = 205.21 kDa), in some cases just modified with a dye, were dissolved in 10 ml of Milli-Q water acidified at pH 5-6. In a different beaker, 1 mmol of N-acetylcysteine was dissolved in DMSO with the minimum volume required. Then, we added 1 mmol of EDC and 1 mmol of HOBt to NAC solution and we left under stirring for 15 min. The pH was at 5-6. Then, to the solution of GC, we added dropwise the solution of the activated NAC, checking that

pH is between 5 and 6 and, if necessary, fixing it, recheck it in the first hour of reaction. We let it react overnight at room temperature. After that, pH reaction solution was adjusted at 4. A 0.5 M TCEP (1.5 mmol) water solution was added to the reaction flask and pH was maintained at a value of 4. The reactions proceeded at room temperature for 1 h. The product was then purified by dialysis (dialysis tubing of 3.5 kDa) four times against water acidified with HCl at pH 4. Each dialysis lasted 2 h or more. The whole purification process ended in two days maximum. Finally, the purified product was freeze-dried for 24 h (Freeze Dryer CHRIST Alpha 1–4 LSC).

The Ellman's test,[35,36,37] a colorimetric assay, was used to determine the free thiols in the polymer. To estimate the molar extinction coefficient (ε) of TNB^{2-} it was performed a calibration curve with standard solutions of NAC. For the functionalized glycol chitosan, 0.4 mg of polymer was dissolved in 0.5 mL of acetic acid 0.1M and mixed with a solution of 0.2 mg/mL DTNB in a phosphate buffer at pH 8.03. The sample was stored in the dark at 25 °C under stirring for 2 h. Then, the absorbance of TNB^{2-} was registered at 412 nm using a Varian Cary Scan 100 Spectrophotometer.[8]

Modification of heparin with allylamine.

Heparin was modified with allylamine as showed in a previous study.[8] In the general procedure, the reaction was in water at pH 6.8, for 6 h and at room temperature. The molar ratio between the reagents was heparin/allylamine/HOBt/EDC = 1/10/4/4. Sample was then dialyzed (dialysis tubing of 3.5 kDa) against 1% w/v NaCl, 0.75% w/v NaCl, 0.5% w/v NaCl, 0.25% w/v NaCl and four times against water. Each dialysis lasted 2 h or more. The whole purification process ended in two days maximum. Finally, the purified product was freeze-dried for 24 h. The degree of functionalization (80%) was determined with ^{1}H NMR spectra.

Synthesis and characterization of the photocleavable linker: the thiol modified o-nitrobenzyl group

The synthesis of azide-funzionalized photodegradable precursor (PLazide) was reported in literature.[33] Briefly, after azidification and deprotection of ethyl-4-bromobutyrate to obtain 4-azidobutanoic acid, it was converted in its anhydride. Then, the anhydride was reacted with 4-[4-(1-Hydroxyethyl)-2-methoxy-5-nitrophenoxy]butanoic acid (Hydroxyethyl photolinker). The final product (PLazide) was checked by LC/MS and ^{1}H NMR. LC/MS (ESI): $C_{17}H_{21}N_4O_8^-$ $[M-^1H]^-$, calculated 409, found 409. ^{1}H NMR (600MHz, $CDCl_3$,δ: 7.58 (s, 1H), 6.99 (s, 1H), 6.48 (q, 1H), 4.13 (t, 2H), 3.96 (s, 3H), 3.38 (t, 2H), 2.6 (t, 2H), 2.48 (t, 2H), 2.19 (m, 2H), 1.92 (m, 2H), 1.62 (d, 3H). The pure product (PL azide) was reducted to PL amine. The started PLazide (0.1 mmol) and triphenylphosphine (1.5 x) were dissolved in tetrahydrofuran (THF, 2 mL), and then water was added to the mixture (v/v 2:1, THF:H_2O). The reaction was stirred for 3 h at room temperature. To obtain

the complete hydrolysis of PL iminophosphorane intermediate, an excess of a 1 M HCl solution (120 mL) was added to the mixture.[38] The reaction was stirred overnight at room temperature. The reaction run was checked by LC/MS (ESI): $C_{17}H_{23}N_2O_8^+$ $[M\text{-}^1H]^+$, calculated 385, found 385. At the end, the crude mixture was concentrated *via* rotary evaporation. The general procedure for the coupling of N-acetyl-L-cysteine and the PLamine was kept by a previous work[39], with same modifications in molar ratio between reagents and starting from an activated amine, without purification but pushing the reaction until completion.The PLamine intermediate (0.1 mmol) was dissolved with dry THF (5 mL) and activated with N,N-diisoproprylethylamine (DiPEA, 3 x), stirring under argon for 30 min. On the other hand, NAC (1.2 x) was co-evaporated twice with THF (2 mL) under reduced pressure and then was dissolved in dry THF (2 mL). To this solution HOBt (1.2 x) previously dissolved in dry THF (1 mL) was added, and this mixture was stirred for 10 min at 0°C. Then, DIC (1.2 x) was added and the mixture was stirred for other 30 min at 0°C. The mixture of PLamine and DiPEA was added to the NAC mixture. The reaction was stirred under argon overnight and the temperature was increased to room temperature within 30 min. The reaction run was checked by LC/MS (ESI): $C_{22}H_{31}N_3O_{10}S^-$ $[M\text{-}^1H]^-$, calculated 528, found 528. At the end, the final PLNAC (shown in Figure 2.1 that shown the general chemical strategy) was concentrated *via* rotary evaporation. $^1H\text{-}^1H$ 2D-TOCSY NMR characterization in $CDCl_3$ was performed (see Results and Discussion).

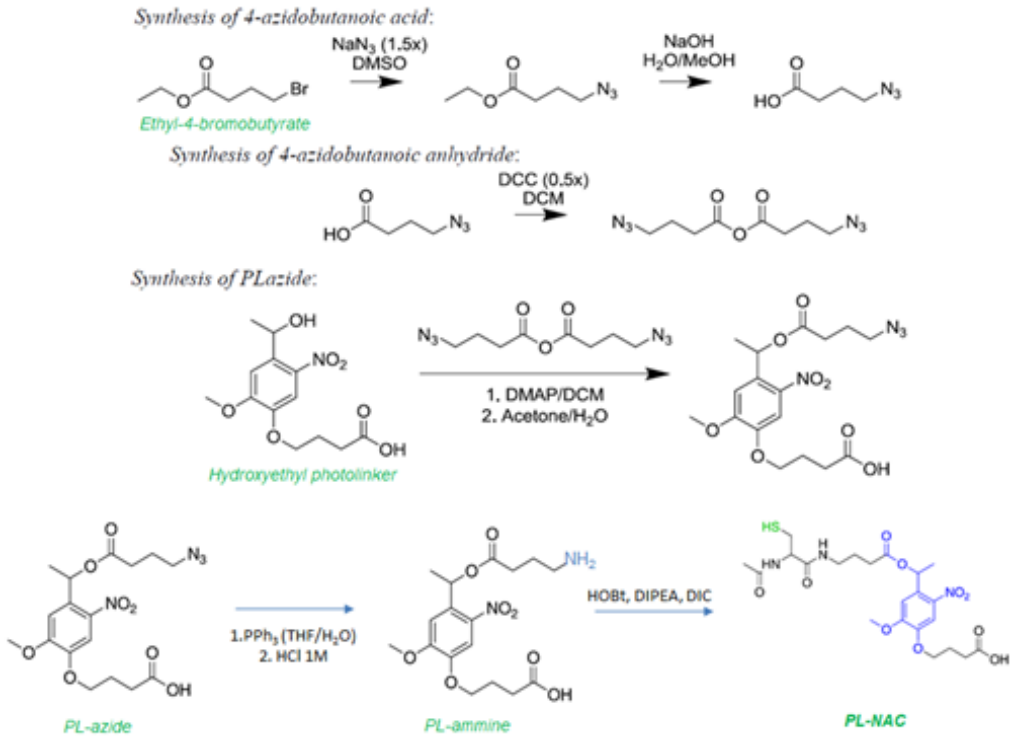

Figure 2.1. Chemical strategy to obtain the photodegradable *o*-nitrobenzyl ether containing a thiol moiety (PLNAC)

Modification of glycol chitosan with photoresponsive linker (PLNAC).

This protocol is as the modification of glycol chitosan with NAC. In fact, it performs the same coupling reaction. So in a flask, 0.05 mmol of glycol chitosan (M_w = 205.21 kDa), in case just modified with a dye, were dissolved in 1 mL of Milli-Q water acidified at pH 5-6. In a different beaker, 0.1 mmol of phoresponsive linker was dissolved in DMSO with the minimum volume required. Then, we added 0.1 mmol of EDC and 0.1 mmol of HOBt to the photolinker solution and we left under stirring for 15 min. The pH was at 5-6. Then, to the solution of GC, we added drop by drop the solution of the activated PLNAC checking that pH is between 5 and 6 and, if necessary, fix it, monitoring it in the first hour of reaction. Then, we let it react overnight at room temperature. After that, pH reaction solution was adjusted at 4. A 70mM TCEP (0.15 mmol) water solution was added to the reaction flask and pH was maintained at a value of 4. The reactions proceeded at room temperature for 1 h. The product was then purified by dialysis (dialysis tubing of 3.5 kDa) four times against water acidified with HCl at pH 4. Each dialysis lasted 2 h or more. The whole purification process ended in two days maximum. Finally, the purified product was freeze-dried for 24 h. The successful functionalization was determined with ^{1}H-^{1}H 2D-TOCSY NMR characterization. Free thiols were determined using the Ellman's test colorimetric assay. To estimate the molar extinction coefficient (ε) of TNB^{2-}, it was performed a calibration curve with standard solutions of PLNAC. For the functionalized glycol chitosan, 0.4 mg was dissolved in 0.5 mL of acetic acid 0.1 M/acetone with a volume ratio of 2.125 and mixed with a solution of 0.2 mg/mL DTNB in a phosphate buffer at pH 8.03. The sample was stored in the dark at 25 °C under stirring for 2 h. Then absorbance of TNB^{2-} was registered at 405 nm using a Varian Cary Scan 100 Spectrophotometer.[8]

Ellman's test for molar extinction coefficient (ε) determination.

The calibration curves for Ellman's test were obtained according to a previous protocol,[8] with some modification for PLNAC in terms of solubility. Briefly, for glycol chitosan with NAC and with PLNAC, the calibration curves for Ellman's tests were obtained using NAC and PLNAC as standard, respectively. NAC was dissolved in acetic acid 0.1 M at different concentrations, while PLNAC in acetic acid and acetone (volume ratio: 2.125) to optimize its dissolution. Then, to 0.5 mL of each standard, 3.5 mL of a solution of 0.2 mg/mL DTNB in 0.5 M buffer phosphate at pH 8.03 were added. The final pH is 7-8, a value necessary for the essay. The baseline was registered at t = 0 to subtract the absorbance due to DTNB at 412 nm for NAC and at 405 nm for PLNAC. In fact, in PLNAC case, the DTNB solution for the baseline measurement was obtained using the appropriate acetic acid/acetone solution in accordance with the same PLNAC solution standards' conditions. Then, standards were stored in the dark at 25 °C under stirring for 2 h. Finally, for each standard the

absorbance and the TNB^{2-} values at 412 nm for NAC and at 405 nm for PLNAC were measured. The absorbance values were fitted to obtain the calibration curves (each measurement was in triplicate).

Solution nuclear magnetic resonance spectroscopy.

For 1D ^{1}H NMR experiments, we used an Agilent 600 MHz spectrometer equipped with a DD2 console and an OneNMR HX probe. GC based samples were prepared at 10 mg/mL in deuterium oxide, containing 1% (v/v) of TFA. Heparin based samples were prepared at 10 mg/mL in deuterium oxide. NMR spectra were recorded with a total of 64 transients and a PRESAT sequence was used to saturate the water residual peak. Spectra analysis was performed using VNMRJ 4.0 software. For PLNAC and GC-PLNAC characterizations we performed a ^{1}H-^{1}H 2D-TOCSY (TOtal Correlated SpectroscopY) experiments.

LbL deposition of polymers on polystyrene carboxylated nanoparticles.

We also performed LbL technique around carboxyl latex beads (PS NPs, 0.5% w/v) as in a previous study.[8] Briefly, monolayer was obtained adding a water suspension (pH 4) of PS NPs (0.5% w/v), under vigorous stirring for 15 min, to a solution of GC (0.04% w/v) in water at pH 4. The volume ratio between water suspension of PS NPs (0.5% w/v) and solution of GC (0.04% w/v) is 1:2. Then, a water solution of heparin (0.128% w/v) at pH 4 was added to an equal volume of monolayer coated nanoparticles suspension (0.16% w/v PS NPs; 0.0256% w/v GC) under vigorous stirring for 15 min. At the end, a trilayer was performed by addiction to a water solution of GC (0.064% w/v) at pH 4, of an equal volume of bilayer-coated nanoparticles suspension (0.08% w/v PSNPs; 0.0128% w/v GC; 0.064% w/v Hep) under vigorous stirring for 15 min. The same procedure was followed with functionalized polymers, such as GC-NAC, GC-PLNAC and Hep-all.

LbL deposition of polymers on oil in water nanoemulsion.

A water solution of nanoemulsion (5 wt%) was added to a solution of GC (0.015% w/v) in water at pH 4 under vigorous stirring for 15 min. The volume ratio between the solutions was respectively 1:4. Then, a water solution of heparin (0.0276% w/v) was added to an equal volume of monolayer coated nanoemulsion suspension (1 wt% oil, 0.012% w/v GC) under vigorous stirring for 15 min. To obtain the final trilayer, the bilayer-coated nanoemulsion suspension (0.5 wt% oil, 0.006% w/v GC, 0.0138% w/v Hep) was added to an equal volume of a water solution of GC (0.0276% w/v) at pH 4 under vigorous stirring for 15 min. The same procedure was followed with functionalized polymers, such as GC-NAC, GC-PLNAC and Hep-all.

Particle size and Z-potential measurements.

We characterized the suspensions using a laser dynamic light scattering (DLS) instrument (λ = 632.8 nm), detecting angle of 173°. All the samples were diluted to a droplet concentration of 0.025 wt% by using Milli-Q water acidified at pH 4 for monolayer and trilayer supensions, and Milli-Q water for emulsions and bilayer suspensions. The calculations of the particle size distribution was performed using a default refractive index ratio (1.59) and 5 runs for each measurement (1 run lasting 100 s). A particle electrophoresis instrument (Zetasizer zs nano series ZEN 3600, Malvern Instruments Ltd., Malvern, U.K.) was used for the Z-potential determinations. Samples were diluted as for the particle size analysis. The Z-potential analysis was carried out by setting 50 runs for each measurement.

Photoinitiator free thiol-ene 'click' reaction and photocleavage of the multilayer conditions.

The suspensions of PS NPs or O/W nano-emulsions coated with polymer multilayer were irradiated with UV light (λ=254 nm) for 1.5 h to perform the photoinitiator free thiol-ene '*click'* reaction. As light source a UV Hand Lamp Spectroline® E-Series UV lamp (output 6 W, wavelength 254 and 365 nm) was used. The light source was at 3 cm distance. A water bath was used to avoid overheating of the solution. Photoreaction was conducted without a photoinitiator.[8] For the photo-cleavage we used a High Intensity Lamp Blak-Ray®UV (Ultraviolet Lamp with Spot Bulb, output 100 W, wavelength 365 nm) and an ice bath was used to avoid overheating of the solution.

Modified Ellman's test.

To determine the reduction of free thiols after irradiation to perform the thiol-ene '*click'* reaction (corresponding to the degree of cross-linkage), in accordance to a previous method,[8] we adopted it with some modifications in employed solvents and volume of sample. 4 mL of PS NPs coated with a bilayer were concentrated by ultracentrifuge (13,000 rpm, 20 min, 4◦C), dissolved in 1.1mL of 0.1M acetic acid and sonicated (10 min, 40 MHz, 50% of power, 4◦C). Half volume was stored at room temperature for 1.5 h in presence of natural light and atmospheric oxygen, while half volume was irradiated. Then, 0.34 mL of each sample were added to 0.16 mL of acetone and 3.5 mL of a solution containing the Ellman's reagent. After 2 h, each sample was centrifuged (13000 rpm, 15 min) and supernatant was collected for UV measurement.

Stability tests on cross-linked O/W trilayer.

In accordance with previous results,[8] we analysed by DLS particle size variations, two systems prepared by LbL depositions of functionalized and non-functionalized polymers on PS NPs as template, before thiol-ene '*click'* reaction, after it and then in PBS 10 mM pH 7.4.

Moreover, such systems were monitored over time to evaluate their stability in PBS 10mM pH 7.4. The systems' stability over time was indirectly determined by DLS particle size variations.

Cryo-TEM Characterization of LbL cross-linked O/W trilayer based on GCPLNAC.

By cryo-TEM we observed the morphology of the LbL cross-linked photo-responsive O/W trilayer. For the preparation of the frozen-hydated sample the plunge freezing method was performed. Briefly a drop of 3 μL of the trilayer were put on a previously glow-discharged 200 mesh holey carbon grids (Ted Pella, USA) after the grid was inserted in the chamber of a FEI Vitrobot Mark IV (FEI company, the Netherlands) at 4°C and 90% of humidity. The droplet of sample was blotted with filter paper for 1 s, (blot force 1, drain time 0,5 s) and then the grid was plunged into the liquid propane. The grid was then stored in liquid nitrogen in a grid box until it was finally transferred to a cryo-specimen 626 holder (Gatan, Inc., USA) and loaded into the cryo-transmission electron microscope for imaging. To obtain the image of the nanoparticles we used a Tecnai G2 20, a cryo-tomo transmission electron microscope (FEI company, the Netherland) equipped with LaB6 emitter (acceleration voltage of 200 kV) and recorded at with a 2 k × 2 k CCD-Eagle 2HS camera. The Frozen-hydrated sample is radiation-sensitive material so to avoid damaging, the observation was carried out in Low Dose Mode.

Confocal analysis of oil core - cross-linked LbL trilayer shell based on GCPLNAC.

The cross-linked trilayer built onto the O/W nanoemulsion containing the photo-linker (25μL in 1mL PBS 10mM pH 7.4) and the last layer labelled with RhodB was put (50μL) on a coverglass for 10 min to allow it to adhere to the surface. After that, the solution droplet is removed from the coverglass which is covered with a microscope slide, in a central region where we had loaded 10 μL of PBS 10mM pH 7.4. Images of the sample were captured with a Leica TCS SP5 Laser Confocal Scanning microscope (Leica-Microsystems, Mannheim, Germany) with a Plan Apo 100x/1.4 oil immersion objective using a 543nm HeNe excitation laser and detecting 560-610nm emission. Images were acquired with a field of view 77.5 x 77.5 μm for a pixel size of 76 x 76 nm. Images were visualized by LAS-AF software (Leica-Microsystems, Mannheim, Germany).

Tests of photocleavage on cross-linked trilayer

Before starting the photocleavage tests of our cross-linked photo-responsive trilayers, we checked if the thiol-ene 'click' conditions (254 nm for 1.5 h) could damage the photodegradable unit of the linker (PL azide) and also we checked its rupture in the photocleavage conditions (365 nm), as just demonstrated in a previous work.[33] We compared ^{1}H NMR spectra in $CDCl_3$ of untreated PLazide, a PLazide first irradiated at 'click' reaction conditions and then at 365 nm for 30 min.

The destabilization of the cross-linked trilayer containing the photolinker and built on O/W nanoemulsion was evaluated starting from the trilayer 0.25 wt% oil, 0.003% w/v GCPLNAC, 0.0069% w/v Hep-all, 0.0138% w/v GCPLNAC, dissolved in PBS 10mM pH 7.4, as 'simil' physiological medium. In particular, 25 μL of that system were put in 1 mL PBS and then this solution was irradiated with High Intensity Lamp Blak-Ray®UV as explained above. The times of exposition were 2 h in steps of 30 min and 10 min of rest between the different steps. We used an ice bath to avoid overheating and refilled it after each step of rest. The destabilization was monitored by DLS particle size variations of the same sample in analysis. To confirm the results the same tests were performed on a cross-linked trilayer with a linker no light sensitive and based on O/W nanoemulsion. So the system was the trilayer 0.25 wt% oil, 0.003% w/v GCNAC, 0.0069% w/v Hep-all, 0.0138% w/v GCNAC.

FRET analysis for photocleavage detection.

Another approach to detect photocleavage was based on using fluorescence lifetime analysis on cross-linked trilayers containing the photolinker and built on O/W NE as mentioned above but with Hepall-FITC and GCPLNAC-RhodB as second and third polymers. Specifically, it was exploited the FRET (Fluorescence Resonance Energy Transfer) occurrence between the two polymer-labelling fluorophores, where FITC is the donor and RhodB is the acceptor, which is known to produce variations of donor lifetime on the basis of the distance between them.[40] A comparison of lifetimes and FRET efficiencies was performed on the same cross-linked trilayer in PBS solutions in two different conditions: irradiated with 365 nm wavelength as explained above for 1.5 h (in steps of 30 min, 10 min of rest and ice bath for temperature control) and non-irradiated. Samples loading on coverglass was the same described in "Confocal analysis" section. For further control, the same FRET analysis in the same conditions was performed on cross-linked trilayer with a linker non light sensitive, so with GCNAC as first layer, and Hepall-FITC and GCNAC-RhodB as second and third polymers. FITC reference lifetime was measured on a GC-HepallFITC polymers deposition on coverglass.

A laser scanning confocal microscope TCS SP5 SMD (Leica Microsystems, Germany) equipped with a Chameleon Ultra II 80MHz pulsed NIR laser (Coherent Inc., US) that was the laser source used for performing FLIM (Fluorescence Lifetime Imaging) experiments, was used. An HCX IRAPO L *25x/0.95* water immersion objective was used for all the experiments exciting FITC donor at 740 nm and detecting emission at 500-530 nm whereas RhodB acceptor was excited at 840 nm and its emission was detected at 560-610 nm. LAS-AF software was used for exporting pre-histogrammed FLIM data that were then elaborated by the FLIM fit software 5.1.1,[40] for calculating lifetime values. To evaluate the lifetime (τ) of the FITC donor we adopted a method of LbL polymer layers deposition on coverglass, reported in literature[41] but with some modifications, in particular in the choice of the solvents, in accordance with our purpose, so we prepared a bilayer of GC and Hepall-FITC. Briefly, we used a coverglass (14 mm) as substrates to build the bilayer films. We diluted GC 1%w/v and Hepall-FITC 1%w/v to 0.1%w/v in the respective solvents (acid water pH 4 for GC and milliq water for Hep). LbL deposition started with GC 0.1%w/v (200 μL for 20 min of deposition). Then, we removed the polymer solution from the coverglass and continued with a washing step (200 μL of acid water pH 4 for 10 min). Then, also this solvent was removed and we started with the second polymer film (200 μL of Hepall-FITC 0.1%w/v for 20 min), and continued as for the first layer but using for the washing step, Milli Qwater. Before putting the coverglass on the microscope slide, we repeated another washing with abundant water to a complete removal of polymer residues and to obtain a good deposition and imaging of the LbL thin films.

Cell viability.

The cytotoxicity effects of nutraceuticals-loaded nanoemulsions was studied on human skin melanoma cell line A375.S2 (ATCC® CRL-1872™), obtained from American Type Culture Collection (Manassas, VA, USA), looking at their mitochondrial dehydrogenase activity by means of a modified MTT [3-(4,5-dimethyldiazol-2-yl)-2,5- diphenyltetrazoliumbromide] method according to the manufacturer's instructions (Dojindo Molecular Technologies Inc., Rockville, MD). A375.S2 cells were grown in Dulbecco modified Eagle's medium (DMEM) with 10% (V/V) heat inactivated FBS, penicillin G (100 U/mL), and streptomycin (100 mg/mL) in 96-well plates at a density of 10000 cells per well at 37°C in a humidified 5% CO_2 atmosphere. After 24 h of appropriate growth we tested the following solutions in full medium and added them to the cells after washing with PBS: Photo-responsive cross-linked trylayer on nanoemulsions (all loaded with curcumin ranged from 0,05 up to 5 μg/mL) were pre-incubated for 2 or 4 or 6 h with melanoma cells; after, cells were washed (or not washed) slowly with PBS, irradiated with UV for 3 min under sterile conditions (under biological cappa) and allowed to grow at standard conditions for 24 or 72 h. We decided to irradiate

cells only for 3 min with UV because of the biological safety of this irradiation time (data not shown); in fact irradiating cells (with or without incubated curcumin) with UV for 3 min cell viability did not change and did not change also the biological activity of curcumin so on the basis of these data we are sure that the biological effects observed in this study were due to the effects of UV on the nanocarriers structure or interactions with intracellular microenvironment making curcumin potentially more bioavailable in the cell cytoplasm. Moreover, at the end of the incubation period, the cells were washed three times with PBS at pH 7.4 and incubated with 100 µL of a MTT solution (0.5 mg/mL in cell culture medium) for 4 h at 37 °C. The absorbance readings were acquired at a wavelength of 450 nm with the Tecan Infinite M200 plate-reader using I-control software. The relative cell viability (%) was calculated by the formula $[A]_{test}/[A]_{control}\times100$, where "$[A]_{test}$" is the absorbance of the test sample, and "$[A]_{control}$" is the absorbance of the control cells incubated solely within culture medium. After evaluating cell cytotoxicity, the total protein content was measured by using the Micro BCA protein assay kit (Pierce). Briefly, the cells were washed with ice-cold PBS, and incubated for 15 min in 150 µL cell lysis buffer (0.5% v/v Triton X-100 in PBS), to which 150 µL of Micro BCA protein assay kit reagent (prepared following the instructions of the manufacturer) were added. The absorbance at 562 nm was finally measured on a plate reader. The cytotoxicity measurements were then normalized by the amount of total protein content in each well.

Cellular uptake quantification.

A375.S2 cells were grown in Dulbecco modified Eagle's medium (DMEM) with 10% (V/V) heat inactivated FBS, penicillin G (100 U/mL), and streptomycin (100 mg/mL) at 37 °C in a humidified 5% CO_2 atmosphere. For uptake experiments, $5x10^3$ cells/well were seeded in 24-well plate and allowed to grow for 24 h. The medium was then replaced with 0.1 mL of a solution based on fluorescent photo-responsive cross-linked or non-functionalized trylayer nanoemulsions dissolved in culture medium and allowed to incubate for a time comprised between 0.5 and 24 h. Cells were then washed twice with PBS (pH 7.4) and after specified time intervals, the experiments were terminated by removing the supernatant, washing the cells three times with 10 mM PBS and lysing the cells with 0.1 mL of 0.5% Triton X-100 in 0.2 N NaOH. The membrane-bound and internalized fluorescent nanoemulsions were quantified by analyzing the fluorescence of the cell lysate (λ_{exc} = 485 nm, λ_{em} = 535 nm), employing a calibration with 0,001-5% oil of fluorescent nanoemulsions dispersed in a cell lysate solution (10^6 untreated cells dissolved in 1 mL of the Triton X-100/0.2 N NaOH solution).

2.3 Results and discussions

The first part of the results and discussion regard the chemical modification and characterization of the polymers used then it follows a part regarding the stability of the multilayer shell cross-linkage and finally a part regarding the assessment of photo-responsive activity of the nanocarrier.

^{1}H-^{1}H 2D-TOCSY NMR characterization of PLNAC and GCPLNAC.

PLNAC was prepared according to the procedure reported in the 'Materials and Methods' section. PLNAC was different from PLN_3 for the presence of NAC exclusively. In fact, from ^{1}H-^{1}H 2D-TOCSY spectra (PLNAC in $CDCl_3$, Figure 2.2) we observed that the group of peaks at 4.11 ppm, 2.53 ppm, 2.15 ppm can be assigned to -$OCH_2CH_2CH_2COOH$ group and the chemical shifts are not different from those attributed to the same group in PLN_3. Instead, the group of peaks at 3.65 ppm, 1.50 ppm and 1.42 ppm can be assigned to –$CH_2CH_2CH_2$- group linked to the amidic bond. In fact, in this case there is a shift of the signal because of the substitution of the azide with a different bond, the amidic bond which links the –$CH_2CH_2CH_2$- group to the NAC. Finally, the group of peaks at 3.75 ppm and 1.84 ppm can be assigned to the –CH-CH_2- in the NAC.

After a coupling reaction between glycol chitosan and PLNAC, the GC-PLNAC polymer was characterized by ^{1}H-^{1}H 2D-TOCSY NMR analysis (Figure 2.3). In this case, as described above, the polymer was dissolved in deuterium oxide, containing 1% (v/v) of TFA, so it is obviously to observe different chemical shifts for the groups of PLNAC just analysed. However, PLNAC is clearly recognizable by the peaks at 3.15 ppm, 2.30 ppm, 1.72 ppm (–$CH_2CH_2CH_2$- group) and the peaks at 4.11 ppm, 2.49 ppm, 2.06 ppm (-$OCH_2CH_2CH_2COOH$ group). The group of peaks between 3.4-3.9 ppm can be attributed to the proton in position 2, 3, 4, 5 and 6 of chitosan glucosamine units. Other signals are covered by polymer's ones.

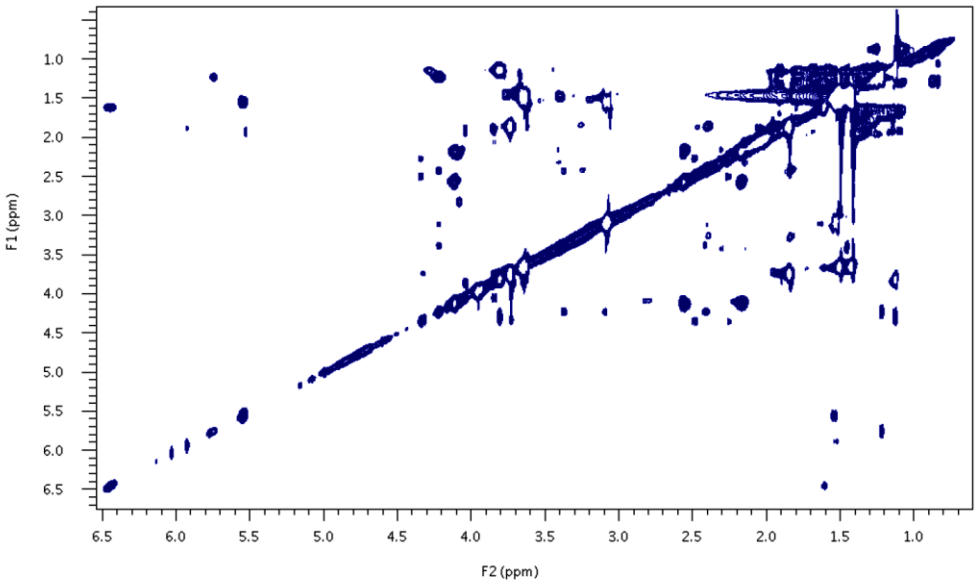

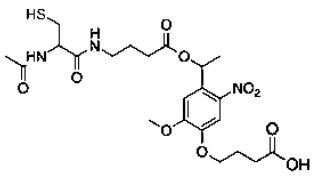

Figure 2.2. ^{1}H-^{1}H 2D-TOCSY spectra of PLNAC (on left) in $CDCl_3$.

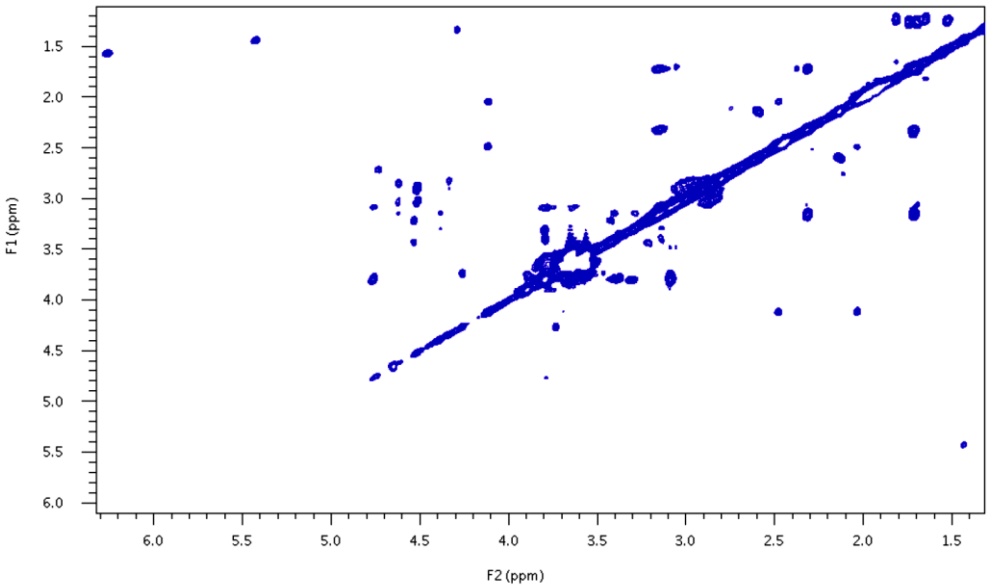

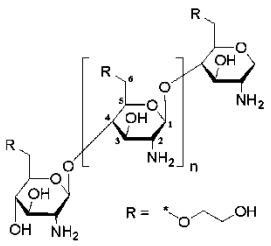

Figure 2.3. ^{1}H-^{1}H 2D-TOCSY spectra of GCPLNAC (on left GC structure) in D_2O/TFA 1% (v/v).

Ellman's test calibration curves and free thiols in glycol chitosan with NAC and PLNAC.

As said in Materials and Methods, we measured the absorbance and the TNB^{2-} values at 412 nm for NAC and 405 nm for PLNAC. Then, these values were fitted to obtain the calibration curves (each measurement was in triplicate, Figures 2.4 and 2.5). For NAC the ε value of TNB^{2-} at 412 nm was $1.3664 \cdot 10^4$ M^{-1} cm^{-1}. For PLNAC the ε value of TNB^{2-} at 405 nm was $1.9646 \cdot 10^4$ M^{-1} cm^{-1}. Starting from these values of ε, we calculated the degree of free thiol in GCPLNAC and GCNAC as explained in Materials and Method, and in both cases the polymers showed ~ 6% of free thiols.

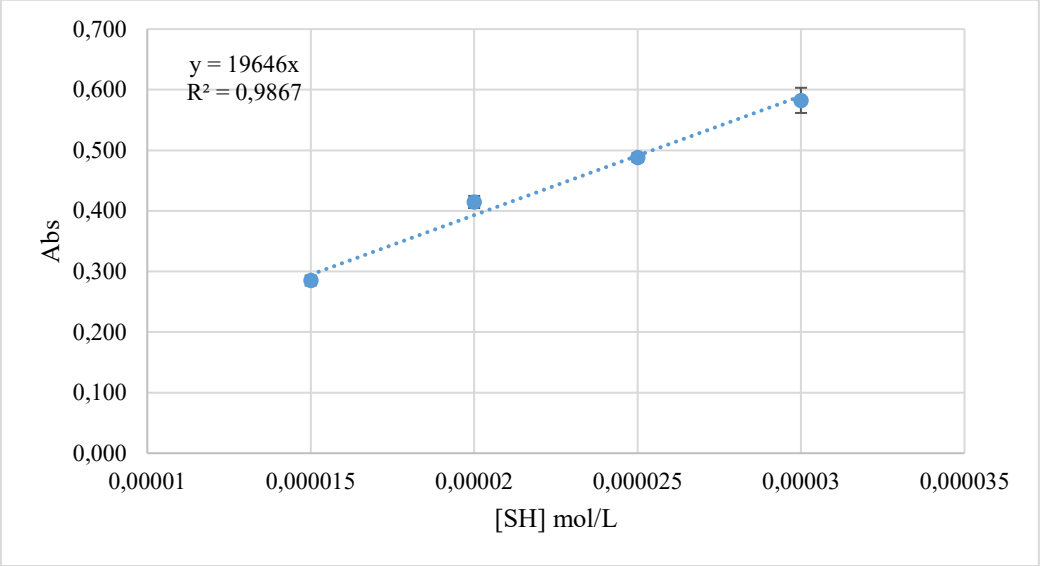

Figure 2.4. Calibration curve to determinate molar extinction coefficient for Ellman's test of GCPLNAC.

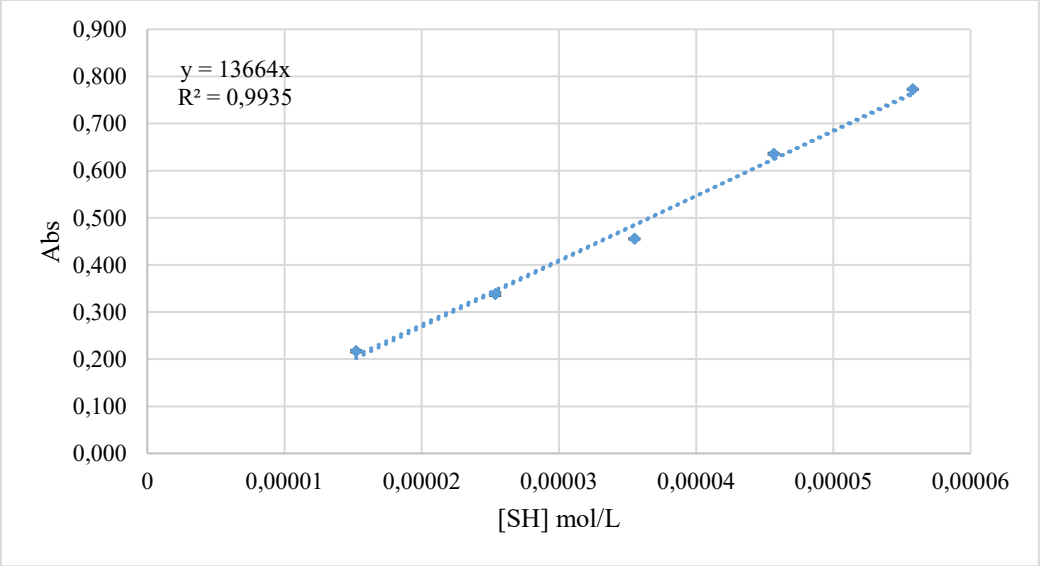

Figure 2.5. Calibration curve to determinate molar extinction coefficient for Ellman's test of GCNAC.

Ellman's test to demonstrate the cross-linkage on a bilayer on PS NPs with functionalized polymers.

In a previous work by our team,[8] we had already demonstrated that with NAC and allyl modified polymers, a covalent cross linkage among successive layers could be performed by a thiol-ene photoinitiatior free reaction at room temperature in the presence of oxygen. In that study, we started from a bilayer of N-acetylcystein glycol chitosan and allylated heparin on PS NPs deposited *via* LbL. Then, a modified Ellman's test was performed before and after irradiation determining the relative reduction of free thiol groups corresponding to the amount of thio-ether bonds formed. Thanks to their rigidity and therefore their ability to be separated by centrifuge, PS NPs were chosen as template instead of O/W nanoemulsion for that characterization study.

In this study, we had repeated this test with the same purpose to demonstrate the cross-linkage between the shells through the reduction of the free thiol groups. However, in this case the system is different because for the bilayer preparation on PS NPs we have used the synthetized photo-linker conjugated on glycol chitosan. In particular, the test was performed both on irradiated (90 min at 254 nm), i.e. crosslinked, and non-irradiated, i.e. non-crosslinked bilayer systems. The experimental conditions are reported in Materials and Methods. By TNB^{2-} UV analysis, we observe the expected reduction of free thiol (red lines in the Figure 2.6) demonstrating, also in this study, cross-linkage in absence of photoinitiator.

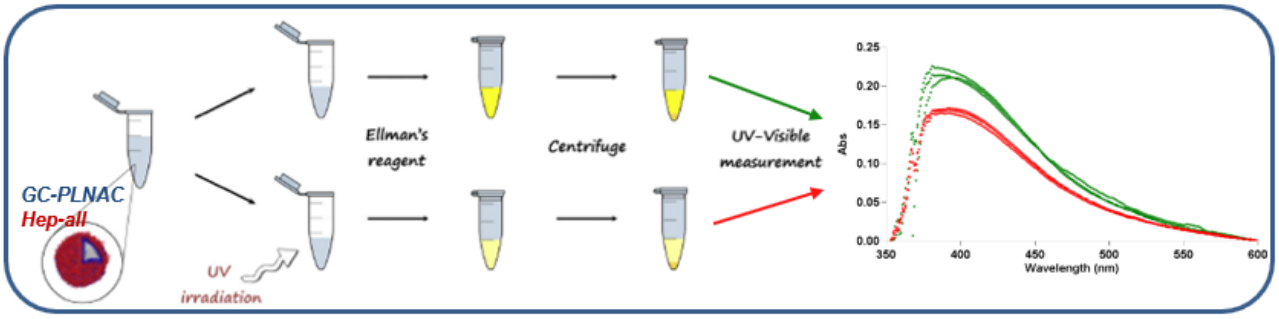

Figure 2.6. Schematic representation of the modified Ellman's test on crosslinked (red) and non-crosslinked PS NPs bilayer. The relative reduction of free thiols indicates the formation of the thioether. The tests were repeated three times.

Cross-linkage stability tests.

In accordance with previous results,[8] we prepared *via* LbL two trilayer systems with functionalized and non-functionalized polymers on PS NPs as template. Both of them were investigated by DLS analysis. In both cases (see Figure 2.7), we have the confirmation that irradiating at 254 nm for 90 min (photoinitiator free thiol-ene '*click*' reaction conditions), with an ice bath to control the overheating, the stability of the systems is preserved. While a media change, using PBS 10 mM pH 7.4, after irradiation at 254 nm, brings to a destabilization of the non-functionalized systems. On the other hand, a functionalized and so cross-linked system, retains its integrity also in PBS even if we observe a slight swelling probably connected to weaker interactions when PS NPs are used as template.

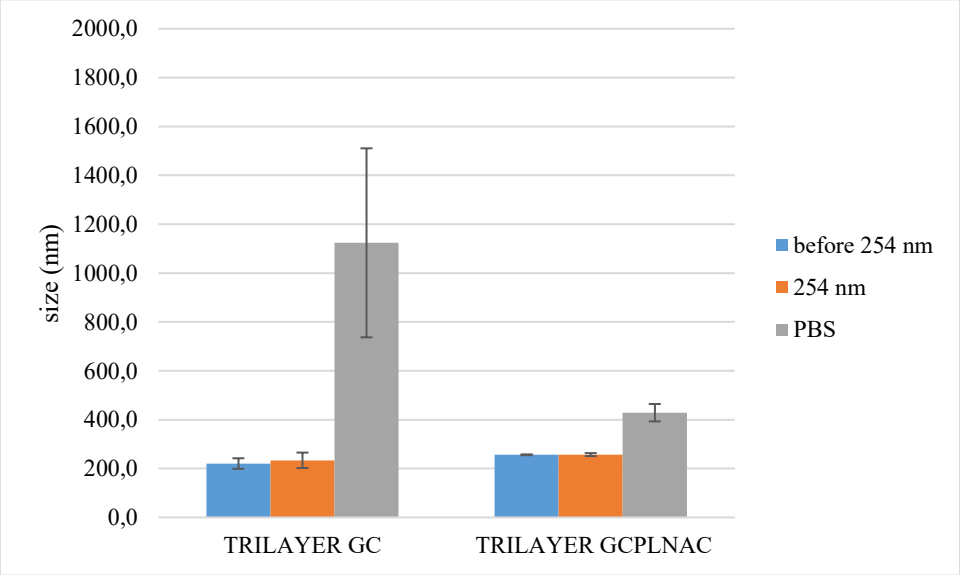

Figure 2.7. Comparison of size measurements between non-functionalized polymers system and functionalized and cross-linked polymers systems sample: blue, samples dispersed in water at pH 4 before 254 nm; orange, samples dispersed in in water at pH 4 after 254 nm for 90 min; grey, samples after 254 nm for 90 min dispersed in 10 mM phosphate buffer solution at pH 7.4. Error bars indicate the standard deviations.

DLS stability tests on cross-linked O/W trilayer.

As previously described, to perform the stability and cleavage tests of the final system we used cross-linked trilayer built on O/W NE, leaving the PS NPs, which were only a model template. Indeed, the cross-linked trilayer built on O/W nanoemulsion is the real drug delivery system developed in this project.

Normal and cross-linked trilayer based on O/W nano-emulsions containing GCPLNAC as first and third shell, were monitored over 20 days to evaluate their stability in PBS 10 mM pH 7.4.

Table 2.1. Average DLS particle size data of non-crosslinked and crosslinked O/W GCPLNAC trilayers.

day	non-crosslinked (nm)	crosslinked (nm)
0	111,9 ± 2,6	106,2 ± 2,3
3	115,8 ± 1,2	109,0 ± 2,7
7	116,7 ± 0,9	109,3 ± 1,5
14	128,4 ± 3,0	110,0 ± 1,6
20	130,2 ± 1,3	111,1 ± 3,5

As shown in Table 2.1, DLS particle size analysis of the non-crosslinked and crosslinked systems show a swelling of the non-crosslinked one over the days but the crosslinked systems preserve their size. This is an indirect demonstration of the higher stability provided by the cross-linkage to the nanocarrier. It has to be noted that physiological environment is more complex than PBS providing many more mechanisms of degradations that can destroy a multi-layer in absence of a chemical cross-linkage.

Results of cryo-TEM characterization of LbL cross-linked O/W trilayer based on GCPLNAC.

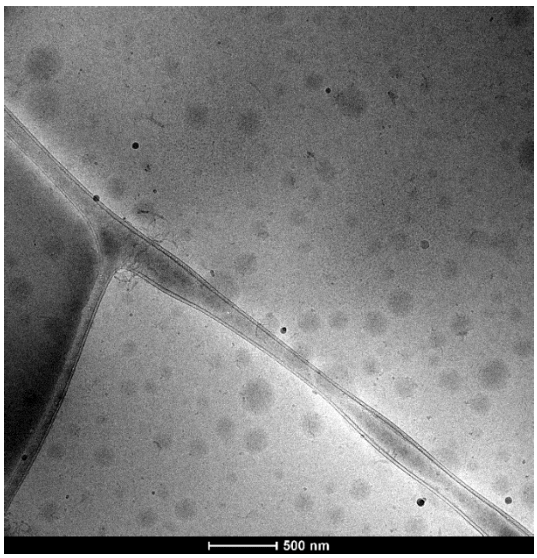

Figure 2.8. Cryo-TEM image of an example of LbL O/W cross-linked photo-responsive trilayer.

Cryo-TEM characterization of the LbL cross-linked photo-responsive trilayer (Figure 2.8) shows the uniform morphology of the systems and the accordance with DLS size measurements. Cryo electron microscopy gives the possibility to preserve the native state of the samples by rapid freezing of suspensions. This process is known as vitrification. Cryo-TEM images were collected to investigate

the shape and the distributions of the LbL cross-linked photo-responsive trilayer. In all images obtained, sample is always embedded in a solid matrix, to give the possibility to have a good characterization of a soft nanocarrier like the oil core based one exploited in this project. As shown in the image (Figure 2.8) LbL cross-linked photo-responsive trilayers are spherical with a uniform morphology in the size range of ~ 50–200 nm. These values agreed with the LbL cross-linked photo-responsive trilayer size data obtained by DLS.

Photocleavage conditions for photolinker.

As mentioned above, glycol chitosan was modified introducing a thiol moiety *via* a coupling reaction with PLNAC. Moreover thanks to this chitosan functionalization, it was possible to obtain a cross-linked LbL system with a photoinitiator free thiol-ene '*click'* reaction between the thiol moiety on glycol chitosan and the double bond on the allylated heparin. Therefore, photolabile linker was inserted between the polymers of the LbL, and tested at 365 nm in terms of ability to be cleaved irreversibly, thus, resulting in the destabilization of the multilayer and the release of the drug. As explained in Materials and Methods, before starting the photocleavage tests of our cross-linked photo-responsive trilayers, by ^{1}H NMR analysis we checked the behaviour of the photodegradable unit of the linker (PLazide) in the cross-linkage (photoinitiator free thiol-ene '*click'* reaction, 254 nm 1.5 h) and photocleavage (365 nm) conditions. The mechanism of photocleavage is shown in Figure 2.9 and was demonstrated in a previous work.[33] So to verify PLazide integrity at 254 nm, i.e. in the photoinitiator free thiol-ene '*click'* reaction conditions, we compared ^{1}H NMR spectra in $CDCl_3$ of untreated PLazide, a PLazide first irradiated at '*click'* reaction conditions and then at 365 nm for 30 min. For simplicity of explanation, we report the superimposed spectra of the linker treated at the two wavelengths (Figure 2.10). In the conditions of the '*click'* reaction, the linker shows only a slight rupture (not more than 20%, red line). That is, this spectrum is practically identical to that of untreated PLazide. At 365 nm (blue line) instead, it is possible to see a shift of all signals, the break is 80% in 30 min. In particular, considering the products of the scission reaction, the characteristic peaks of the rupture are highlighted in the spectrum.

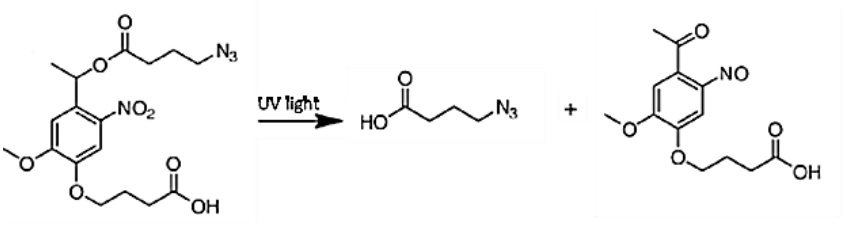

Figure 2.9. Photocleavage mechanism of PLazide.

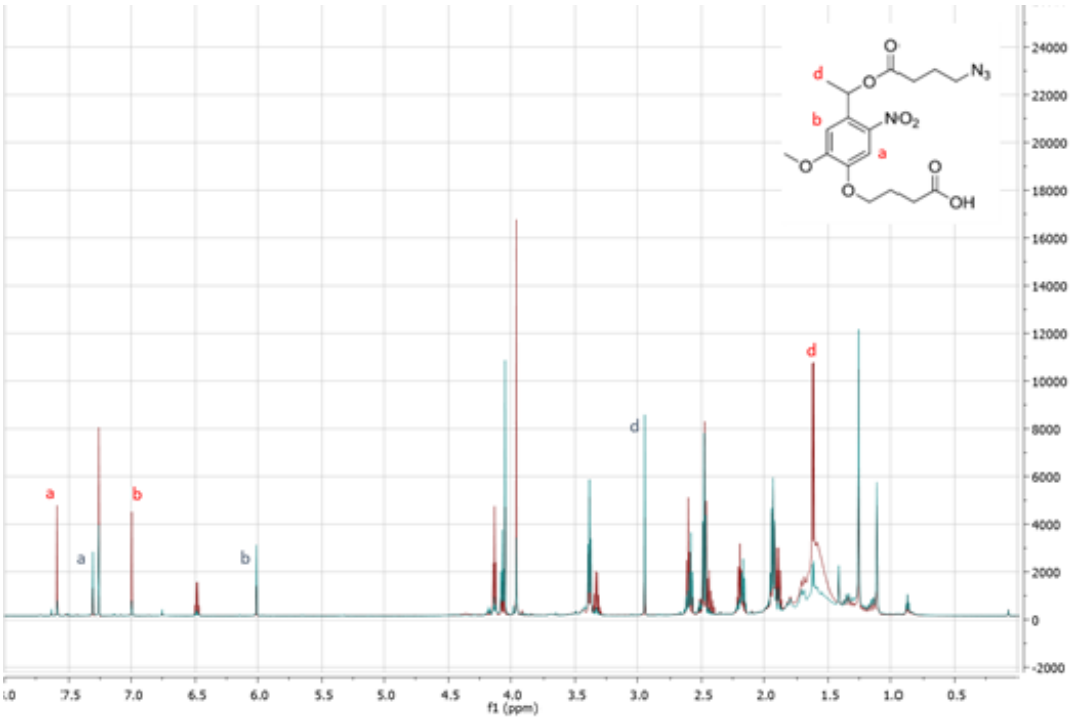

Figure 2.10. ^{1}H NMR of PLazide: red line, PLazide at 254nm for 90 min; blue line, PLazide at 365 nm for 30 min.

Results of photocleavage on cross-linked trilayer.

As described above, we had evaluated the effect of the irradiation at 365 nm on the cross-linked trilayer composed by GCPLNAC, Hepall, GCPLNAC (25 µL in 1 mL PBS 10mM pH 7.4). We irradiated at 365 nm for 2 h in steps of 30 min and 10 min of rest and we observed a swelling of the trilayer (Figure 2.11). We selected this strategy of irradiation because in preliminary experiments (data no shown) we noticed that a combination of irradiation and rest steps, improve the swelling of the nanocapsules. Very probably, we observe only a swelling, because despite the photo-linker cleavage, the electrostatic interactions among the polymeric shells and oil core tend to preserve in part the system's integrity. However, the cross-linkage and the next photo-swelling permit a controlled release of the capsules (as shown in the biological study). Moreover, this test shows that the irradiation of the system in step of 30 min and 10 min of rest brings to a more marked swelling in 1.5 hours. For this reason, we choose this time and method of irradiation for our next investigation and characterization.

The same experiment of irradiation at 365 nm was performed on a cross-linked O/W trilayer composed by GCNAC, Hepall, GCNAC. In this case, no variation can be observed on the capsules after irradiation. This result confirms that the swelling of cross-linked GCPLNAC trilayer is connected to the cleavage of the photo-linker. Indeed, in the same system but with GCNAC, meaning a polymer with no any photo-cleavable linker, the irradiation does not bring any destabilization (Figure 2.12).

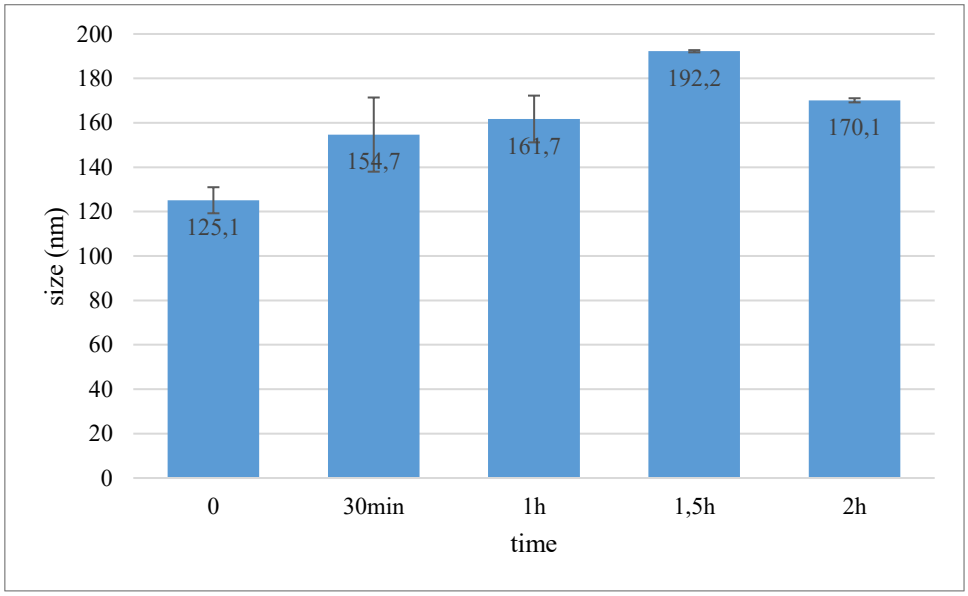

Figure 2.11. Cross-linked trilayer composed by GCPLNAC irradiated for 2h in steps of 30 min and 10 min of rest.

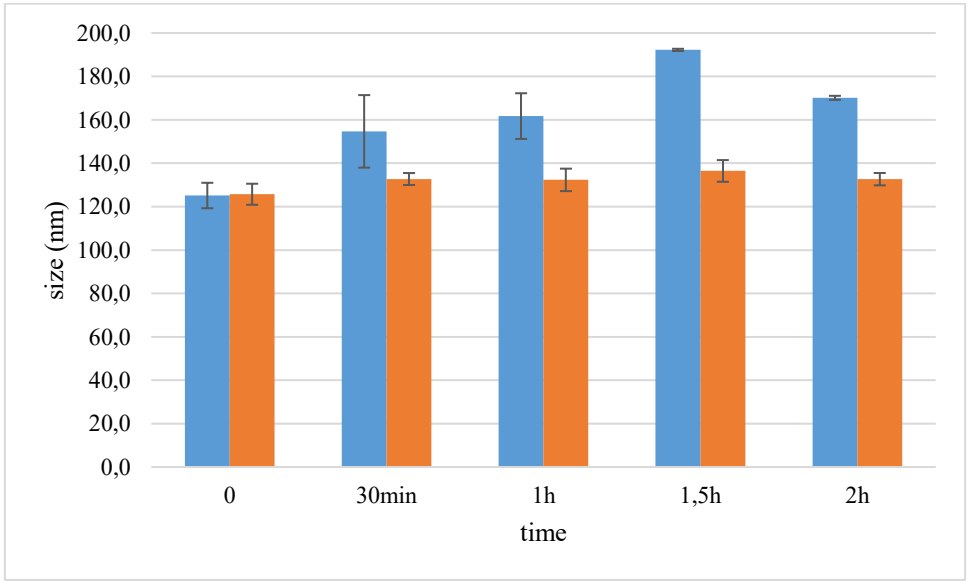

Figure 2.12. Comparison between irradiated cross-linked trilayer for 2h in steps of 30 min and 10 min of rest.

Blue bars: GCPLNAC trilayer – Orange bars: GCNAC trilayer.

Confocal characterization and FRET analysis for photocleavage detection in LbL cross-linked trilayer based on GCPLNAC built on O/W nanoemulsions.

As described in Materials and Methods, we used confocal analysis to acquire an image of the distribution of the cross-linked trilayer containing the photo-linker built on the O/W nanoemulsion and diluted in PBS 10 mM pH 7.4. Clearly, the image (Figure 2.13) shows the accordance with our expectations: uniform distribution and good deposition.

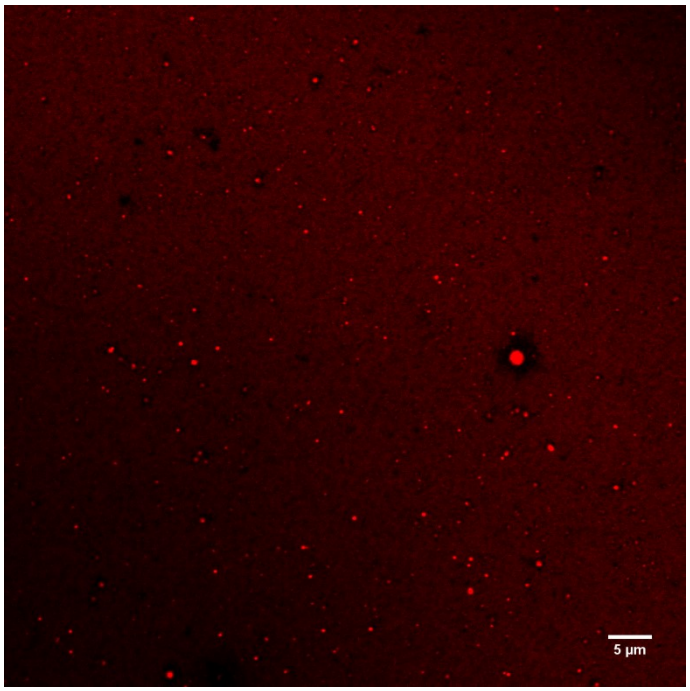

Figure 2.13.Confocal analysis of cross-linked O/W trilayer containing the photo-linker dispersion in PBS and with the last layer labelled with rhodamine B.

In Figure 2.13, we show an image of our cross-linked photo-responsive trilayer diluted in PBS 10 mM pH 7.4, with the last layer labelled with RhodB. However, we have abandoned the confocal analysis for the study of photo-cleavage at 365 nm of the irradiated and non-irradiated cross-linked trilayers, photo-responsive and not. In fact, having verified from the DLS data that 365 nm exposure involved a swelling with a dimensional increase of much less than 200 nm, this was expected to be not appreciable with the optical microscopy. Therefore, we switched to FRET analysis to confirm the swelling observed by DLS after 365 nm irradiation in the photo-responsive cross-linked trilayer respect to no-photo-responsive one.

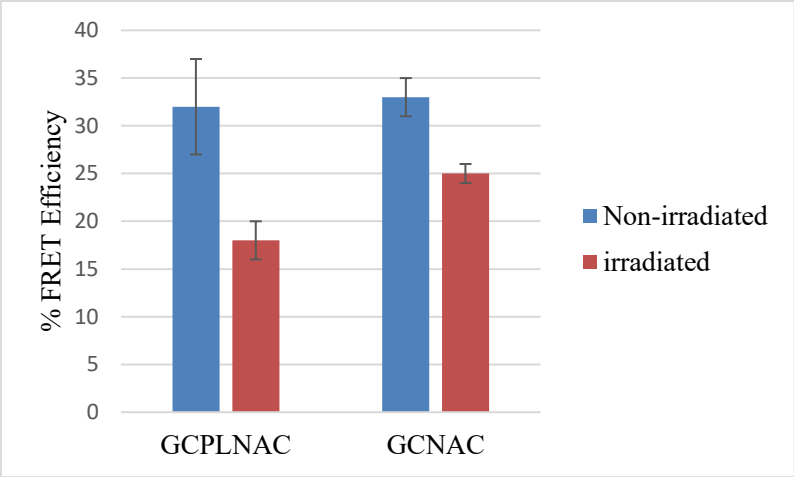

Figure 2.14. % FRET Efficiency (donor FITC/ acceptor RhodB) - Condition of irradiation: Cross-linked trilayers were in PBS 10 mM pH 7.4. Irradiated for 1.5 h in steps of 30 min and 10 min of rest at 365 nm in an ice bath.

Table 2.2. % Averages of FRET Efficiency of the photo-responsive and no-photo-responsive LbL cross-linked trilayers based on GCPLNAC and GCNAC: before and after 365 nm irradiation.

FRET Efficiency (%)		
sample	**% E_{FRET}**	**% st.dev.**
irradiated GCLINKER	18	2
irradiated GCNAC	25	1
no-irradiated GCLINKER	32	5
no-irradiated GCNAC	33	2

The FRET efficiency was calculated by the following equation:

$$E_{FRET} = (\tau_{donor} - \tau_{donor\text{-}acceptor})/\tau_{donor}$$

where the reference τ_{donor} is that of FITC on allylated heparine in the absence of RhodB and therefore of any FRET. τ_{donor} was evaluated by polymers deposition on coverglass as described in Materials and Methods and was 3.56ns. While $\tau_{donor\text{-}acceptor}$ was that of the tested samples. As shown in the Figure 2.14, after 1.5 h of 365 nm irradiation the cross-linked photo-responsive trilayer based on GC-PLNAC in PBS 10 mM pH 7.4 showed a significant decrease of FRET efficiency, which was calculated respect to the non-irradiated sample. This result is in agreement with the swelling of the nanocapsules seen by DLS analysis, and can be explained by the cleavage of the photolinker. Conversely, the cross-linked non-photo-responsive trilayer based on GCNAC upon the same treatments showed only a weak decrease of the FRET efficiency (see Table 2.2). This result far from being in contrast with the DLS measurements where the non-photo-responsive systems was shown

stable in the irradiation's conditions, could be explained by an expected sensitivity of donor acceptor pair to a photochemical effect of UV irradiation at 365 nm able to change the lifetime of the donor even if the donor-acceptor distance remains the same as expected in the non-swelling case.

Cellular uptake quantification and cell viability studies.

As previously reported,[42] the cellular uptake of fluorescent nanocarriers is time-dependent. Here, after 2 h of incubation, approximately 30–35% of photo-responsive cross-linked and non-functionalized trilayer nanoemulsion were internalized or adhered to the membrane of A375.S2 cells (Figure 2.15). After 6 h of incubation, around 70-75% of both the systems were internalized and started a quite-plateaux curve (Figure 2.15). This is the reason why we decided to adopt 6 h of internalization as the superior limit in our cellular experiments when to start with UV stimulation.

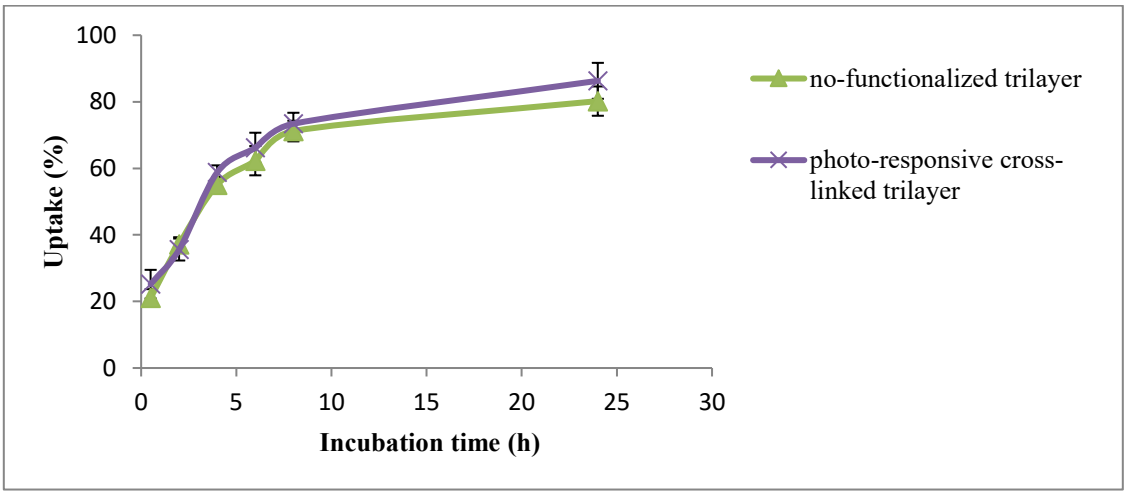

Figure 2.15: Melanoma cellular uptake of photo-responsive cross-linked and non-functionalized trilayer nanoemlsions incubated from 0,5 up to 24 h.

On the other hand, focusing on our photo-responsive cross-linked trilayer having the oil core loaded with curcumin, the cytotoxicity measurements are in accordance with the fact that in 6 h of pre-incubation before UV irradiation (365 nm) there is a complete internalization. In fact, in Figure 2.16 and 2.17 we compare the photo-responsive cross-linked trilayer loaded with curcumin at different time of pre-incubation (2 h, 4 h, 6 h) with melanoma cells and we compared washed or no-washed conditions after this pre-incubation time and UV exposure in terms of cell viability at 24 and 72 h. In both cases, we observe that for 2 h or 4 h of pre-incubation, the washed systems are less toxic than no-washed ones, while for 6 h of pre-incubation, there are not differences between washed and no washed conditions, so the washing step does not change the cellular results, both for 24 or 72 h of culture. Therefore, we can be sure that in 6 h of pre-incubation, there is the maximum internalization.

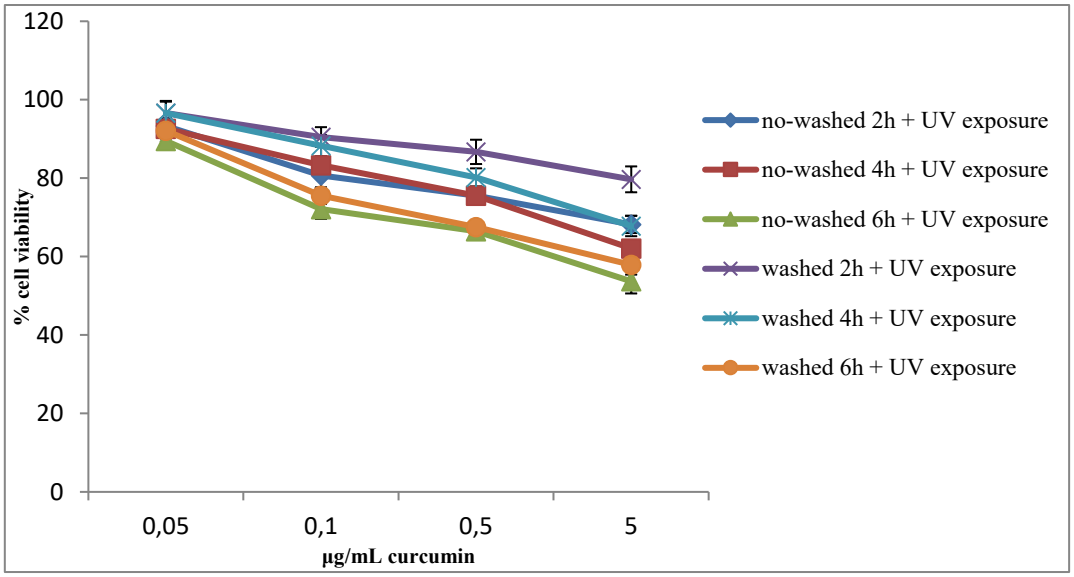

Figure 2.16. Growth condition: 24 h. Photo-responsive cross-linked trilayer loaded with curcumin (range of curcumin concentrations from 0.05 to 5 µg/mL) for different times of pre-incubation, washed or no-washed, then expose to UV.

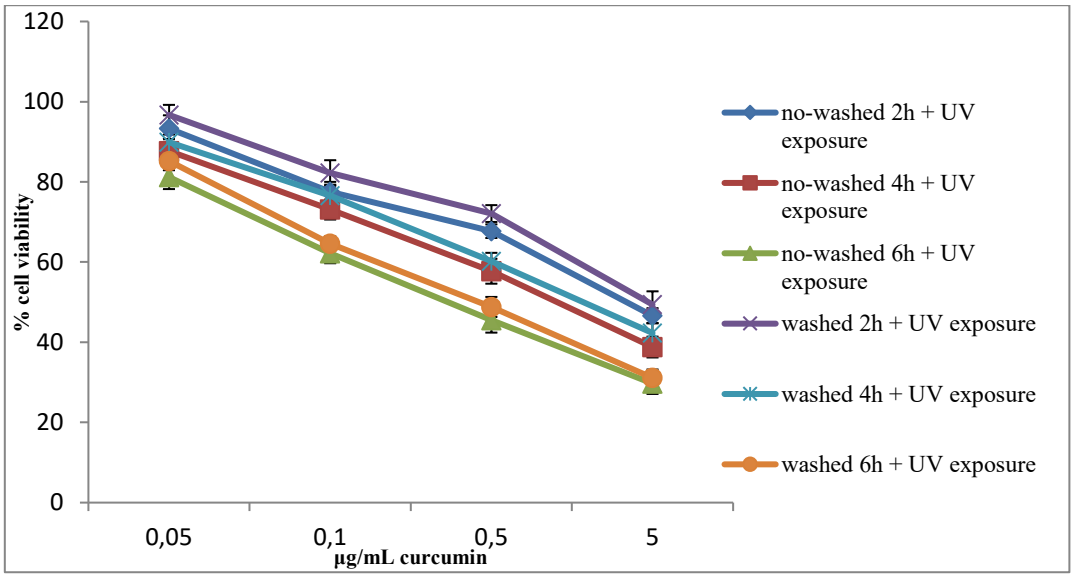

Figure 2.17. Growth condition: 72 h. Photo-responsive cross-linked trilayer loaded with curcumin (range of curcumin concentrations from 0.05 to 5 µg/mL) for different times of pre-incubation, washed or no-washed, then expose to UV.

For what we have just said above, the next presented results are referred to 6 h of pre-incubation time. Curcumin and photo-linker effect of the photo-responsive cross-linked trilayer on human skin melanoma cell line A375.S2 are promising. Indeed, first of all, for both 24 h or 72 h of culture conditions, we observe that a photo-responsive cross-linked trilayer no-loaded (blue lines in Figure 2.18 and 2.19) , also irradiated, does not show cytotoxicity. Therefore, in all the other cases, the observed cellular mortality is connected to the release of the drug while the nanocarriers is not toxic by itself. Furthermore, we could appreciate the photo-linker effect on curcumin action, observing

that the photo-responsive cross-linked trilayer when irradiated showed a cellular viability much lower than the same system (washed or not washed) but not photo-stimulated (violet curve in Figure 2.18 and 2.19). The only difference in the two cases was the absence or presence, respectively, of the UV irradiation. This is a nice demonstration of the goodness of our photo-responsive cross-linked trilayer.

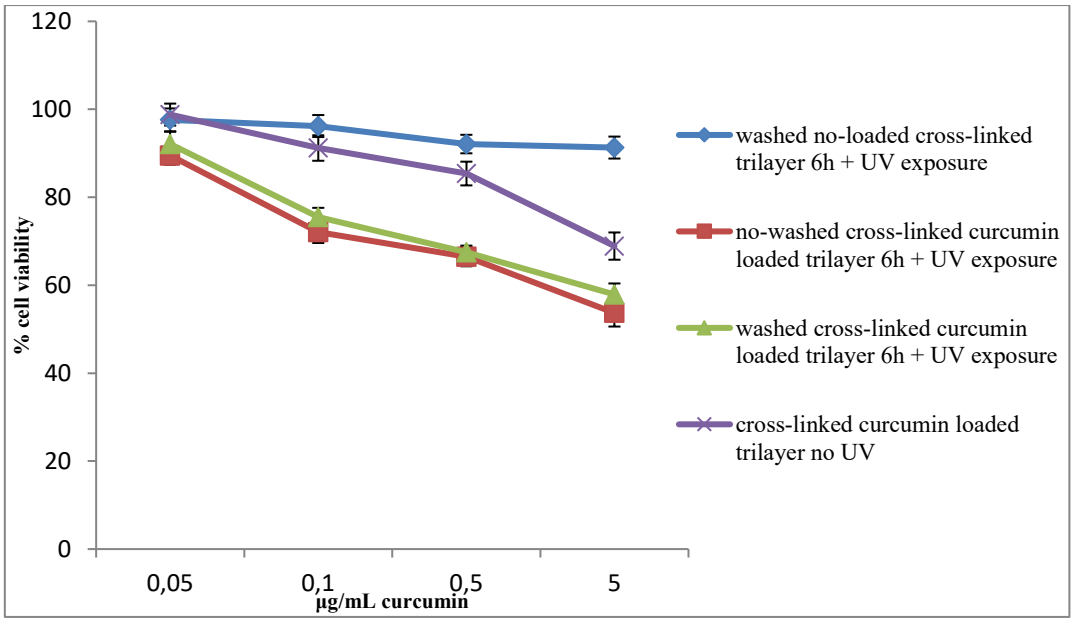

Figure 2.18. Viability of A375.S2 cell after 24h of exposure to 37°C as a function of curcumin concentration (µg/mL). Growth conditions: 24h.

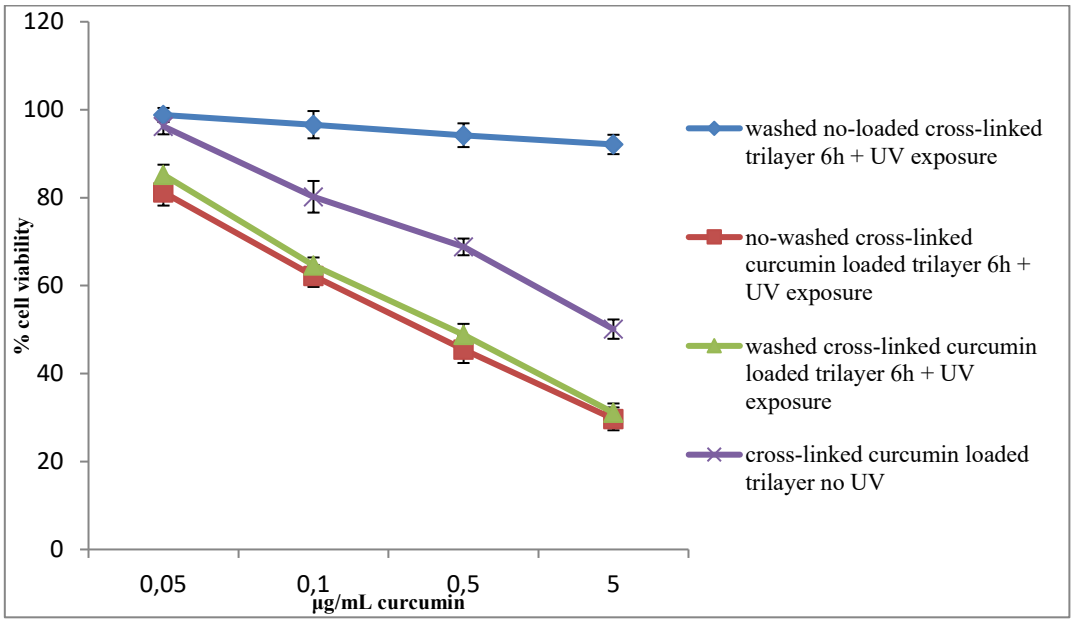

Figure 2.19. Viability of A375.S2 cell after 24h of exposure to 37°C as a function of curcumin concentration (µg/mL). Growth conditions: 72h.

2.4 Conclusions

In this work, we showed the preparation of a photo-responsive cross-linked LbL multilayer built on O/W nanoemulsion made of biocompatible materials. The introduction of a thiol functionalized *o*-nitrobenzyl group on glycol chitosan, opportunely characterized, allowed us to prepare a cross-linked trilayer using the alternated depositions of that polymer and allylated heparin *via* LbL technique and a photoinitiator free thiol-ene '*click'* reaction, obtaining stable nanocapsules in physiological conditions. On the other hand, the same thiol functionalized *o*-nitrobenzyl group allowed us to induce a controlled photo-cleavage of the nanocarrier at 365 nm, demonstrated by different characterization techniques. The goodness of our systems was also assessed by biological tests on melanoma cell models using curcumin as drug. Therefore, we provide a strategy to prepare biocompatible photo-responsive oil core based nanocapsules with possible use as controlled drug delivery systems. In particular, they may be used in the therapy of skin tumors or in the treatment of tumor tissues during surgery applications. Future *in vivo* studies could be another confirmation of the interesting applications of this new system.

2.5 References

1. Y. Yan, G. K. Such, A. P. R. Johnston, H. Lomas, and F. Caruso, *ACSNano*, **2011**, 5(6), 4252-4257.
2. A.P.R. Johnston et al., *Current Opinion in Colloid & Interface Science,* **2006**, 11, 203-209.
3. Y. Yan, M. Björnmalm, and F. Caruso, *Chem. Mater.,* **2014**, 26, 452−460.
4. E. Fleige et al., *Advanced Drug Delivery Reviews,* **2012**, 64, 866-884.
5. Pilar Rivera Gil et al., *Nanotoday,* **2008**, 3, 3-4.
6. R. Vecchione, U. Ciotola, A. Sagliano, P. Bianchini, A. Diaspro and P. A. Netti, *Nanoscale,* **2014**, 6, 9300-9307.
7. Vecchione et al., *Small,* **2016**, 22(12), 3005- 3016.
8. V. Calcagno, R. Vecchione, A. Sagliano, A. Carella, D. Guarnieri, V. Belli, L. Raiola, A. Roviello, P.A. Netti, *Colloids and Surfaces B: Biointerfaces,* **2016**, 142, 281-289.
9. Heng Pho Yap et al., *Adv. Mater.,* **2009**, 21, 4348-4352.
10. P.K. Deshmukh et al., *Journal of Controlled Release,* **2013**, 166, 294–306.
11. Younghyun Cho et al., *Soft Matter,* **2012**, 8, 10271-10278.
12. S. Ganta et al., *Journal of Controlled Release,* **2008**, 126, 187–204.
13. L.L. del Mercato et al., *Advances in Colloid and Interface Science,* **2014**, 207, 139–154.
14. D. Roy et al., *Progress in Polymer Science,* **2010**, 35, 278–301.
15. Q. Yi, G.B. Surkhorukov, *Advances in Colloid and Interface Science*, **2016**, 207, 57-63.
16. B. Yan, J. C. Boyer, D. Habault, N. R. Branda,, and Y. Zhao, *J. Am. Chem. Soc.,***2012**, 134, 16558−16561.
17. B. Yan, J. C. Boyer, N. R. Branda, and Y. Zhao*, J. Am. Chem. Soc.,* **2011**, 133, 19714–19717.
18. M. He, J. Li, S. Tan, R. Wang, and Y. Zhang, *J. Am. Chem. Soc.,* **2013**, 135, 18718−18721.
19. Avijit Jana et al., *J. Am. Chem. Soc.,* **2012**, 134, 7656−7659.
20. Tomatsu et al., *Advanced Drug Delivery Reviews*, **2011**, 63, 1257–1266.
21. V. Marturano et al., *Polymer,* **2015**, 70, 222-230.
22. S. Karthik et al., *Chem. Commun.,* **2013**, 49, 10471—10473.
23. P. Bawa, V. Pillay, Y. E Choonara and L. C du Toit, *Biomed. Mater.,* **2009**, 4.
24. Jyothi U. Menon et al., *Theranostics,* **2013**, 3(3).
25. Alina Y.Rwei et al., *Nano Today,* **2015**, 10, 451-467.
26. N. Fomina et al., *Advanced Drug Delivery Reviews,* **2012**, 64, 1005–1020.
27. T. Pauloehrl et al., *Angew. Chem. Int.,* **2012**, 51, 9181-9184.
28. Y. Zhao*, The Chemical Record,* **2007**, 7, 286-294.

29. E. Cabane, V. Malinova, S. Menon, C. G. Palivan and W. Meier, *Soft Matter,* **2011**, 7, 9167-9176.
30. Chiyoung Park et al., *Angew. Chem. Int.,* **2008**, 47, 2959 –2963.
31. Y. Li et al., *Journal of Polymer Science: Part A: Polymer Chemistry,* **2010**, 48, 551–557.
32. J. L. Vivero-Escoto, I. I. Slowing, C.-W. Wu, and V. S.-Y. Lin, *J. Am. Chem. Soc.,* **2009**, 131, 3462-3463.
33. C. A. DeForest and K. S. Anseth, *Angew. Chem. Int.*, **2012**, 51, 1816-1819.
34. I.-K. Park et al., *Polymer,* **2010**, 51, 3387-3393.
35. G.L. Ellman, *Arch. Biochem. Biophys*, **1958**, 74, 443–450.
36. P.W. Riddles, R.L. Blakeley, B. Zerner, *Anal. Biochem.,* **1979**, 94, 75–81.
37. P. Eyer, F. Worek, D. Kiderlen, G. Sinko, A. Stuglin, V. Simeon-Rudolf, E. Reiner, *Anal. Biochem.,* **2003**, 312, 224–227.
38. G. Papageorgiou, J. E. T. Corrie, *Tetrahedron*, **2007**, 63, 9668–9676.
39. Chapuis, Strazewski, *Tetrahedron,* **2006**, 62, 12108-12115.
40. Sean C. Warren et al., **2013**, Rapid Global Fitting of Large Fluorescence Lifetime Imaging Microscopy Datasets, PloS One, 8(8), e70687.
41. J. Hatami, S. G. Silva, M. B. Oliveira, R. R. Costa, R. L. Reis and J. F. Mano, *Polymers,* **2017**, 9, 440.
42. V. Quagliariello, R.V. Iaffaioli, E. Armenia, O. Clemente, M. Barbarisi, G. Nasti, M. Berretta, A. Ottaiano, A. Barbarisi, *J. Cell. Physiol*., **2017**, 232, 2063–2074.

Chapter 3

Cardioprotective Effects of Nanoemulsions Loaded with Anti-Inflammatory Nutraceuticals against Doxorubicin-Induced Cardiotoxicity

This work has been published: Vincenzo Quagliariello, Raffaele Vecchione, Carmela Coppola, Chiara Di Cicco, Alberta De Capua, Giovanna Piscopo, Rolando Paciello, Viviana Narciso, Carmen Formisano, Orazio Taglialatela-Scafati, Rosario Vincenzo Iaffaioli, Gerardo Botti, Paolo Antonio Netti and Nicola Maurea, Cardioprotective Effects of Nanoemulsions Loaded with Anti-Inflammatory Nutraceuticals against Doxorubicin-Induced Cardiotoxicity. *Nutrients*, 2018, 10, 1304

Abstract

Doxorubicin is a highly active antineoplastic agent, but its clinical use is limited because of its cardiotoxicity. Although nutraceuticals endowed with anti-inflammatory properties exert cardioprotective activity, their bioavailability and stability are inconsistent. In an attempt to address this issue, we evaluated whether bioavailable nanoemulsions loaded with nutraceuticals (curcumin and fresh and dry tomato extracts rich in lycopene) protect cardiomyoblasts (H9C2 cells) from doxorubicin-induced toxicity. Nanoemulsions were produced with a high-pressure homogenizer. H9C2 cells were incubated with nanoemulsions loaded with different nutraceuticals alone or in combination with doxorubicin. Cell viability was evaluated with a modified MTT method. The levels of the lipid peroxidation products malondialdehyde (MDA) and 4-hydroxy-2-butanone (4-HNA), and of the cardiotoxic-related interleukins IL-6, IL-8, IL-1β and IL-10, tumor necrosis factor-alpha (TNF-α), and nitric oxide were analyzed in cardiomyoblasts. The hydrodynamic size of nanoemulsions was around 100 nm. Cell viability enhancement was 35–40% higher in cardiomyoblasts treated with nanoemulsion + doxorubicin than in cardiomyoblasts treated with doxorubicin alone. Nanoemulsions also protected against oxidative stress as witnessed by a reduction of MDA and 4-HNA. Notably, nanoemulsions inhibited the release of IL-6, IL-8, IL-1β, TNF-α and nitric oxide by around 35–40% and increased IL-10 production by 25–27% versus cells not treated with emulsions. Of the nutraceuticals evaluated, lycopene-rich nanoemulsions had the best cardioprotective profile. In conclusion, nanoemulsions loaded with the nutraceuticals described herein protect against cardiotoxicity, by reducing inflammation and lipid oxidative stress. These results set the stage for studies in preclinical models.

3.1 Introduction

Doxorubicin is a cytotoxic antibiotic that is used to treat leukemia and lymphoma, as well as breast, lung, and other solid tumors. However, its clinical use is limited because of its irreversible cardiotoxicity that can lead to heart failure in a dose-dependent manner.[1-3] The mechanism of doxorubicin-induced cardiotoxicity is based on the generation of free radicals and reactive oxygen species that attach to membrane lipids and proteins thereby generating toxic products.[4,5] Doxorubicin stimulates overproduction of reactive oxygen species and impairs cardiac cell function.[2] It induces cardiotoxicity also by producing the pro-inflammatory interleukins IL-8 and IL-6.[6] Natural products endowed with antioxidant activity, namely, survivin, sesamol and herbaleonurin, decrease or prevent doxorubicin-induced damage.[7] The natural antioxidants vitamin E and catalase, and the synthetic antioxidants 3-methyl-1-phenyl-2-pyrazolin-5-one (edaravone) are used to treat cardiac hypertrophy. The mechanism of action of nutraceuticals is based on the reduction of oxidative stress,

cardiovascular risk factors such as Metabolic Syndrome[8,9] but their therapeutic potential in cardiology remains unknown.[10,11] Lycopene is a potent dietary carotenoid antioxidant thanks to its many conjugated double bonds[12] and it has the strongest singlet oxygen-quenching ability of all dietary carotenoids.[13] The relationship between lycopene and cardiovascular disease has been examined in several epidemiological studies.[5] The few studies conducted so far regarding the effect of lycopene or tomato extract on doxorubicin-induced cardiotoxicity showed some protective effects, but more studies are needed to evaluate their potential as cardioprotectors under doxorubicin treatment.[14] Curcumin is the main active ingredient of the turmeric spice Curcuma longa; it has several pharmacological and biological properties being an antioxidant, anticancer, anti-inflammatory and antiviral agent.[12] Curcumin induces apoptosis, via deactivation of NF-kB and its regulated gene products, and it also suppresses inflammatory cytokines such as interleukins (IL-1, -1β, -6, and -8), TNF-α, and COX-2.[15] In studies comparing free and nano encapsulated curcumin, the bioavailability and effect of curcumin were greatly increased in terms of anti-inflammatory action.[16,17] The mechanism of action of these nutraceuticals are based on cell cycle regulation, tyrosine kinase modulation[18] inhibition of cytokine and interleukin secretion, and AMPK-Sclerosis Tuberous Complex (TSC) activation with consequent AKT-mTOR axis inhibition.[19] However, the clinical use of these nutraceuticals is limited by their low oral bioavailability due to oxidation in biological environments, which results in a low accumulation in the cell cytoplasm.[20] Given these limitations, the aim of this study was to encapsulate such nutraceuticals in nanocarriers able to protect them from oxidative and enzymatic environmentsin order to achieve a more specific and controlled release. We also investigated the pathways involved in cardioprotection by analyzing the anti-inflammatory and anti-oxidant effects of the nanocarriers based on IL-1β, IL-8, IL-6 and malondialdehyde (MDA)/4-HNA cellular secretion under pro-inflammatory conditions.

The proposed strategy of cardioprotection could be of translational importance in cardioncology considering the crucial role of the heart and vascular microenvironments in the etiology of cardiotoxicity.

3.2 Materials and Methods

Synthesis and Characterization of Nanoemulsions. Materials: Both soybean oil (density at 20 °C of 0.922 g mL^{-1}) and surfactant Lipoid E80 (egg lecithin powder 80–85% enriched with phosphatidyl choline (PC) and 7–9.5% content in phosphatidylethanolamine (PE)) were purchased from Lipoid GmbH and used without further purification. Millipore Milli-Q water was used for the preparation of all nanoemulsions and solutions. Chitosan (CT, LMW 90–150 kDa, DDA 75–85%) was purchased from Sigma Aldrich (Milan, Italy). Chitosan was soluble in acidic conditions due to the protonation

of its amine moieties[21] and was used without further purification; Fluorescein isothiocyanate (FITC, M.W. = 389.38 g mol^{-1}) was also purchased from Sigma Aldrich and used without further purification. Curcumin (from *Curcuma longa* Turmeric, powder, M.W. = 368.38 g mol^{-1}) was again purchased from Sigma-Aldrich and used with no further purification.

Preparation of Nanoemulsions.

Nanoemulsions were prepared following a previously developed protocol[22] which can also be adapted to the encapsulation of contrasting agents.[23] Briefly, first the oil phase was prepared by adding the surfactant to the soybean oil and mixed at 60 °C under gentle stirring. Then, the oil phase was added drop wise to the water phase (Milli-Q water) and mixed using the immersion sonicator (Ultrasonic Processor VCX500 Sonic and Materials) until there was a suitable dissolution. The pre-emulsions were finally passed at 2000 bar through the high-pressure valve homogenizer (Microfluidics M110PS) for the first three individual cycles to greatly reduce the initial size, then the reservoir was continuously refilled for 200 steps. This method was used for the preparation of all oil-in-water nanoemulsions at 20 wt% of oil concentration. In particular, 5.8 g of surfactant were dissolved in 24 mL of oil. In the case of curcumin, 100 mg of drug were added to 24 mL of the oil phase dissolving the surfactant, and mixing at 60 °C under gentle stirring. Instead, in the case of tomato peel extracts, 5.8 g of surfactant were dissolved in 24 mL of oil already containing the biomolecule always mixing at 60 °C under gentle stirring. In fact, in the case of tomato peel extracts, in one option, ~800 g of fresh tomato peels were processed overnight with ~1.5 L of soy-bean oil in the Naviglio extractor which is a type of solid-liquid extractor.[24] This method has already been used to extract pure lycopene by using an alcoholic extraction.[25] In this case, for the first time we extracted the bioactive compounds from the tomato peels by using a vegetable oil as solvent that is then used for the preparation of the nanoemulsion. In a second option, the same amount of fresh tomato peels was first lyophilized and then processed by using the same procedure as for the fresh tomato peels. Fluorescent nanoemulsions were obtained by mixing 4 mL of ethanol solution of FITC (0.75 mg/mL) to the soybean oil during the emulsion preparation and drying the ethanol from the mixture with mild heating. The final concentration of FITC in the 10 wt% emulsion is 125 μg/mL. Then, 0.1 M acetic acid solution of chitosan (0.125 wt%) was prepared. Each nanoemulsion (freshTom-Ne, dryTom-Ne, curc-Ne and FITC-Ne) 20 wt% oil was added to the chitosan solution quickly under vigorous stirring and kept under stirring for 15 min to allow uniform chitosan deposition. Final concentrations of oil and chitosan were 10 and 0.1 wt%, respectively, while the pH of the final secondary nanoemulsions was 4. These nanoemulsions were re-dispersed using the method reported previously[26] and stored at room temperature. The nutraceutical-loaded nanoemulsions tested in this study are listed in Table 3.1.

Table 3.1. The nutraceutical-loaded and fluorescent nanoemulsions

Nanoemulsions and Nutraceuticals Loaded	Acronym
Uncoated nanoemulsion loaded with fresh tomato extract	freshTom-Ne
Chitosan-coated nanoemulsion loaded with fresh tomato extract	freshTom Ne-CT
Uncoated nanoemulsion loaded with dry tomato extract	dryTom-Ne
Chitosan-coated nanoemulsion loaded with dry tomato extract	dryTom-Ne-CT
Uncoated nanoemulsion loaded with curcumin	curc-Ne
Chitosan-coated nanoemulsion loaded with curcumin	curc-Ne -CT
Uncoated fluorescent nanoemulsion loaded with FITC	FITC-Ne
Chitosan-coated fluorescent nanoemulsion loaded with FITC	FITC-Ne-CT

LC/MS Analysis for Lycopene Measurement.

HPLC-grade acetonitrile, methanol, dichloromethane, n-hexane and lycopene analytical standard were purchased from Sigma (St. Louis, MO, USA). The assay was performed according to the procedure described by Kozukue and Friedman (2003) slightly modified.[27] HPLC analysis was performed on a Jasco Extrema LC-4000 system (Jasco Inc., Easton, MD, USA) equipped with photo diode-array detector and autosampler. Data were acquired and analyses were performed using JASCO ChromNAV (version 2.02.04). Samples were analyzed on a Gemini C18 column (250 x 4.6 mm, 5 µm, Phenomenex) and lycopene was detected at 450 nm. The column was eluted at a flow rate of 1mL/min with a two-solvent system, namely, (A) acetonitrile, (B) n-hexane/dichloromethane/methanol (1:1:1) with 82–76% A for the first 10 min, then in 2 min 58% A, in 6 min 40% A, and finally returned to 82% A in 5 min. This was followed by isocratic elution for 2 min. Calibration curve was performed with lycopene samples prepared freshly on a daily basis. The retention time of lycopene was 15 min. Each analysis was performed in triplicate. Lycopene standard was diluted to obtain the following ppm concentrations: 1, 5, 25, 50 and 100. A good linear fit range was found, the regression equation and correlation coefficient were respectively: $y = 11660x + 776.75$, $R = 0.9998$.

Cell Viability.

To evaluate the cardioprotective effects of nutraceutical-loaded nanoemulsions on H9c2 cardiomyoblasts (American Type Culture Collection, Manassas, VA, USA), we measured the mitochondrial dehydrogenase activity of these cells using a modified MTT [3-(4,5-dimethyldiazol-2-yl)-2,5-diphenyltetrazoliumbromide] procedure according to the manufacturer's instructions (Dojindo Molecular Technologies Inc., Rockville, MD, USA). H9c2 cells were grown in Dulbecco's modified Eagle's medium (DMEM) with 10% (v/v) heat inactivated fetal bovine serum, penicillin G

(100 U/mL), and streptomycin (100 mg/mL) in 96-well plates at a density of 10,000 cells per well at 37 °C in a humidified 5% CO_2 atmosphere. After 24 h of growth, we divided cells into the following groups: doxorubicin at 20 μM; nutraceutical-loaded nanoemulsions in the uncoated form: dryTom-Ne, freshTom-Ne, curc-Ne and in the chitosan-coated formulations, designated dryTom-Ne-CT, freshTom-Ne-CT, curc-Ne-CT (all at concentrations ranging from 0.5 to 5% w/v of oil) all tested in combination with 20 μM doxorubicin. We decided to use only this Doxorubicin concentration referring to several works, related to cardioprotection, in the literature.[2,3] Moreover, we tested and compared the effects of Enalapril, a common inhibitor of angiotensin-converting enzyme at 10, 25 and 50 μM as reported elsewhere[28] and Carvedilol at 1, 5 and 10 μM[29] both co-incubated with 20 μM doxorubicin. Carvedilol is a nonselective beta blocker/alpha-1 blocker used to treat mild-to-severe congestive heart failure and left ventricular dysfunction after a heart attack. In all experiments, cells were incubated for 24 h under standard conditions. Cells were then washed three times with PBS at pH 7.4 and incubated with 100 μL of an MTT solution (0.5 mg/mL in cell culture medium) for 4 h at 37 °C. Absorbance readings were acquired at a wavelength of 450 nm with the Tecan Infinite M200 plate-reader (Tecan Life Sciences Home, Männedorf, Switzerland) using I-control software. Relative cell viability (%) was calculated with the following formula $[A]_{test}/[A]_{control}$ x 100, where "$[A]_{test}$" is the absorbance of the test sample, and "$[A]_{control}$" is the absorbance of the control cells incubated solely in culture medium. After the evaluation of cell cytotoxicity, we measured the total protein content using the Pierce Micro BCA protein assay kit (Thermo Fisher, Milan, Italy). Briefly, the cells were washed with ice-cold PBS, and incubated for 15 min in 150 μL cell lysis buffer (0.5% v/v Triton X-100 in PBS) that included 150 μL of the Micro BCA protein assay kit reagent (prepared according to the manufacturer's instructions). Absorbance at 562 nm was measured on a plate reader. Cytotoxicity measurements were normalized by the amount of total protein content in each well.

Cellular Uptake Studies.

Uptake Quantification. H9c2 cardiomyoblasts were grown in DMEM with 10% (v/v) heat inactivated FBS, penicillin G (100 U/mL), and streptomycin (100 mg/mL) at 37 °C in a humidified 5% CO_2 atmosphere. For uptake experiments, 5 x 103 cells/well were seeded in a 24-well plate and allowed to grow for 24 h. The medium was then replaced with 0.1 mL of a 0.5% oil solution of fluorescent uncoated and chitosan-coated nanoemulsions in culture medium and incubated for between 0.5 and 24 h. Cells were then washed twice with PBS (pH 7.4) and after specified time intervals, the experiments were terminated by removing the supernatant, washing the cells three times with 10 mM PBS and lysing the cells with 0.1 mL of 0.5% Triton X-100 in 0.2 N NaOH. The membrane-bound and internalized fluorescent nanoemulsions were quantified by analyzing the fluorescence of the cell

lysate (λ_{exc} = 485 nm, λ_{em} = 535 nm), using a calibration curve with 0.001 up 5% oil of fluorescent nanoemulsions dispersed in a cell lysate solution (10^6 untreated cells dissolved in 1 mL of the Triton X-100/0.2 N NaOH solution).

Mechanistic Studies. To determine the mechanism underlying nanoemulsion internalization in H9c2 cells, we investigated the effects of following treatment: bafilomycin A1 (that inhibits endosomal acidification by inhibiting membrane ATPases, that also affects the budding of endosomal carrier vesicles from early endosomes, filipin (an inhibitor of caveolae-mediated endocytosis), nocodazol (that inhibits membrane ruffling and active [vesicular] transport by disrupting cytoplasmic microtubules), cytochalasin D (a well-known inhibitor of membrane ruffling and active [vesicular] transport that acts by disrupting actin fibers), hypertonic sucrose and potassium-free buffer (that inhibit the clathrin-mediated uptake with lower and higher selectivity, respectively), and sodium azide (that reduces active transport by inhibiting cellular respiration).In the case of fluorescent nanoemulsions, cellular uptake experiments were conducted after 4 h of incubation in the presence of these inhibitors, specifically: 0.45 M sucrose, 0.1mg/mL cytochalasin D, 1 mg /mL nocodazole, 0.1 mg/mL filipin and 2 x 10^{-7} M bafilomycin A1. In separate experiments, cancer cells were preincubated with 10^{-2} M of the metabolic inhibitor sodium azide for 30 min before the uptake of uncoated and chitosan-coated nanoemulsions and during uptake to evaluate the energy dependence of the process. With the exception of sodium azide and sucrose, which were dissolved directly in the culture medium, stock solutions of the other effectors were prepared in DMSO then diluted with culture medium to the proper concentration. H9c2cells were pre-incubated at 4 °C for 30 min with inhibitors then at 37 °C for 4 h as reported elsewhere.[30] Instead, to study the effect of intracellular potassium depletion, cardiomyocytes were rinsed twice and incubated with a potassium-free buffer solution with the following substances: 0.14 M NaCl, 0.02 M of MES buffer, 10^{-3} M of $CaCl_2$ and 1 mg/mL of glucose pH 7.4 for 30 min before uptake experiments were performed in the same medium, as reported in literature.[31]

Cellular Antioxidant Activity Following Oxygen Radical Generator Exposure. Cellular uptake of nanoemulsionsin H9c2 cells after oxygen radical generator exposure was measured as reported elsewhere.[32] In brief, H9c2cellswere incubated with 50 µL of 2,2'-Azobis(2-methylpropionamidine) dihydrochloride (AAPH) 4 µM for 10 min to simulate oxidative stress. Cells were then washed three times with PBS and then treated with nutraceutical-loaded nanoemulsions at oil concentrations ranging from 0.5 to 5% w/v of oil for 10, 20, 45, or 60 min. Gallic Acid (at 25, 50 and 100 µM), a common antioxidant, was used as positive control. Subsequently, samples were washed twice and

sonicated at 10% amplitude with energy of 20 W/cm^2 for 5 min to lyse cardiomyoblasts by sonicator (Sonics, Vibra Cell, Newtown, CT, USA). After sonication, samples were centrifuged for 30 min at 2700x g. The supernantant was then removed as the lysate fraction. Three different plates per compound were run for lysate fractions.

Detection of Intracellular Reactive Oxygen Species. The formation of intracellular reactive oxygen species was evaluated using a conventional fluorescent probe, called DCFH-DA, as described elsewhere.33 Briefly, H9c2 cells were grown in DMEM with 10% (v/v) heat-inactivated FBS, penicillin G (100 U/mL) and streptomycin (100 mg/mL) at 37 °C in a humidified 5% CO_2 atmosphere. Subsequently, 5 x 10^3 cells/well were seeded in a 24-well plate and allowed to grow for 24 h. After washing twice with PBS, cells were pretreated or not with all nutraceutical-loaded nanoemulsions at oil concentrations ranging from 0.5 to 5% w/v of oil for 4 h; pretreatment also with gallic acid (at 25, 50 and 100 μM) was used as positive control. After pretreatments, cells were then incubated with 5 μM DCFH-DA in PBS for 30 min. After the DCFH-DA removal, cells were stimulated with 40 ng/mL of lipopolysaccharide (LPS) or doxorubicin at 50 nM for 12 h. Cell fluorescence was measured using a microplate spectrofluorometer (xMark Microplate, Spectrofluorometer Biorad, Milan, Italy). Intracellular antioxidant activity was expressed as percentage of control cells.

Lipid Peroxidation Studies. To study the protective effects of nutraceutical-loaded nanoemulsions at the membrane level of cardiomyoblasts, H9c2 cells were grown in DMEM with 10% (v/v) heat inactivated FBS, penicillin G (100 U/mL), and streptomycin (100 mg/mL) at 37 °C in a humidified 5% CO_2 atmosphere. Subsequently, 5 x 10^3 cells/well were seeded in a 24-well plate and allowed to grow for 24 h. Briefly, H9c2 cells were treated with doxorubicin (50 nM) or LPS (40 ng/mL) for 6 h or pretreated for 4 h with all nutraceutical-loaded nanoemulsions at oil concentrations ranging from 0.5 to 5% w/v or with gallic acid (at 25, 50 and 100 μM) as positive control. Then, cells from each group were washed three times with cold PBS, harvested with 0.25% trypsin, and centrifuged at 1000x g for 10 min. The supernatant was discarded and the cell pellet sonicated in cold PBS. After centrifugation (800x g, 5 min), the supernatant was immediately evaluated for MDA and 4-HNAcommercial kits with a spectrophotometer according to the manufacturer's protocols (Sigma Aldrich, Milan, Italy). We measured the protein content of the cell homogenates using the Micro BCA protein assay kit (Pierce, Thermo Fisher, Milan, Italy) according to kit instructions.

Measurement of Nitric Oxide. To evaluate the effects of nutraceutical-loaded nanoemulsions on the release of nitric oxide from H9c2 cells we analyzed the release of nitrite, a stable product of nitric

oxide in aqueous medium, using the Griess Reagent System (Promega, Madison, WI, USA) as described elsewhere.[18] Briefly, H9c2 cardiomyoblasts were grown in DMEM with 10% (v/v) heat inactivated FBS, penicillin G (100 U/mL), and streptomycin (100 mg/mL) at 37 °C in a humidified 5% CO_2 atmosphere. Subsequently, 5 x 10^3 cells/well were seeded in a 24-well plate and allowed to grow for 24 h. Cells were treated with doxorubicin (50 nM) or LPS (40 ng/mL) for 6h or pretreated for 4 h with all nutraceutical-loaded nanoemulsions at oil concentrations ranging from 0.5 to 5% w/v. Also, in this case, pre-incubation with gallic acid (at 25, 50 and 100 μM), a common antioxidant, was used as positive control. The culture medium was then mixed with an equal volume of sulfanilamide solution (1% v/v in 5% v/v phosphoric acid) and of N-1-naphtylethylenediamine dihydrochloride solution (0.1% v/v in water). Absorbance was measured at 540 nm with a spectrophotometer (xMark Microplate, Spectrofluorometer Biorad, Milan, Italy). Nitrite concentrations were determined from a calibration curve of standard 0.1 M sodium nitrite concentrations from 0.5 to 50 μM against absorbance.

Intracellular Calcium Level. Doxorubicin-induced cardiotoxicity is also accompanied by an increase in intracellular calcium levels. Dysregulation of intracellular calcium concentrations is both a result and a cause of the generation of radical oxygen species. Doxorubicin induces the release of calcium from the sarcoplasmic reticulum by increasing the probability that the channel adopts the open state. An increase in intracellular calcium is not the only cause of mitochondrial calcium dysregulation, in fact, doxorubicin affects mitochondrial calcium transport thereby contributing to the increase in intracellular calcium levels. To monitor the intracellular calcium in H9c2 cardiomyoblasts, we used the fluorescence dye Fluo-3 AM, following the manufacturer's protocol. Briefly, H9c2 cells were treated with doxorubicin (50 nM) or LPS (40 ng/mL) for 6h or pretreated for 4h with each of the nutraceutical-loaded nanoemulsions at oil concentrations ranging from 0.5 to 5% w/v. After incubation, H9c2 cardiomyoblasts were loaded with 5 μM Fluo-3 AM at 37 °C for 30 min in the dark, and then washed three times with PBS to remove excess dye. The fluorescence intensity of Fluo-3 chelated with calcium was recorded on a microplate spectrofluorometer (xMark Microplate, Spectrofluorometer Biorad, Milan, Italy) at excitation and emission wavelengths of 488 and 525 nm, respectively.

Anti-Inflammatory Studies. The expression of IL-6, IL-8, IL-1β, IL-10, and tumor necrosis factor-alpha (TNF-α) in cardiomyoblasts was evaluated with ELISA, as described elsewhere.[34] Briefly, H9c2 cells were grown in DMEM with 10% (v/v) heat inactivated FBS, penicillin G (100 U/mL), and streptomycin (100 mg/mL) at 37 °C in a humidified 5% CO_2 atmosphere. After incubation for

24h and starvation in serum-free medium for 2.5 h, cardiomyoblasts were treated or not with the nutraceutical-loaded nanoemulsions at oil concentrations ranging from 0.5 to 5% w/v for 4h before exposure to LPS (40 ng/mL) for 12 h to stimulate inflammation. Subsequently, culture supernatants were collected, centrifuged to pellet any detached cells, and measured using TNF-α, IL-1β, IL-6, IL-8 and IL-10 ELISA kits according to the manufacturer's instructions (Sigma Aldrich, Milan, Italy). The sensitivity of this method was below 10 (pg/mL), and the assay accurately detected cytokines in the range of 1–32,000 pg/mL.

Statistical Analysis. Differences between the experimental groups were identified with a one-way analysis of variance and subsequently with Turkey's multiple comparison test in Sigma Plot Software (Sigma, San Jose, CA, USA). $p < 0.05$ was the lowest acceptable threshold for significance.

3.3 Results.

Synthesis and Chemical-Physical Characterization of Nutraceutical-Loaded Nanocarriers.

Oil in water nanoemulsions in their uncoated and chitosan-coated form were produced as previously described.[23] In particular, among different possible sizes of the nanoemulsions that can be tuned with the amount of surfactant, namely egg lecithin, we chose to work with the smallest possible. Indeed, we have already demonstrated the importance of scaling down the size in terms of bioavailability once in vivo. Regarding curcumin, we reproduced the uncoated and chitosan-coated oil in water nanoemulsion that we previously used to evaluate their cardio-protective properties.[16] Then, given the well-known cardio-protective properties of lycopene, we started from tomato peel that is notoriously rich in lycopene and we applied the Naviglio solid-liquid extraction method by directly immersing tomato peel in the oil phase. After enriching the oil with the active principles contained in tomato peel, we used it to prepare the uncoated and chitosan-coated form of the oil in water nanoemulsion by applying the same procedure described above. In one extraction procedure, we used wet tomato peels directly as obtained from a tomato company (Pietro Grimaldisrl, Sant'Egidio del Monte Albino SA, Italy), and in another we lyophilized the tomato peels before extraction. In the latter case, we used an amount of peel corresponding to the starting amount of wet tomato peels. For the overall uptake study, we also used oil in water nanoemulsions again uncoated and coated with chitosan by repeating the procedure previously reported. Together with the nutraceutical encapsulating nanoemulsions we also used an FITC-loaded nanoemulsion for uptake studies. The dimensional characterization of the nanocarriers used in this study is reported in Table 3.2, together with the z-pot of the all systems. Thanks to the surface charge and to the narrow size distribution, the systems are stable for several months especially in the coated forms, as reported elsewhere.[21,26] As an

example, the uncoated and coated nanoemulsions richest in lycopene were characterized by cryo-TEM as reported in Figure 3.1. It is clear from the morphological analysis the level of monodispersion of the uncoated and coated carrier and the sizes are in agreement with the DLS analysis.

Table 3.2. Physical–chemical characteristics of nanocarriers used in this study: hydrodynamic size, polydispersity index and z-potential.

Nanoemulsions	Mean Hydrodynamic Size (nm)	PDI	ζ-Potential (mV)
Uncoated nanoemulsion loaded with fresh tomato extract	97.09 (0.59)	0.098 (0.011)	−22.9 (1.3)
Chitosan-coated nanoemulsion loaded with fresh tomato extract	139.6 (0.85)	0.076 (0.004)	49.6 (0.5)
Uncoated nanoemulsion loaded with dry tomato extract	93.23 (0.66)	0.122 (0.020)	−23.0 (0.9)
Chitosan-coated nanoemulsion loaded with dry tomato extract	128.8 (1.01)	0.056 (0.007)	46.1 (0.5)
Uncoated nanoemulsion loaded with curcumin	105.4 (2.83)	0.118 (0.049)	−22.0 (5.6)
Chitosan-coated nanoemulsion loaded with curcumin	119.8 (0.80)	0.079 (0.010)	44.3 (1.7)
Uncoated fluorescent nanoemulsion loaded with FITC	93.83 (0.86)	0.090 (0.016)	−30.5 (1.5)
Chitosan-coated fluorescent nanoemulsion loaded with FITC	94.50 (0.75)	0.075 (0.010)	23.7 (0.2)

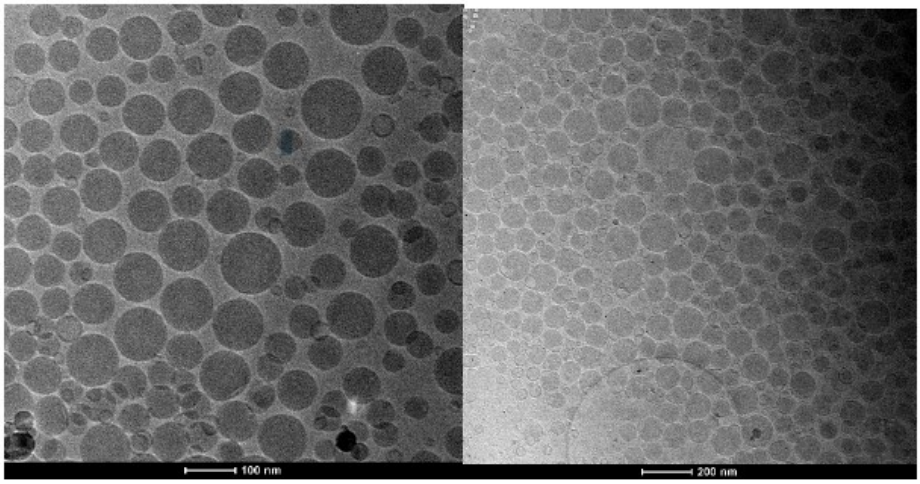

Figure 3.1. Cryo-TEM projection images of dryTom-Ne (left) and dryTom-Ne-CT (right).

Measurement of Lycopene Content in Tomato Peel Extracts.

The amount of lycopene in the two samples was measured using a previously reported LC/MS method slightly modified.[25] Quantitative measurements were obtained on the basis of a calibration curve established with commercial lycopene standard samples as reported in the materials and methods section. The lycopene content was significantly lower in “fresh tomato extract” than in “dry tomato extract” (0.007 mg/mL ± 0.0005, versus 0.029 mg/mL ± 0.001). A representative chromatogram of the two samples is depicted in Figure 3.2. This is due to the fact that the presence of water in fresh products makes the extraction of lipophilic compounds more difficult using this method. Based on this information, for all subsequent studies, it is important to specify that the nanoemulsions are based

on fresh tomato extract at 0.5%, 1% and 5% of oil contain, respectively, 0.035, 0.07 and 0.35 μg of lycopene/mL of solution. Moreover, nanoemulsions must be based on dry tomato extract at 0.5%, 1% and 5% of oil contain, respectively, 0.145, 0.29 and 1.45 μg of lycopene/mL of solution.

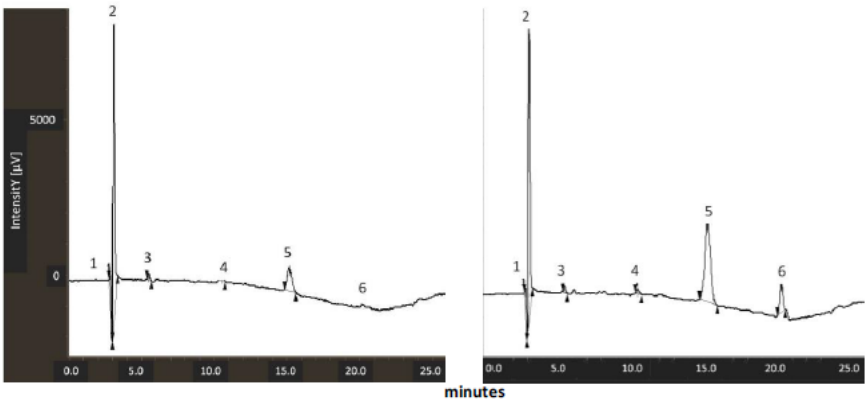

Figure 3.2. Representative chromatograms for the samples "dry tomato extract" (left) and "fresh tomato extract" (right). Lycopene is peak n. 5.

Cell Viability.

As shown in Figure 3, doxorubicin treatment for 24 h decreased cardiomyoblasts viability by more than 80% but co-incubated with all the nanoemulsions used resulted in concentration-dependent cardioprotective effects. Chitosan-coated forms of nanoemulsions had the best cardioprotective properties, probably due to a better cellular uptake on cardiomyoblasts (Figure 3.3A). Overall cell viability was 5-20% higher in cells treated with chitosan-coated nanoemulsions than in unpretreated cells. Moreover, lycopene-rich nanoemulsions (dry-Tom-Ne) had better cardioprotective properties than did fresh-Tom-Ne-treated and curc-Ne-treated cardiomyoblasts. In fact, the viability of cardiomyoblasts treated with uncoated and chitosan-coated dryTom-Ne at 5% oil was about 45% and 60% higher, respectively versus doxorubicin-treated cells. To determine the translational potential of these nanoemulsions in cardioprotection during doxorubicin treatment, we compared the effects of Enalapril and Carvedilol (Figure 3.3B–D) as common drugs used in cardio-oncology; interestingly, the best nanoemulsion formulation at the higher concentration tested seems to be 30% and 35% more effective, compared to Enalapril and Carvedilol at very high concentration such as 50 and 100 μM respectively ($p < 0.001$ for both).

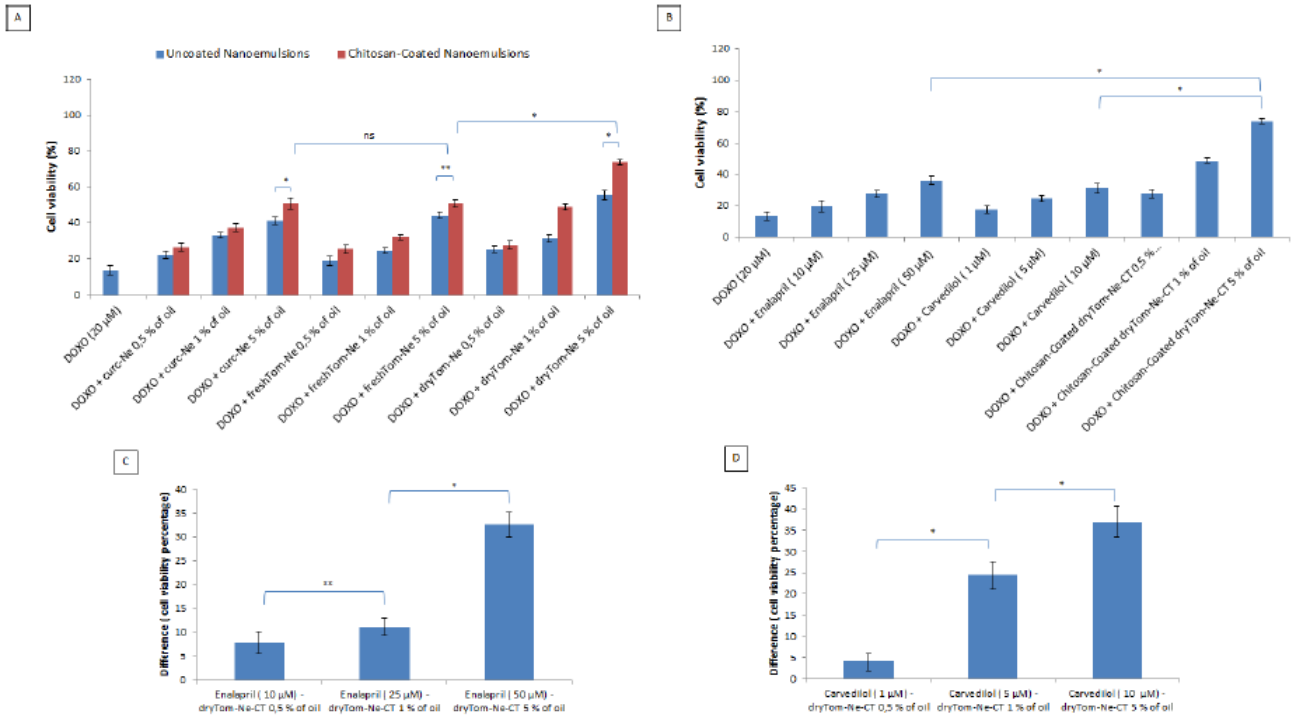

Figure 3.3. Cell viability in function of the concentration of nutraceutical-loaded uncoated and chitosan-coated nanoemulsions all tested at concentrations from 0.5 to 5% v/v of oil tested combined with doxorubicin at 20 µM. (**A**). The viability of cardiomyoblasts incubated with doxorubicin (at 20 µM) in association with Enalapril at 10, 25 and 50 µM and Carvedilol at 1, 5 and 10 µM. (**B**). Difference in the percentage of cell viability versus control, between (**C**) Enalapril and (**D**) Carvedilol and the best nanoemulsion (dryTom-Ne-CT) at different concentrations * $p < 0.001$; ** $p < 0.05$; ns: not significant.

Uptake Quantification and Mechanistic Studies.

As we previously reported,[18] the cellular uptake of fluorescent nanocarriers is time-dependent. In the present study, after 2 h of incubation, approximately 30–35% of chitosan-coated nanoemulsions were internalized or adhered to the membrane of H9c2 cells (Figure 3.4). The uptake of uncoated nanoemulsions at 24 h of incubation was invariably less than 30–35% that of chitosan-coated emulsion, which corroborates the effects on cell viability described previously. After 24 h of incubation, around 90% of chitosan-coated nanoemulsions were internalized in cardiomyoblasts (Figure 3.4). Having established that nanocarriers are able to internalize in H9c2 cells, we complemented this study by analyzing the mechanism of cell uptake using a small library of inhibitors of general active transport processes, endosomal acidification, caveolae-mediated endocytosis, membrane ruffling and vesicular transport microtubules and actin fibers.[35] Thus, we evaluated the effects of these inhibitors on the internalization of fluorescent nanocarriers in cells. As shown in Figure 3.4, the nanocarriers were highly sensitive to all these factors. In detail, sodium azide inhibited endocytosis by 55–60% and cytochalasin by 35–40%. Nocodazole did not have any significant effect on H9c2, which is in line with the energy-dependent nature of the nanocarrier internalization and the

involvement of stress fibers, but not of microtubules. Filipin did not significantly inhibit cellular internalization thereby excluding a caveolae-mediated endocytic mechanism of nanoemulsions uptake. Bafilomycin A1 significantly reduced endocytosis by 50%. Although hypertonic sucrose is known to inhibit also macropinocytic and caveolar uptake, the more clathrin-selective potassium-free buffer had the same inhibitory effect, indicating the clathrin-dependent endocytosis is the most likely internalization mechanism.[36] It seems that uncoated and chitosan-coated nanoemulsions have the same mechanism of endocytosis, however, chitosan-coated nanoemulsions are clearly more sensitive to the inhibitors than uncoated nanoemulsions, which indicates a clathrin-dependent endocytosis.

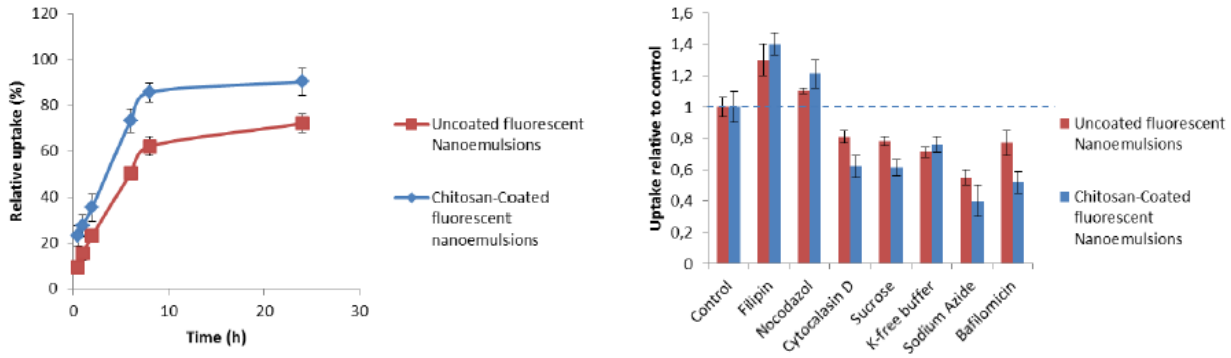

Figure 3.4. Left, overall cellular uptake quantification of H9c2 cells (at a density of 5 x 10^3 cells/well) from 0.5 up to 24 h of contact with fluorescent nanocarriers at 1% v/v oil. Right, effect of different inhibitors on the internalization of fluorescent nanocarriers (1% v/v oil) in H9c2 cells after 4 h of incubation. The data are normalized against their controls.

Cellular Antioxidant Activity after Oxygen Radical Generator Exposure.

As shown in Figure 3.5A, the mean antioxidant capacity differed significantly between the lysates of cells treated with chitosan-coated nanocarrier sand those of uncoated nanocarriers. Specifically, treatment of H9c2 cells with dryTom-Ne exerted antioxidant activity in a concentration-dependent manner with a mean of 12,323 (±998), 20,233 (±956), 30,122 (±1023) TE/L/10 cells for 0.5%, 1% and 5% of oil, respectively. The chitosan-coated emulsion had similar behavior with even higher antioxidant activity than uncoated nanocarriers with a mean of 15,456 (±744), 27,233 (±535) and 38,344 (±898) TE/L/10 cells for 0.5%, 1% and 5% of oil, respectively. The antioxidant properties of dryTom-Ne were 10–13% higher than curc-Ne, and around 40% higher than freshTom-Ne. Gallic acid, a common antioxidant used as positive control, as reported in Figure 3.5B has a slight antioxidant property compared to nanoemulsions a mean of 10,245 (±886), 14,563 (±978) and 19,856 (±1023) TE/L/10 cells for 25, 50 and 100 µM, respectively.

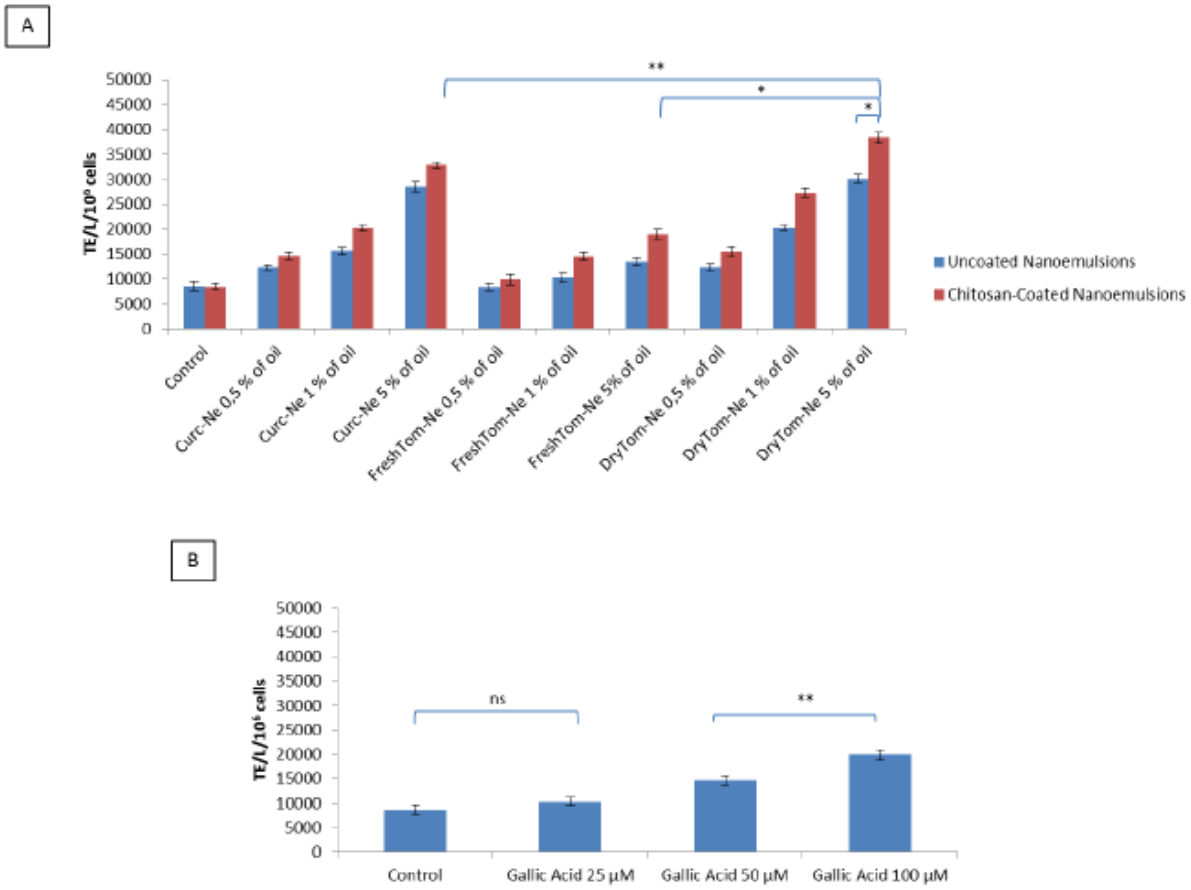

Figure 3.5. Mean antioxidant values (±SEM) of H9c2 cell lysates (TE/L/10^6 cells). Antioxidant values of cell lysates after challenge with 50 mL of AAPH (4 mM) for 10 min and recovery with PBS (control) or chitosan-coated or uncoated nutraceutical-loaded nanoemulsions (**A**) or gallic acid (**B**) at 25, 50 and 100 µM. * $p < 0.001$; ** $p < 0.05$.

Detection of Intracellular Reactive Oxygen Species.

The H9c2 cell lysate fraction served as a model to measure the antioxidative effect of nutraceutical-loaded nanocarriers under pro-inflammatory conditions induced by lipopolysaccharides (LPS) and doxorubicin (Figure 3.6). As reported elsewhere,[37] intracellular ROS production was higher in LPS-treated H9c2 cells due to the stimulation of the TLR4—NADPH oxidase 1 (NOX1) pathway. Treatment of cardiomyoblasts with LPS and doxorubicin increased the antioxidant properties by 50% and 55–60%, respectively, versus the control (Figure 3.6A). Incubation with nutraceutical-loaded nanocarriers invariably decreased oxidative status at all concentrations tested but not in a statistically significant manner at 0.5% oil, compared to untreated cells. Chitosan-coated dryTom-Ne, namely dryTom-Ne-CT, had the best antioxidant activity. Indeed, it reduced oxidative stress by 45–50%, similar to control cells, and by 45% similar to LPS- and doxorubicin-treated cells. In LPS-treated cells, the antioxidant activity of dryTom-Ne was 35% and 25% higher than that of freshTom-Ne and curc-Ne, respectively ($p < 0.001$). As shown in Figure 3.6B,D, Gallic acid used as positive control, had antioxidant effects both in LPS (Figure 3.6B) and Doxorubicin (Figure 3.6D) treated cells with a

reduction of oxidative stress of around 26% and 21% at 100 µM, respectively, compared to untreated cells ($p < 0.001$ for both).

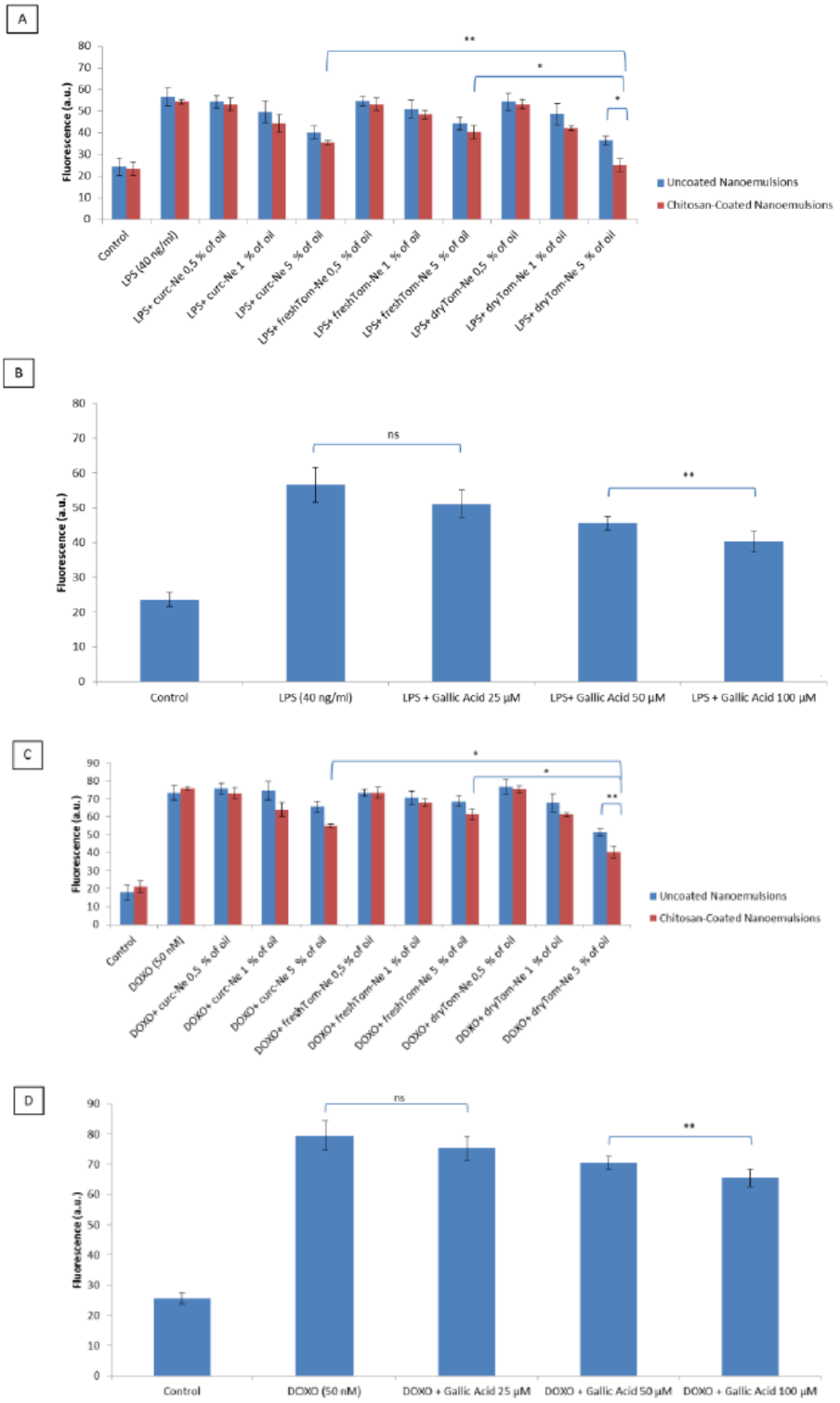

Figure 3.6. Detection of intracellular reactive oxygen species by fluorescence (a.u) in the H9c2 cell line (5000 cells/well). Cells were pretreated or not with uncoated and chitosan-coated nutraceutical-loaded nanoemulsions for 4 h before stimulation with 40 ng/mL of lipopolysaccharide (LPS) (**A**) or 50 nM of doxorubicin (**C**) for 24 h. Gallic acid was also exposed to cardiomyoblasts as positive control before stimulation with LPS (**B**) or doxorubicin (**D**). * $p < 0.001$; ** $p < 0.05$.

Lipid Peroxidation Studies.

As reported in Figure 3.7, nutraceutical-loaded nanocarriers significantly decreased the production of MDA and 4HNA by cardiomyoblasts under pro-inflammatory conditions (LPS) and chemotherapy (doxorubicin). Inhibition of lipid peroxidation is a cardioprotective strategy used to increase vascular and cardiac cell viability during anthracycline therapies. Specifically, curcumin-loaded nanocarriers, chitosan coated, at 5% oil reduced the formation of MDA and 4HNA by 31%and 23%, respectively versus LPS-treated cells ($p < 0.001$); dryTom-Ne had better lipid-antioxidant properties than the other nutraceuticals with reductions (at 5% oil) of MDA and 4HNA of 37.5% and 57%, respectively versus LPS-treated cells ($p < 0.001$). The same applies to doxorubicin-treated cells, which indicates that the same mechanism of action counteracts lipid peroxidation synthesis in the two nutraceuticals. As positive control, we analyzed effects of gallic acid as common antioxidant at the same conditions tested with nanoemulsions and, as reported in Figure 3.7E–H, at 100 μM, it reduced MDA and 4HNA production of around 26% and 21% in LPS treated cells and of 20% and 28%, respectively, in doxorubicin treated cells. However, based on all results obtained, chitosan-coated lycopene-enriched nutraceuticals, namely dryTom-Ne-CT, had the best biological properties of all the nutraceuticals evaluated thereby corroborating the results of the cell viability, antioxidant and cellular uptake studies.

Measurement of Nitric Oxide.

Nitric oxide initiates lipid peroxidation and, by interacting with superoxide anion, produces peroxynitrite which is implicated in atherosclerosis.[38] Peroxynitrites trigger lipid peroxidation, protein oxidation, nitration and activation of matrix metalloproteinases.[39] Under pro-inflammatory conditions and chemotherapy, cardiomyoblasts can produce NO. As shown in Figure 3.8A,B, H9c2 cells increase NO production under pro-inflammatory conditions and chemotherapy. Treatment with nutraceutical-loaded nanocarriers significantly inhibited NO production at all tested concentrations with inhibition percentages reaching 93% (very near to baseline concentrations) in the case of curc-Ne-CT and dryTom-Ne-CT at the maximum tested concentration (5% of oil). As shown in Figure 3.8, there was no significant difference between curcumin-loaded and high lycopene concentration nanoemulsions, for both uncoated and chitosan coated nanoemulsions, which suggests that the same mechanism of action underlies the NO inhibition of these bioactives. Also, in this experiment, the chitosan-coated nanoemulsions were more effective than the uncoated ones. As positive control, gallic acid at the maximum concentration tested (100 μM) inhibit of around 33 and 42% NO production under LPS and Doxorubicin exposure, respectively, compared to unpretreated cells.

Calcium Levels.

To determine the intracellular calcium level in cardiomyoblasts during LPS or doxorubicin treatments and the biological effects of nutraceuticals-loaded nanoemulsions, we used the fluorescence probe Fluo-3 AM as reported elsewhere,[40] LPS and DOXO treatment dramatically increased intracellular calcium levels in cardiomyoblasts compared to control cells ($p < 0.001$) for both. DryTom-Ne-CT treatment dose-dependently attenuated the overload of intracellular calcium in cardiomyoblastsas witnessed by the reduced fluorescence intensities of 8%, 19% and 55.6% at 0.5%, 1% and 5% ($p < 0.001$) compared to cells treated with LPS alone (Figure 3.9A). Similar behavior was seen for DOXO exposed cardiomyoblasts; specifically, dryTom-Ne-CT decreased calcium overload in H9c2 cells of 0.6%, 17% and 52% at 0.5%, 1% and 5% ($p < 0.001$) compared to only DOXO treated cells (Figure 3.9B). These results suggested that nutraceuticals-loaded nanoemulsions were able to reduce the overload of intracellular calcium in H9c2 cells induced by LPS and DOXO treatments.

Anti-Inflammatory Studies.

Given the anti-inflammatory activity of nutraceuticals, we investigated how nutraceuticals affect IL-8, IL-6, IL-1β, IL-10 and TNF-α production in cardiomyoblasts under pro-inflammatory conditions. As shown Figure 8, LPS at a dose of 40 ng/mL significantly stimulated the production of all interleukins analyzed versus untreated cells due to their binding with Toll Like Receptor type 4 (TLR4) expressed on the membrane of cardiomyoblasts leads to up-regulation of interleukins mRNA expression and their secretion. Pretreatment with all nutraceutical-loaded nanocarriers significantly decreased the level of all molecules analyzed (Figure 3.10). Specifically, dryTom-Ne-CTat 5% oil decreased the levels of IL-8, IL-6, IL1β and TNFα, by 58%, 64%, 67% and 65% respectively, versus LPS-treated cardiomyoblasts ($p < 0.001$). These effects are very similar to those observed for curcumin-loaded nanoemulsions (chitosan coated) thereby indicating very strong anti-inflammatory effects. Lastly, IL-10, dryTom-Ne and curc-Ne stimulated the release of IL-10 from cells under pro-inflammatory conditions.

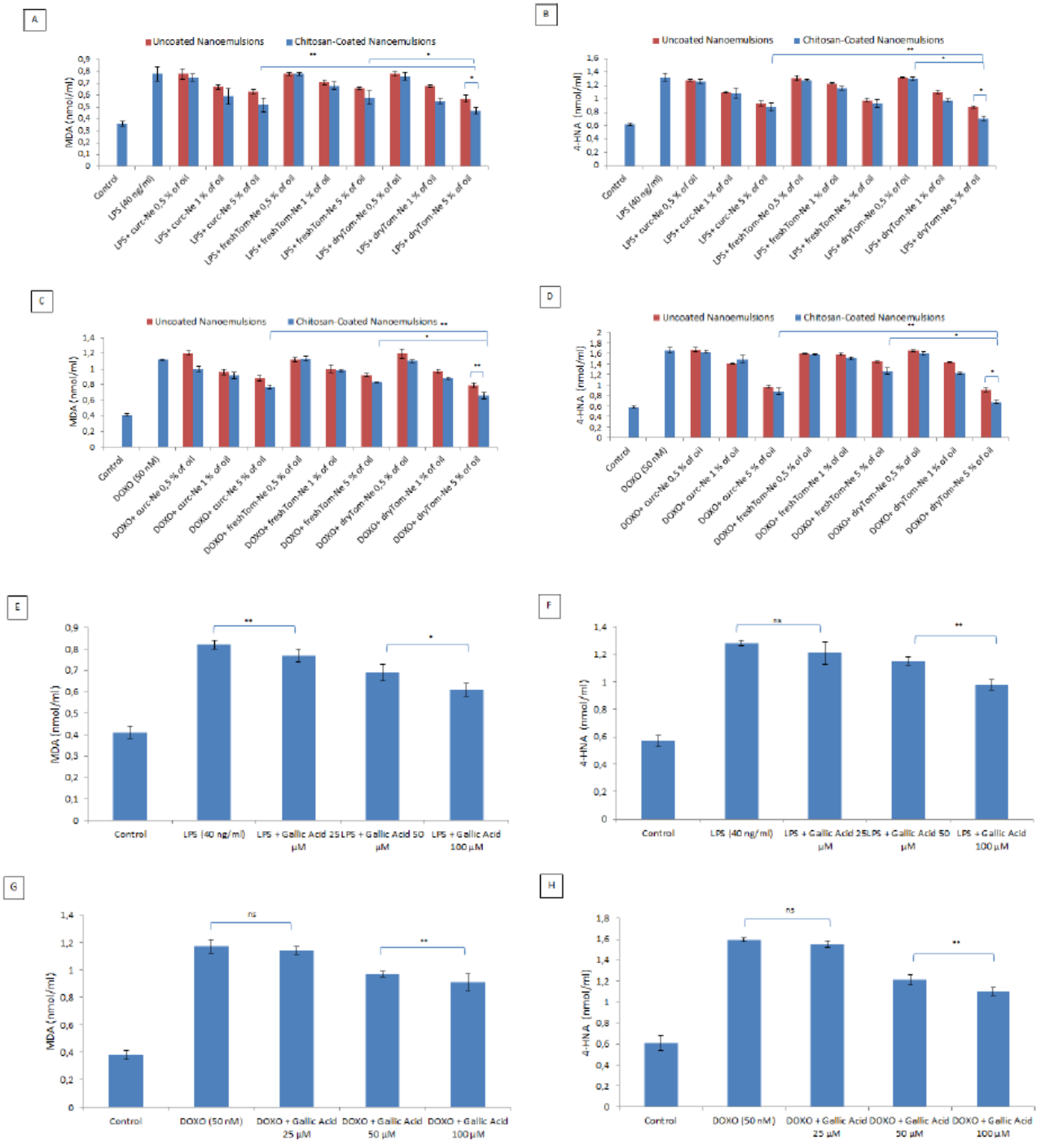

Figure 3.7. Cellular quantification of malondialdehyde (MDA) and 4HNA production under pro-inflammatory conditions and doxorubicin exposure. MDA and 4HNA (nmol/mL) production by cardiomyoblasts treated with LPS (**A,B**) and doxorubicin (**C,D**) alone or combined with uncoated or chitosan-coated nutraceutical-loaded nanocarriers at concentrations ranging from 0.5 to 5% oil. At the same condition, as positive control, we tested also the effects of gallic acid at 25, 50 and 100 µM (**E,F**) for LPS treatments; (**G,H**) for doxorubicin treatments). * $p < 0.001$; ** $p < 0.05$; ns: not significant.

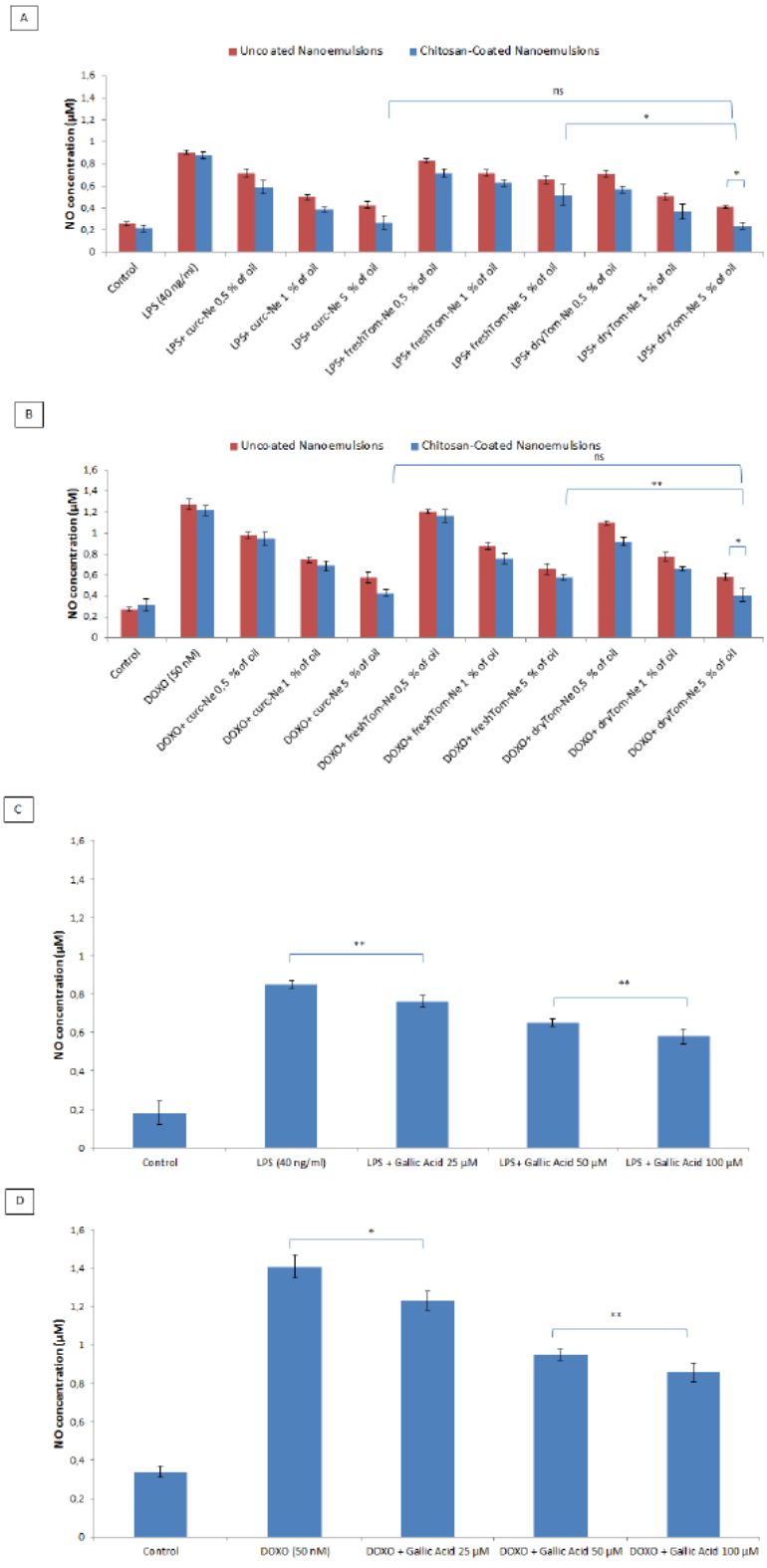

Figure 3.8. Measurement of nitric oxide (NO) production expressed as nitric oxide concentration (µM) in H9c2 cells (5000 cells/well). Cells were pretreated or not with uncoated and chitosan-coated nutraceutical-loaded nanoemulsions at 0.5%, 1% and 5% of oil 4 h before stimulation with 40 ng/mL of LPS (**A**) or 50 nM of DOXO, (**B**) for 24 h. Pretreatments were also performed by incubating cells with gallic acid, as positive control, for both LPS (**C**) and DOXO (**D**) treatments. * $p < 0.001$; ** $p < 0.05$; ns: not significant.

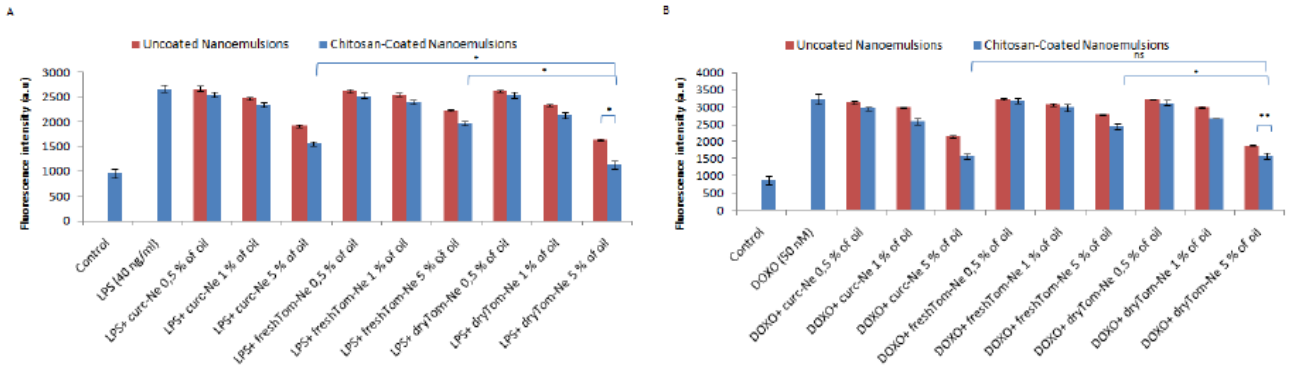

Figure 3.9. Intracellular calcium fluorescence staining in H9c2 cells (expressed as fluorescence intensity a.u). Cells were pretreated or not with uncoated and chitosan-coated nutraceutical-loaded nanoemulsions at 0.5%, 1% and 5% of oil for 4h before stimulation with 40 ng/mL of LPS (**A**) or 50 nM of DOXO, (**B**) for 24 h. * $p < 0.001$; ** $p < 0.05$; ns: not significant.

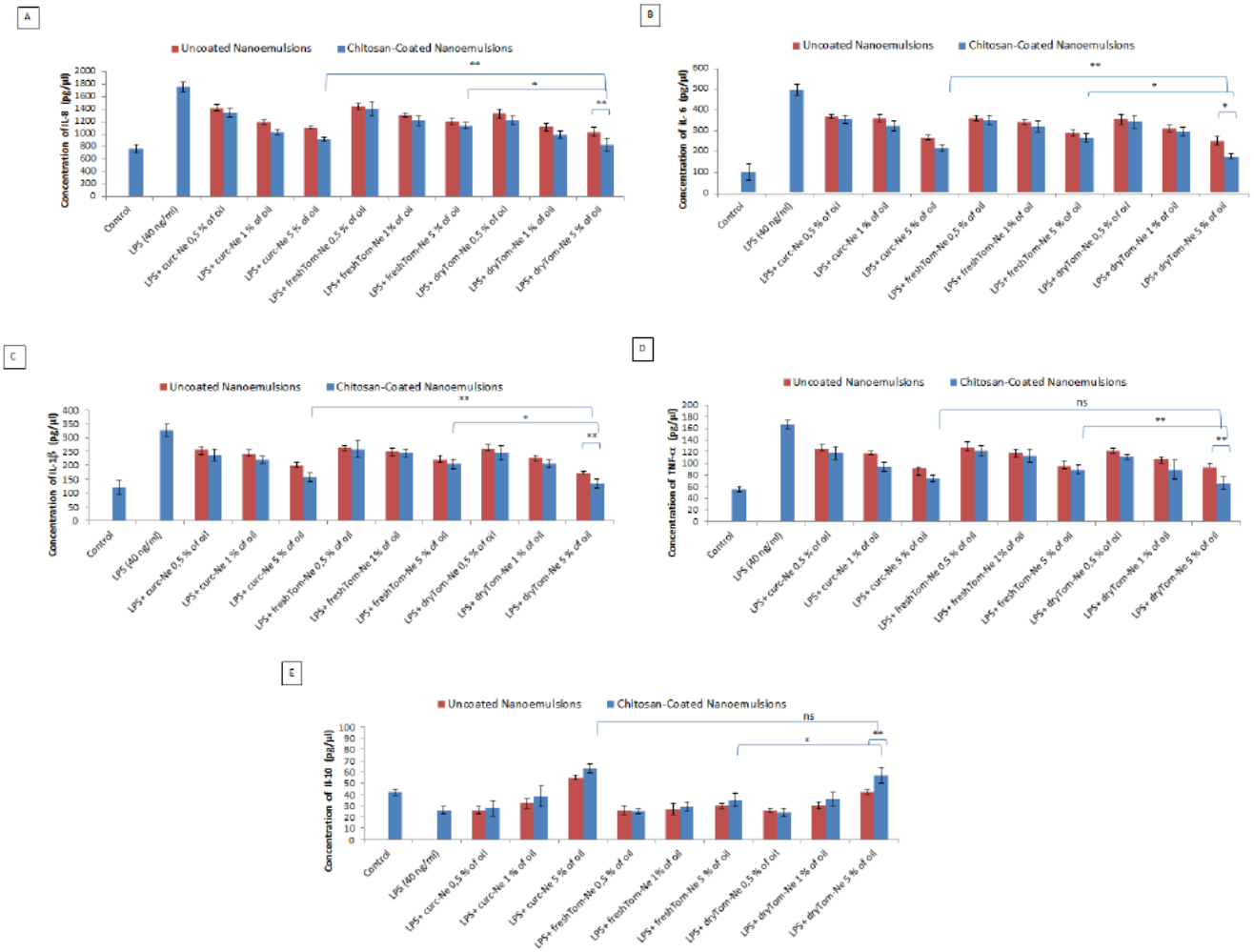

Figure 3.10. Anti-inflammatory effects of nutraceutical-loaded nanoemulsionson IL-8 (A), IL-6 (B), IL-1β (C), TNF-α (D) and IL-10 (E) production of cardiomyoblasts (at a density of 1.2 x 10^5 cells/well). Cells were treated or not with 0.1 mL of a 0.5%, 1% and 5% of oil of chitosan-coated and uncoated nanoemulsions for 5 h before exposure to lipopolysaccharides (40 ng/mL) for 12 h. * $p < 0.001$, ** $p < 0.05$; ns: not significant.

3.4 Discussion

Anthracyclines are powerful drugs used to treat a multitude of neoplasms; however, cardiotoxicity, which generally results from ROS overproduction, lipid peroxidation and mitochondrial damage, compromises their clinical applications. The heart and vascular microenvironments play key pathological roles in the etiology of cardiovascular disease related to some anticancer drugs and to radiotherapy. These recent observations are of extreme interest in cardioncology because several interleukins, cytokines, growth factors and hormones are crucial for cardiomyocyte survival. Specifically, IL-6 is a cytokine derived from T lymphocytes, macrophages and adipocytes, and acts via its membrane-bound or soluble receptor, stimulating C-reactive protein, fibrinogen hepatic synthesis, and joint inflammation and accelerating atherosclerosis processes. High IL-6 concentrations have been associated with an increased relative risk of myocardial infarction in healthy men. Moreover, IL-6 and its receptor levels have an early peak in the acute phase of myocardial infarction, probably due to plaque instability.[41] Moreover, recent clinical evidence supports the potential role of IL-8 in atherosclerosis, both as a marker or as a potential therapeutic target. In the field of interventional cardiology, it was suggested that increased serum levels of IL-8 after percutaneous coronary intervention could predict the development of heart failure in patients with acute myocardial infarction.[42] Another interleukin of interest in cardioncology is Interleukin-1 (IL-1) that plays an important role in the development and progression of coronary atherosclerosis and congestive heart failure. Moreover, IL-1 receptor antagonists exerted cardioprotective effects in rat myocardial ischemia-reperfusion injury and mouse viral myocarditis. Interestingly, doxorubicin treatment leads to overproduction of IL-1β in cardiac tissue, which suggests that this interleukin is involved in doxorubicin-related cardiotoxicity and apoptosis induction also by overloading calcium in cardiac cells. Moreover, IL-1 in association with nitric oxide (in the field of the NO-IL1β axis) can induce neonatal cardiac myocyte apoptosis even at very low concentrations.[43]

Under pro-inflammatory conditions such as LPS exposure, fibroblasts, monocytes, macrophages and cardiomyocytes secrete TNF-α.[44] Toll-like receptor 4 (TLR4), which is the main target of LPS, is expressed throughout the body including cardiomyocytes, and it is involved in the etiology of several cardiovascular diseases; for example, cardiac dysfunctions were frequently observed in patients with sepsis and also in animals injected with LPS.[45] These findings suggest that, the heart microenvironment, seen as the inflammation-interleukin-NO-ROS axis, could play a key role in the pathogenesis of cardiotoxicity. Consequently, new cardioprotective strategies that act on this network could optimize heart protection in patients undergoing cancer treatments. Nutraceuticals are natural bioactives that exert anti-inflammatory activities. Lycopene is a promising cardioprotective anti-inflammatory molecule that acts on the AMPK-mTOR pathway and exerts anti-atherosclerosis and

anti-myocarditis effects.[46] Lycopene, a naturally occurring hydrocarbon carotenoid found in red food such as tomatoes, pink guavas and watermelons has attracted considerable clinical attention as a potential chemopreventive agent against cardiovascular disease.[47] Interestingly, lycopene regulates Mg^{2+}-ATPase and maintains the Mg^{2+} balance during some anticancer therapies.[48] In addition, lycopene exerted heart-protective effects and improved cardiac function in preclinical models.[49] Curcumin suppresses the inflammatory cytokines IL-1,-1β, -6, and -8, TNF-α, and COX-2.[16] It was recently demonstrated that curcumin decreased several markers of doxorubicin-related cardiotoxicity in preclinical models, however its biological activities are limited by its reduced bioavailability.[12] Consequently, new formulations are required to optimize bioavailability of cardioprotective nutraceuticals during doxoribincin treatment. Biodegradable nanocarriers are promising pharmacological tools to increase in vivo accumulation of drugs and/or chemo-sensitizing agents in cancer therapy both by oral or by intravenous injection as we have recently shown with similar nanocarriers.[16,23]

Here we show that the nanoemulsions loaded with both curcumin and lycopene (derived from fresh or dry tomato extract) exert multiple molecular mechanisms of cardioprotection during doxorubicin treatment. The anti-inflammatory activities of the nanocarriers described herein hold potential in terms of modulating the heart microenvironment thereby providing insights for further preclinical studies, also in combination with other cardiotoxic anticancer drugs, namely anti-VEGF therapy and immunotherapies. Such studies could be valuable especially given the crucial role of interleukins in the pathogenesis of cardiac toxicity.

The results of this study demonstrate the cardioprotective effects of nanoemulsions loaded with nutraceuticals with abilities of cellular internalization with actin and ATP-dependent mechanism of uptake. However, we recognize that one limitation of our study is the use of only one type of cardiomyocyte and further investigations are required to explore the biological effects of nutraceutical-loaded nanoemulsions also in endothelial cells as well as in the co-culture of endothelial and adult cardiomyocytes. Preclinical studies are currently underway in our group to evaluate modification of left ventricular ejection fraction and factional shortening upon administration of nanocarriers during doxorubicin treatment, by using conventional murine models of cardiotoxicity often used by our research group.[50]

3.5 Conclusions

Doxorubicin-induced cardiotoxicity remains a major concern for patients receiving chemotherapy. There is great interest in identifying compounds and developing drugs aimed at reducing oxidative stress and lipid peroxidation as well as inhibiting the secretion of interleukin from cardiac cells. This

study shows that nutraceutical-loaded nanocarriers exert cardioprotective effects. Of particular translational interest are their effects on interleukins especially on IL1-β, considering its prognostic role in cardiology and its correlation with an increased relative risk of cardiovascular disease.[48] Nutraceuticals loaded in nanocarriers could be considered an emerging strategy with which to elicit cardioprotection from chemotherapies.

3.6 References

1. M. Fernandez-Chas, M.J. Curtis, S.A. Niederer, *Br. J. Pharmacol.,* **2018**, 175, 763-781.
2. D. Mele, C.G. Tocchetti, P. Pagliaro, R. Madonna, G. Novo, A. Pepe, C. Zito, N. Maurea, P. Spallarossa, *J. Cardiovasc. Med*., **2016**, 17 (Suppl. 1), e3–e11.
3. N. Maurea, C. Coppola, G. Piscopo, F. Galletta, G. Riccio, E. Esposito, C. De Lorenzo, M. De Laurentiis, P. Spallarossa, G. Mercuro, *J. Cardiovasc. Med*. **2016**, 17 (Suppl. 1), e19–e26.
4. T. Simůnek, M. Stérba, O. Popelová, M. Adamcová, R. Hrdina, V. Gersl, *Pharmacol. Rep.,* **2009**, 61, 154–171.
5. K. Wu, S.J. Schwartz, E.A. Platz, *J. Nutr.,* **2003**, 133, 1930–1936.
6. M. Pecoraro, M. Del Pizzo, S. Marzocco, R. Sorrentino, M. Ciccarelli, G. Iaccarino, A. Pinto, A. Popolo, *Toxicol. Appl. Pharmacol.,* **2016**, 293, 44–52.
7. A. Hosseini, E. Bakhtiari, S.H. Mousavi, *Iran. J. Pharm. Res*., **2017**, 16, 708–713.
8. I. Capasso, E. Esposito, N. Maurea, M. Montella, A. Crispo, M. De Laurentiis, M. D'Aiuto, G. Frasci, G. Botti, M. Grimaldi, et al., *Trials,* **2013**, 14, 273.
9. N. Maurea, C. Coppola, G. Ragone, G. Frasci, A. Bonelli, C. Romano, R.V. Iaffaioli, *J. Cardiovasc. Med*., **2010**, 11, 861–868.
10. P. Møller, S. Loft, C. Lundby, N.V. Olsen, *FASEB J*., **2001**, 15, 1181–1186.
11. K. Nakamura, K. Fushimi, H. Kouchi, K. Mihara, M. Miyazaki, T. Ohe, M. Namba, *Circulation,* **1998**, 98, 794–799.
12. A. Shehzad, F. Wahid, Y.S. Lee, *Arch. Pharm*., **2010**, 343, 489–499.
13. P. Mascio, S. Kaiser, H. Sies, *Arch. Biochem. Biophys*., **1989**, 274, 532–538.
14. G. Karimi, M. Ramezani, A. Abdi, *Phytother. Res*., **2005**, 19, 912–914.
15. R. Manikandan, M. Beulaja, R. Thiagarajan, A. Priyadarsini, R. Saravanan, M. Arumugam, *Eur. J. Pharmacol.,* **2011**, 670, 578–585.
16. R. Vecchione, V. Quagliariello, D. Calabria, V. Calcagno, E. De Luca, R.V. Iaffaioli, P.A. Netti, P.A., *J. Control. Release* **2016**, 233, 88–100.
17. C. Yucel, V. Quagliariello, R.V. Iaffaioli, G. Ferrari, F. Donsì, *Int. J. Pharm.,* **2015**, 494, 357–369.
18. V. Quagliariello, R.V. Iaffaioli, E. Armenia, O. Clemente, M. Barbarisi, G. Nasti, M. Berretta, A. Ottaiano, A. Barbarisi, *J. Cell. Physiol.,* **2017**, 232, 2063–2074.
19. A. Albini, B. Bassani, D. Baci, K. Dallaglio, M. Gallazzi, P. Corradino, A. Bruno, D.M. Noonan, *Curr. Med. Chem*., **2017**.
20. J.S. Nam, A.R. Sharma, L.T. Nguyen, C. Chakraborty, G. Sharma, S.S. Lee, *Molecules,* **2016**, 21, 108.

21. R. Vecchione, G. Luciani, V. Calcagno, A. Jakhmola, B. Silvestri, D. Guarnieri, V. Belli, A. Costantini, P.A. Netti, *Nanoscale,* **2016**, 8, 8798–8809.
22. R. Vecchione, G. Iaccarino, P. Bianchini, R. Marotta, F. D'autilia, V. Quagliariello, A. Diaspro, P.A. Netti, *Small,* **2016**, 12, 3005–3013.
23. R. Vecchione, V. Quagliariello, P. Giustetto, D. Calabria, A. Sathya, R. Marotta, M. Profeta, S. Nitti, N. Silvestri, T. Pellegrino et al., *Nanomedicine,* **2017**, 13, 275–286.
24. D. Naviglio, A. Formato, G. Scaglione, D. Montesano, A. Pellegrino, F. Villecco, M. Gallo, *Foods,* **2018**, 7, 107.
25. D. Naviglio, T. Caruso, P. Iannece, A. Aragòn, A. Santini, *J. Agric. Food Chem.,* **2008**, 56, 6227–6231.
26. R. Vecchione, U. Ciotola, A. Sagliano, P. Bianchini, A. Diaspro, P.A. Netti, *Nanoscale,* **2014**, 6, 9300–9307.
27. N. Kozukue, M. Friendman, *J. Sci. Food Agric.,* **2003**, 83, 195–200.
28. R. Meamar, L. Dehghani, M. Ghasemi, M. Saadatnia, K. Basiri, N.A. Faradonbeh, S.H. Javanmard, *J. Res. Med. Sci.,* **2013**, 18 (Suppl. 1), S1–S5.
29. P. Spallarossa, S. Garibaldi, P. Altieri, P. Fabbi, V. Manca, S. Nasti, P. Rossettin, G. Ghigliotti, A. Ballestrero, F. Patrone et al., *J. Mol. Cell. Cardiol.,* **2004**, 37, 837–846.
30. M. Barbarisi, R.V. Iaffaioli, E. Armenia, L. Schiavo, G. De Sena, S. Tafuto, A. Barbarisi, V. Quagliariello, *J. Cell. Physiol*., **2017**, 233, 6550–6564.
31. M. Huang, Z. Ma, E. Khor, L.Y. Lim, *Pharm. Res*. **2002**, 19, 1488–1494.
32. G. Gupta-Elera, A.R. Garrett, R.A. Robison, K.L. O'Neill, *Eur. J. Cancer Prev*., **2012**, 21, 155–162.
33. A.K. Pal, D. Bello, B. Budhlall, E. Rogers, D.K. Milton, *Dose Response,* **2012**, 10, 308–330.
34. T. Nagasaki, H. Matsumoto, Y. Kanemitsu, K. Izuhara, Y. Tohda, H. Kita, T. Horiguchi, K. Kuwabara, K. Tomii, K. Otsuka et al., *J Allergy ClinImmunol*., **2014**, 133, 1474–1477.
35. A. Almalik, P.J. Day, N. Tirelli, *Macromol. Biosci.,* **2013**, 13, 1671–1680.
36. Y. Fan, Y. Zhang, W. Yokoyama, J. Yi, *Nanomaterials,* **2017**, 7, 349.
37. X. Liu, C. Pei, S. Yan, G. Liu, G. Liu, W. Chen, Y. Cui, Y. Liu, *Tumour. Biol.,* **2015**, 36, 1493–1502.
38. N.S. Dhalla, R.M. Temsah, T. Netticadan, *J. Hypertens.,* **2000**, 18, 655–673.
39. E. Takimoto, D.A. Kass, *Hypertension,* **2007**, 49, 241–248.
40. Y. Zhu, Z. Feng, W. Cheng, Y. Xiao, *Mol. Med. Rep.,* **2018**, 17, 8457–8465.
41. B.C. Bacchiega, A.B. Bacchiega, M.J. Usnayo, R. Bedirian, G. Singh, G.D. Pinheiro, *J. Am. Heart Assoc.,* **2017**, 6, e005038.

42. S. Apostolakis, K. Vogiatzi, V. Amanatidou, D.A. Spandidos, *Cardiovasc. Res.,* **2009**, 84, 353–360.
43. J. Zhu, J. Zhang, L. Zhang, R. Du, D. Xiang, M. Wu, R. Zhang, W. Han, *Biomed. Pharmacother*., **2011**, 65, 481–485.
44. M.V. Singh, P.D. Swaminathan, E.D. Luczak, W. Kutschke, R.M. Weiss, M.E. Anderson, *J. Mol. Cell. Cardiol*., **2012**, 52, 1135–1144.
45. J. Cha, Z. Wang, L. Ao, N. Zou, C.A. Dinarello, A. Banerjee, D.A. Fullerton, X. Meng, *Ann. Thorac. Surg*., **2008**, 85, 1678–1685.
46. S. Ojha, S. Goyal, C. Sharma, S. Arora, S. Kumari, D.S. Arya, *Hum. Exp. Toxicol.,* **2013**, 32, 492–503.
47. P. Bansal, S.K. Gupta, S.K. Ojha, M. Nandave, R. Mittal, S. Kumari, D.S. Arya, *Mol. Cell. Biochem*. **2006**, 289, 1–9.
48. B.W. Van Tassell, S. Toldo, E. Mezzaroma, A. Abbate, *Circulation,* **2013**, 128, 1910–1923.
49. X. Wang, H. Lv, Y. Gu, X. Wang, H. Cao, Y. Tang, H. Chen, C. Huang, *J. Mol. Histol*. **2014**, 45, 113–120.
50. C.G. Tocchetti, A. Carpi, C. Coppola, C. Quintavalle, D. Rea, M. Campesan, A. Arcari, G. Piscopo, C. Cipresso, M.G. Monti et al., *Eur. J. Heart Fail.,* **2014**, 16, 358–366.

Chapter 4

Oil Core - PEG Shell Nanocarrier for *In Vivo* MRI Imaging

This work is under revision for publication in Advanced Health Care Materials: Vincenzo Calcagno, Raffaele Vecchione, Vincenzo Quagliariello, Pasquina Marzola, Alice Busato, Pierangela Giustetto, Martina Profeta, Sara Gargiulo, Chiara Di Cicco, Hui Yu, Marco Cassani, Nicola Maurea, Marcello Mancini, Teresa Pellegrino, Paolo A. Netti, Oil Core - PEG Shell Nanocarrier for In Vivo MRI Imaging.

Abstract

Oil-in-water emulsions represent a promising carrier for *in vivo* imaging because of the possibility to convey poorly water-soluble species. To promote accumulation at the tumor site and prolong circulation time, reduction of carrier size and surface PEGylation play a fundamental role. In this work a novel, simple method to design an oil-core/PEG-shell nanocarrier is reported. A PEG-shell is grown around a monodisperse oil-in-water nano-emulsion with a one-pot method, using the radical polymerization of poly(ethylene glycol)diacrylate. PEG polymerization was triggered by UV, thus obtaining a PEG-shell with tunable thickness. This core-shell nano-system combines the eluding feature of the PEG with the ability to confine and preserve high payloads of lipophilic species in the oil core. Indeed, the core was successfully loaded with a lipophilic contrast agent, namely super paramagnetic iron oxide nano-cubes. Interestingly, it was demonstrated an *in vitro* and an *in vivo* MRI response of the nanocapsules. Additionally, when the nano-system loaded with nanocubes was mixed with a fluorescent contrast agent, Indo-cyanine green, a synergic photo-acoustic effect was observed. Moreover, viability and cellular uptake studies showed no significant cell cytotoxicity. These results, together with the choice of low cost materials and the scale up production, make this nanocarrier a potential platform for in vivo imaging.

4.1 Introduction

Nanoparticles (NPs), with dimensions below 100 nm[1] and in contrast to macroscopic materials, have a high ratio of surface to volume and the way in which they interact with matter is unique. As consequence, several nanoparticle formulations have found remarkable applications in biophysical studies, biological sensing, imaging, medical diagnostic, and cancer therapy.[2] NPs have high payload efficiency, stability, and signal enhancement. Moreover, due to their dimensions – larger than molecules and smaller than cells and tissues – they possess advantageous features compared to other therapies and imaging agents. For example, NPs show an enhanced permeability to cancer tissue than in healthy tissue, since they exploit the difference in capillary structure between these tissues.[3]

Despite these advantages, their application may be limited by their inadequate clearance characteristics. Indeed, small NPs can be rapidly removed by the vascular system, while large NPs can accumulate and be retained in the body for long time, also thanks to their high stability.[4,5] Recently, we proposed the use of nano-emulsions as a vehicle for magnetic cobalt-ferrite NPs as imaging contrast agents.[6] The nano-emulsions developed by us possess some pharmaceutical and clinical advantages, such as easy of manufacture, scalable production, good biocompatibility, biodegradability, reasonable stability and the possibility to incorporate hydrophobic drugs and inorganic NPs.[7,8]

In general, the ability to extend the circulation times in blood depends largely on the carrier size and the physicochemical properties of the surface.[9] Modifying the surface with a hydrophilic polymer such as poly(ethylene glycol) (PEG) is widely used - as a strategy to alter protein absorption and prolong circulation time with consequent enhanced accumulation at the tumor site.[10] The mechanisms of preventing opsonization by PEG – and subsequent excretion by reticuloendothelial system (RES) – include the shielding of the surface, the increased surface hydrophilicity and the enhanced repulsive interaction between polymer-coated nanocarriers and blood component.[11] More recently, Schöttler et al.[12] demonstrated that, in addition to reducing protein adsorption, PEG – and poly(ethyl ethylene phosphate) (PEEP) – can modify the composition of proteins that surround nano-particles (protein corona), and the presence of specific proteins is required to prevent non-specific cellular uptake. As a protecting polymer, PEG provides a very attractive combination of properties: excellent solubility in aqueous solutions, high flexibility of its polymer chain, very low toxicity, immunogenicity, and antigenicity, lack of accumulation in the RES cells, minimum influence on specific biological properties of modified pharmaceuticals.[11,13]

In light of these observations, in this work we propose a novel synthetic strategy to prepare oil core – PEG shell nanocarriers (PEG-NE). Compared to other procedures widely proposed,[14-18] our strategy results simple to be performed and low cost. It consists of a photo-activated radical polymerization of poly(ethylene glycol) diacrylate (PEGDA), directly performed on the oil-water interface. The PEG shell was functionalized with a methacrylate dye (Rhodamine B), thus demonstrating that the outer surface can be further modified to accomplish to other functions such as optical imaging. Furthermore, the oil core - of 100 nm - was loaded with cubic iron oxide nanoparticles (IONC, 14 nm). Compared with cubic cobalt ferrite nanocubes,[19] used in a previous work, IONCs have higher biocompatibility and also result exploitable for both magnetic resonance imaging (MRI) and photo-acoustic imaging (PAI). *In vitro* PA tests, cell viability and uptake studies were also performed to evaluate the biocompatibility and the potentiality of this PEG-NE as diagnostic tool for imaging.

4.2 Results and Discussion

Nanocarrier design and physico-chemical characterization.

The presented nanocarrier is a core-shell system consisting of an oil-core and a PEG-shell. We chose a monodisperse oil-in-water (O/W) emulsion as the morphology-casting template to obtain the final nano-capsules. We used highly monodisperse O/W nano-emulsions with droplet size of around 90–110 nm, a polydispersity index (PDI) <0.1 and a ζ-potential <−30 mV, as measured by DLS. The size of the starting nano-emulsion is crucial since the final capsule should be small enough to pass through the human capillaries and, in particular, to exploit the difference in capillary structure between healthy

and tumor tissues (EPR effect). This difference allows to discriminate against healthy and tumor tissues with a favourable drug accumulation at the tumor site – thus obtaining the passive targeting.[3,20] To provide a PEGylated shell a simple, one-pot synthesis has been designed. This strategy relies on a different approach with respect to the ones proposed in literature to obtain PEGylated nano-emulsions.[14] PEGylation typically involves chemical attachment of PEG chains onto individual lipid monomers which are subsequently incorporated into the carrier systems.[15] The resulting PEGylated lipid based nano-system has a hydrophobic lipid structure camouflaged by an outer PEG region. The most common strategy to cover the surface with PEG is to use a PEG-modified surfactant. Distearoylphosphatidylethanolamine (DSPE)-PEG, at defined PEG chain lengths and structure, have been used to prepare and investigate PEG-coated nano-emulsions;[16,17] and modified DSPE-PEGs have also been used to further functionalize the outer surface for active targeting.[18] However, this approach is not fully convincing because of the use of such PEG-surfactant species that are costly – even more if they are designed to add target moieties – and because the coverage of PEG layer on particle surface is very critical: the length of the PEG chains, the PEG amount and the overall surface composition must be finely balanced to obtain suitable PEG coated nano-emulsions.[17]

Conversely, in our procedure a photo-activated polymerization is performed directly at the oil-water interface of the nano-emulsion to create a solid PEG shell. The sequence of mixing of the reactants and the intervals between each step have been set to obtain with any certainty the shell around the oil-core. Indeed, as depicted in Figure 4.1, a saturated water solution of Darocur 1173 is firstly added to the nano-emulsions suspension to allow the absorption of the photoinitiator on the oil surface. In this way, it is possible to guide the following PEG polymerization selectively at the oil-water interface. Darocur 1173 is a hydroxyphenilketone used to generate free radical species.

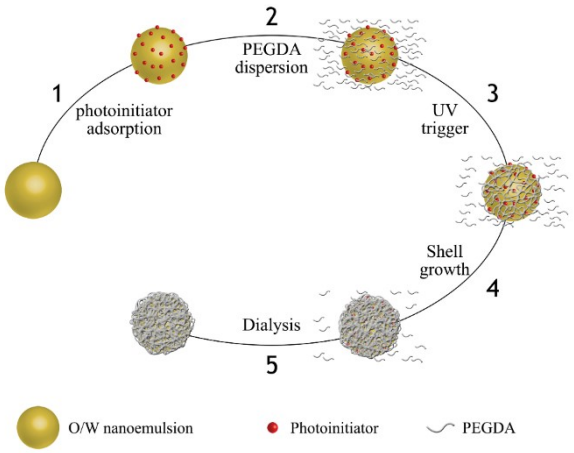

Figure 4.1. Schematic synthesis protocol of a core/shell type nanocarrier with a lipophilic core and a PEGylated shell. The photoinitiator, adsorbed on the oil nano-emulsion at the interface with water, allows to activate and guide the shell growth on the oil template.

The UV photo-cleavage of this molecule generates a benzoyl radical and a α-hydroxyalkyl radical, both of which are able to react with the acrylate double bond (Figure 4.2A).[21] The addition of the photoinitiator solution to the O/W nanoemulsion, together with the following addition of the water solution of PEGDA700, does not affect the size distribution of the nano-emulsion, as verified through DLS measurements (see Supporting Information, Tables S1). Once added photoinitiator and monomer, the radical polymerization (Figure 4.2B) was triggered with a UV irradiation (365 nm, 20 minutes).

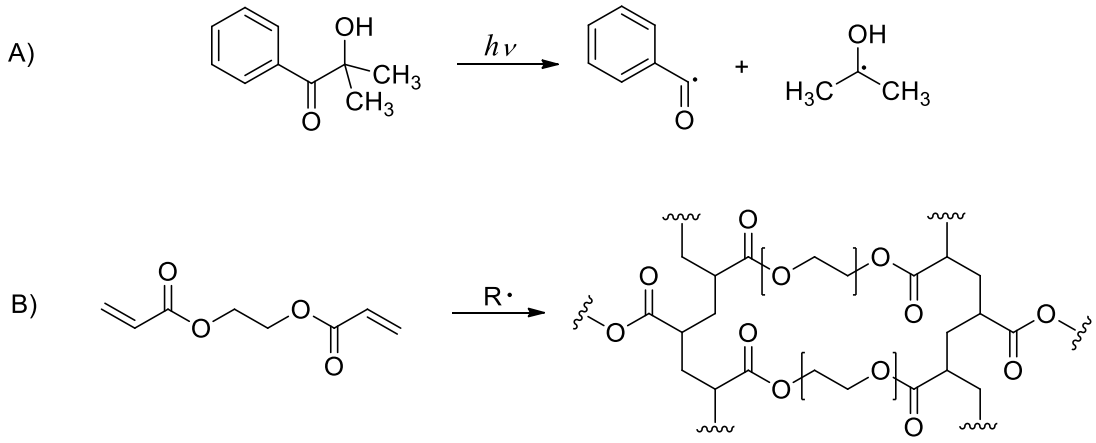

Figure 4.2. A) Photocleavage of hydroxyphenylketone with the production of two radical species, a benzoyl radical and a α-hydroxyalkyl radical; B) the free radical obtained from the cleavage of the photoinitiator initiate the polymerization of PEGDA forming a polymer network.

The irradiation does not determine any immediate increase in the particle size, but it starts the polymerization. In fact, by following the evolution of the size with the time, it is noteworthy that the size increases gradually (Figure 4.3), suggesting that the polymerization goes on until all the monomers of PEGDA in solution are consumed. A fine tuning of the shell thickness is obtained, as confirmed by the following observations. Firstly, the increase of the particle size has been tracked for several days and it can be noticed that size increases up to a plateau, but PDI is still rather below a value of 0.1. In a second test, we followed the same protocol but taking care to avoid any interaction of the system with the ambient light: once the UV irradiation has been performed no increase of the particle size is detected (see Figure S1 in the Supporting Information). In another case the polymerization is stopped by dialyzing the sample and, again, no increase of the particle size is detected (see Figure S1 in the Supporting Information). We decided to use the dialysis as a purification step of the standard procedure since it enables to stop the polymerization at the desired shell thickness and to remove the excess of unreacted species, which can have toxic effects. Of course, an alternative procedure with a prolonged use of the UV irradiation could have been designed – thus

obtaining the same shell growth in a shorter time – but such an intensive irradiation may affect the food grade materials of the oil-core[22] and especially it can lead to the degradation of light sensitive molecules.[23] In the proposed procedure the polymerization is stopped before the size growth reaches the plateau, as smaller PEG-nanoparticles begin to form spontaneously (see Figure 4.4D and Supporting Information, Figures S4).

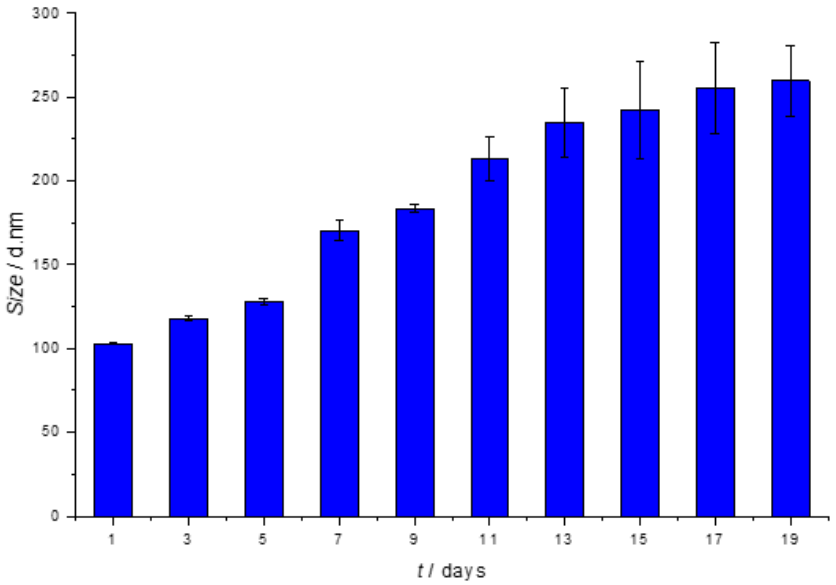

Figure 4.3. Particle size growth as function of the time. Error bars are derived from standard deviation over 3 sample preparations.

PEG-NE were further characterized by Electron and Confocal Microscopy. In particular, the morphological analysis was performed using TEM. For PEG-NE with only 1 day of reaction time, the shell was very thin and the only way to obtain micrographs was by Cryo-TEM. However, the observation was rather difficult as the nano-capsules are composed of low-contrast materials and, as shown in Figure 4.4A, the micrograph of PEG-NE with 1-day reaction time displayed the presence of a nanocarrier with narrow distribution but a core-shell system was not yet appreciable. Instead, for sample obtained after a longer reaction time, traditional TEM could be carried out and an OsO_4 staining could be performed obtaining a better image contrast. The Figure 4.4B depicts a TEM image of PEG-NE after 5 days of reaction time. The aggregation is only due to the drying process, as confirmed from cryo-TEM analysis (Figure 4.4A and C). Finally, for very long reaction times, like 30 days, the shell structure could be clearly seen by traditional TEM and a mutation from a smoother to a fuzzy surface can be appreciate (Figure 4.4D and Inlet).

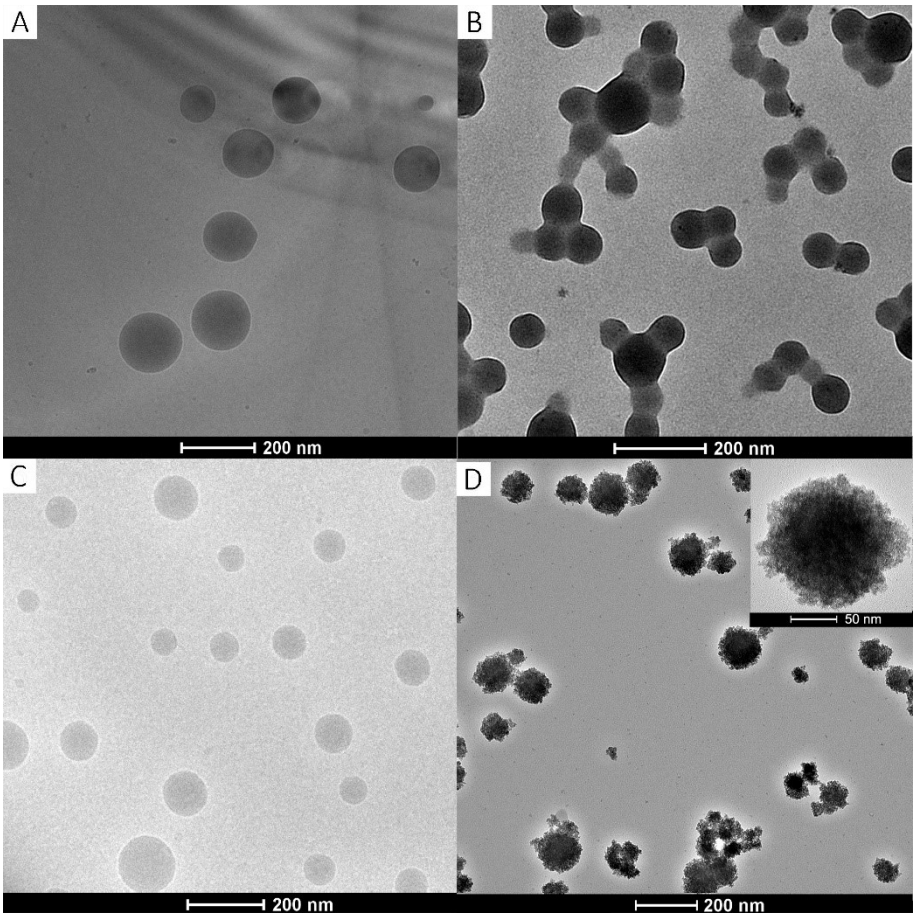

Figure 4.4. Micrographs of PEG-NE at different reaction times: A) Cryo-TEM micrograph after one day of polymerization; B) TEM micrograph after 5 days of polymerization, sample stained with OsO_4 vapours; C) Cryo-TEM micrograph after 5 days of polymerization; D) TEM micrograph after 30 days of polymerization, sample stained with OsO4 vapours. In the inlet of Figure D, it can be better appreciated the irregular surface of the shell after long shell growth. Images and inlet scale bars are 200 nm and 50 nm, respectively.

For fluorescent analysis both the core and the shell of PEG-NE were marked with a fluorescent dye. In detail, the inner oil-core was loaded with FITC (Supporting Information, Figure S5). As described in previous works, the liquid template can encapsulate dyes (e.g. nile red[24] and fluorescein[7]) or contrast agents (e.g. iron oxide NPs and CdSe QDs[24,25]), thus suggesting a possible multi-imaging of the final nanocarrier. On the other side, the outer shell was conjugated with Rhodamine B (Figure 4.5) by simply adding a methacrylate derivative of the dye during the shell growth. The shell modification did not bring any noticeable change in size or aggregation (see Supporting Information, Table S2) showing further possibility to add a contrasting functionality to the system. Moreover, this approach represents a very simple method to functionalize the outer PEGylated surface and, therefore, may be further exploited to add bioactive molecules for active targeting.[26]

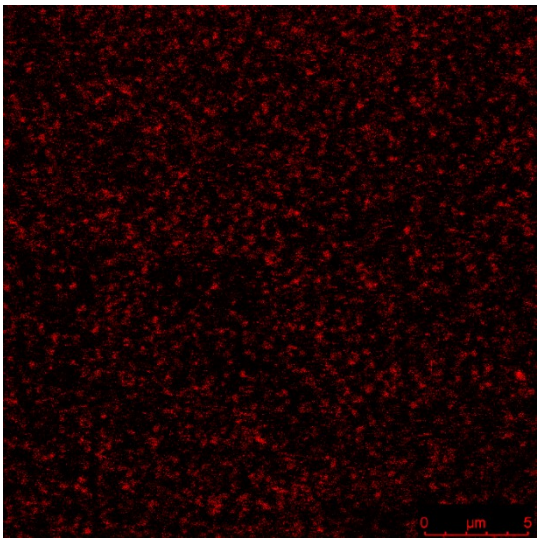

Figure 4.5. Confocal image of nano-capsules labelled with Rhodamine B on the outer PEGylated shell. Scale bar 5 µm.

Cell viability and cellular uptake studies.

As clearly shown in Figure 4.6A-D, confocal images depict a time dependent overall uptake of fluorescent PEG-NE, obtained by loading FITC in the oil core, in human breast cancer cells with a peripheral localization after 0.5 h of incubation and a more central accumulation after 24 h (Figure 4.6, D). Therefore, in summary, PEG-NE seems to localize mainly on the cell membrane and in the juxtamembrane region (Figure 4.6A and 4.6B) at short time of incubation. A quantitative uptake of the fluorescent PEG-NEs was performed by fluorescence analysis. As reported in Figure 4.6E, a great cellular accumulation of the proposed nanocarrier can be noticed.

To understand how the proposed nanocapsules can have an impact on the biocompatibility of the resulting nano-system, PEG-NE@IONC (i.e. PEG-NE loaded with IONC) were tested in terms of cytotoxicity on human breast cancer cells. As shown in Figure 4.7, even after 24 h of contact with cells, the PEG-NE@IONC did not show any significant decrease in cell viability.

Additionally, cellular uptake studies of PEG-NE@IONC, (see Figure S4 C and D for TEM characterization) were also performed to qualitatively asses the presence of the iron. In more detail, intracellular iron was detected by means of Prussian blue staining, while cells nuclei were counterstained using Nuclear Fast Red. As can be seen in Figure 4.8, blue spots were observed in the majority of cells and seemed to be localized around the cell membrane and throughout the cytoplasm, indicating a significant cellular uptake of the IONCs. We did not observe any blue staining of the control cells (image not shown). All these considerations remark the ability of this PEG-NE as a potential bio-safe nanocarrier for cancer imaging.

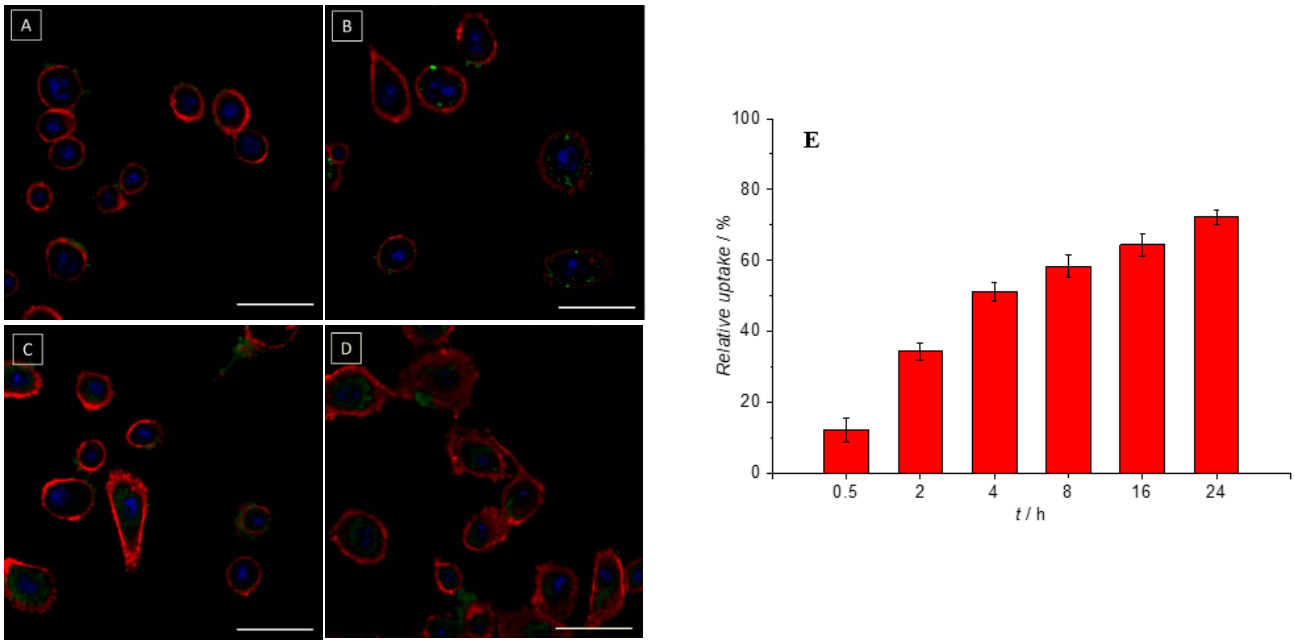

Figure 4.6. Cellular images by Confocal Laser Scanning Microscope of MCF-7 cells (5000 cells/well) after 0.5 h (A), 4 h (B), 8 h (C) and 24 h (D) of incubation with fluorescent PEG-NE at 0.05% of oil. Green signal: fluorescent PEG-NE; Red signal: cellular membrane labelled with concanavalin A tetramethylrhodamine conjugate; Blue signal: nucleus labelled with TO-PRO 3 Iodide. Scale bar: 50 µm. E) Overall cellular uptake quantification of MCF-7 cells ($5x10^3$ cells/well) from 0.5 up to 24 h of contact with fluorescent PEG-NE at 0.05 % of oil.

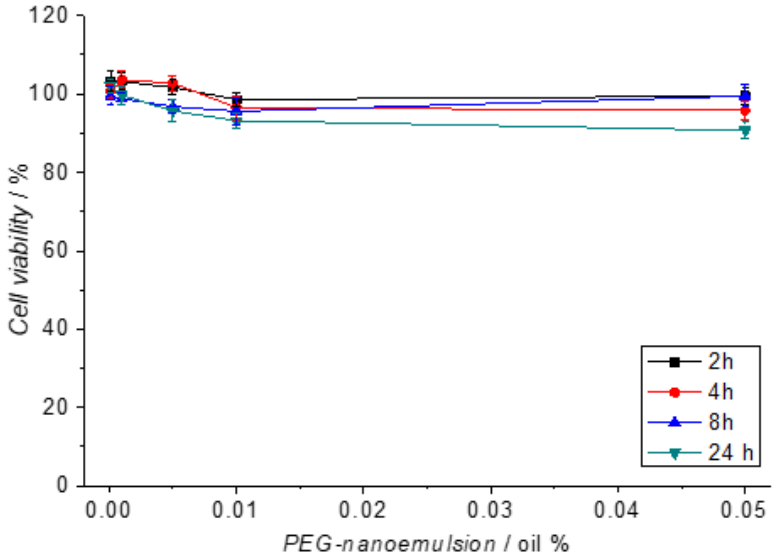

Figure 4.7. MCF-7 cell viability (± SEM) performed by modified MTT method as in function of the time (from 2 up to 24h of incubation time) and concentration of PEG-NE@IONC (from 0.001 up to 0.05 % of oil).

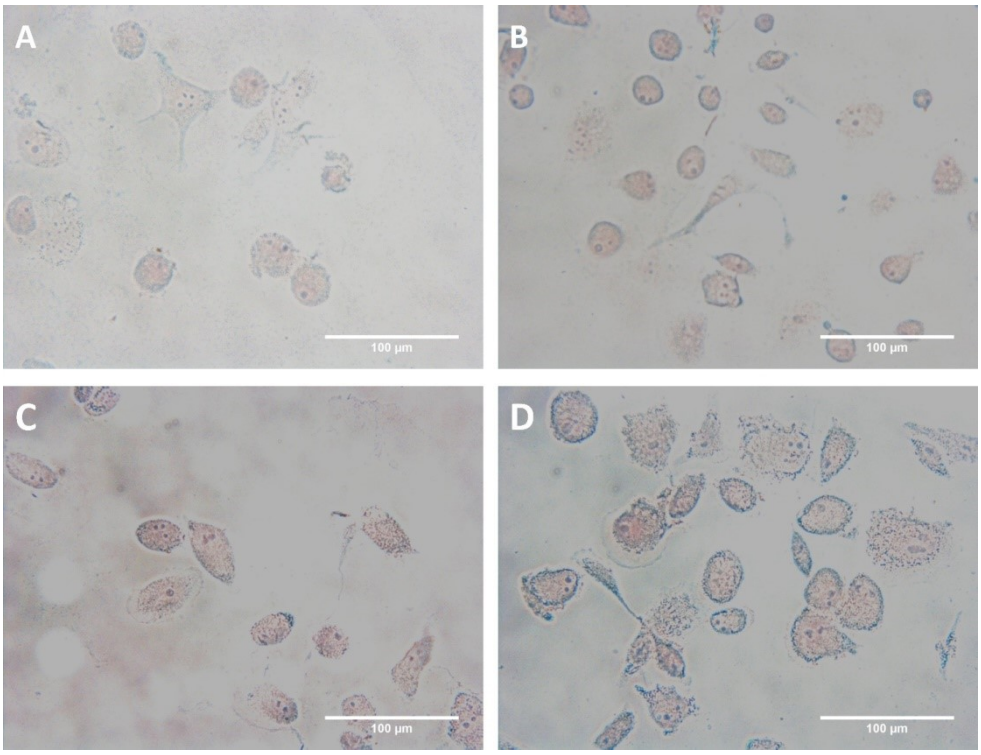

Figure 4.8. Prussian blue staining of MCF-7 cells after 30 min (A), 4 h (B), 8 h (C) and 24 h (D) of exposure to PEG-NE@IONC. Scale bar 100 µm.

Photo-acoustic and MRI analysis.

Photoacoustic imaging is a new diagnostic tool with non-invasive and non-ionizing properties which provides high sensitivity, and excellent resolution typical of acoustic methods.[27] It is based on the generation of acoustic waves by the absorption of electromagnetic energy, thus overcoming the limited spatial resolution of the conventional optical imaging of soft tissues.[28] To accentuate the image contrast, a contrast agent material (with an organic or inorganic nature) can be administered to a patient. Herein, we used oil nanodroplets to convey lipophilic inorganic nanoparticles acting as contrast agents and a PEG shell for its antifouling properties.

In vitro tests were performed to determine the variation of the intensity values of the photo-acoustic signal as a function of the excitation wavelengths of the laser beam (Figure 4.9). Each trend of the curves was calculated according to the ROI outlined in the area of analysis and by identifying the region where the photo-acoustic signal was significant and perceivable. Each curve is expressed as the average of five measurements, performed at different points of the sample tube. For all curves, the standard error of the mean (SEM), expressed as a percentage, ranged from 8% to 10%. The results evidence that the stock PEG-NE@IONC and the corresponding samples diluted in PBS showed a good photo-acoustic signal intensity, as expected (Figure S6, Supporting Information). On the contrary, the photoacoustic signal of the sample resulted to be sensibly attenuated after dilution with the blood (Figure 4.9A). To confirm this, it is possible to use the Spectragryph 1.1 software to make

a spectral addition of different components, thus predicting and taking into account the effect of blood dilution (Figure 4.9B). These results seem to prevent a photoacoustic application of pristine PEG-NE@IONC since the signal derived from IONC should not be detectable at the concentration used for the experiments. However, by adding a fluorescent contrast agent, namely the ICG, at a concentration which is not detectable alone, we observed an interesting synergic effect. In fact, as shown in Figure 4.9A and B, we observed an increase in the photo-acoustic intensity above the blood spectrum (both for OXY and DEOXY components), especially in the high frequency of range from 680 to 760 nm, which cannot be merely attributed to the sum of the contributions from PEG-NE@IONC and ICG.

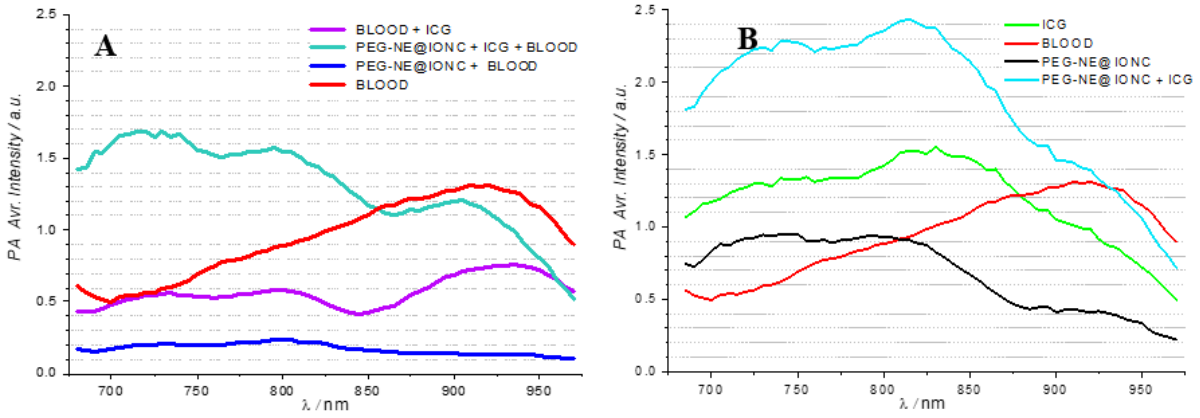

Figure 4.9. PA in vitro study of PEG-NE@IONC. A) PA average intensity as a function of the wavelength for blood (red line), PEG-NE@IONC+blood (blue line), ICG+blood (violet line) and PEG-NE@IONC+ICG+blood (green line). B) Combined spectral analysis: PA spectra obtained by ICG plus PEG-NE@IONC (cyan line) – its trend is comparable with PEG-NE@IONC+ICG+blood in the spectrum (A). SEM = 9.5%, n = 5. Additional spectra are calculated with SpectraGryph software.

This synergic behaviour may be due to an accumulation of ICG onto the surface of the PEG-NE@IONC that enhances the ICG response, as it was also reported in the case of single walled carbon nanotubes.[29]. No variation of the in vitro detected signal was registered upon multiple stimulation cycles confirming the stability of the proposed nano-system combined with ICG (data not shown).
Additionally, PEG-NE@IONC showed a relevant magnetic response thus confirming a possible dual imaging, Figure 4.10. In particular, water solutions of PEG coated nanoemulsion doped with iron oxide nanocubes were diluted in a range of concentration from 0.039 mM to 0.00162 mM in Fe. The highest concentration of 0.039 mM was obtained by concentrating three times the initial solution of PEG coated nanoemulsion, on a permanent neodymium magnet with an overnight exposure.

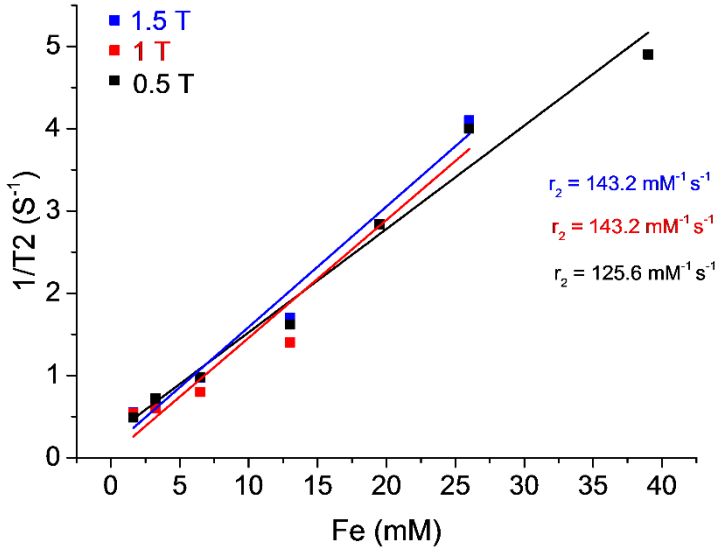

Figure 4.10. Inverse relaxation time T_2, as a function of different Fe concentrations containing in PEG-NCs and under different magnetic field.

The solution of PEG coated nano-emulsion, not doped with magnetic nanocubes (as control), was diluted using the same dilution factor of the nanocubes containing solution. The longitudinal (T_1) and transverse (T_2) relaxation times were measured at 40 °C using a Minispec spectrometer (Bruker, Germany) mq 20 (0.5 T), mq 40 (1 T) and mq 60 (1.5 T). T_2 relaxation time was measured using a Carr–Purcell Meiboom Gill (CPMG) spin–echo pulse sequence with 5000 data points with inter echo time of 0.5 ms. The relaxivities r_2 was determined by the following equation:

$$\frac{1}{T2} = \frac{1}{T2\ (H2O)} + r2\ CFe$$

where C_{Fe} is the concentration of Fe, T2(H_2O) the relaxation time of pure water and T2 the measured value of relaxation time of the solution. Data are reported in Fig. 4.10. The slope of the best fitting straight lines represents the transversal relaxivity r_2 of PEG coated nanoemulsion doped with iron oxide nanocubes at the different magnetic fields. The values of r_2 are comparable to those reported for other iron-oxide based contrast agents.[30] For control, transversal relaxation times have been also measured for the PEG coated nanoemulsion not doped with magnetic nanocubes. As expected, undoped nanoemulsions did not affected the water relaxation time (data not shown). Finally, within the experimental error, no significant change has been detected in the longitudinal relaxation time T_1.

Consequently, further investigations have been conducted *in vivo* by performing an *in vivo* MRI detection of PEG-NE@IONC after intratumoral injection.

Representative coronal T2-weighted images of tumor mass before and after intratumoral injections of 200 µL (11% w/v of oil in water emulsion containing iron nanocubes at concentration of ~20 ng/mL corresponding to ~ 0.4 µmol of Fe) of PEG-NE@IONIC are shown in Figure 4.11. In vivo MR images revealed that PEG-NE@IONIC nanoparticles were clearly detectable in the tumor tissue: post-contrast MR images showed areas of strong signal drop as expected for a T2 relaxing contrast agent. Areas of signal drop were detected in both the subcutaneous region (asterisks in Fig. 4.11, frames c, d) and within the tumor tissue (arrows in Fig. 4.11, frames c, d). Histological examination of tumor mass confirmed the presence of iron. Prussian Blue staining showed several blue-stained areas at the periphery of the tumor tissue (asterisks in Fig. 4.11, frame e) and inside the tissue (arrows in Fig. 4.11, frame f) corresponding to the signal drop areas detected in MRI.

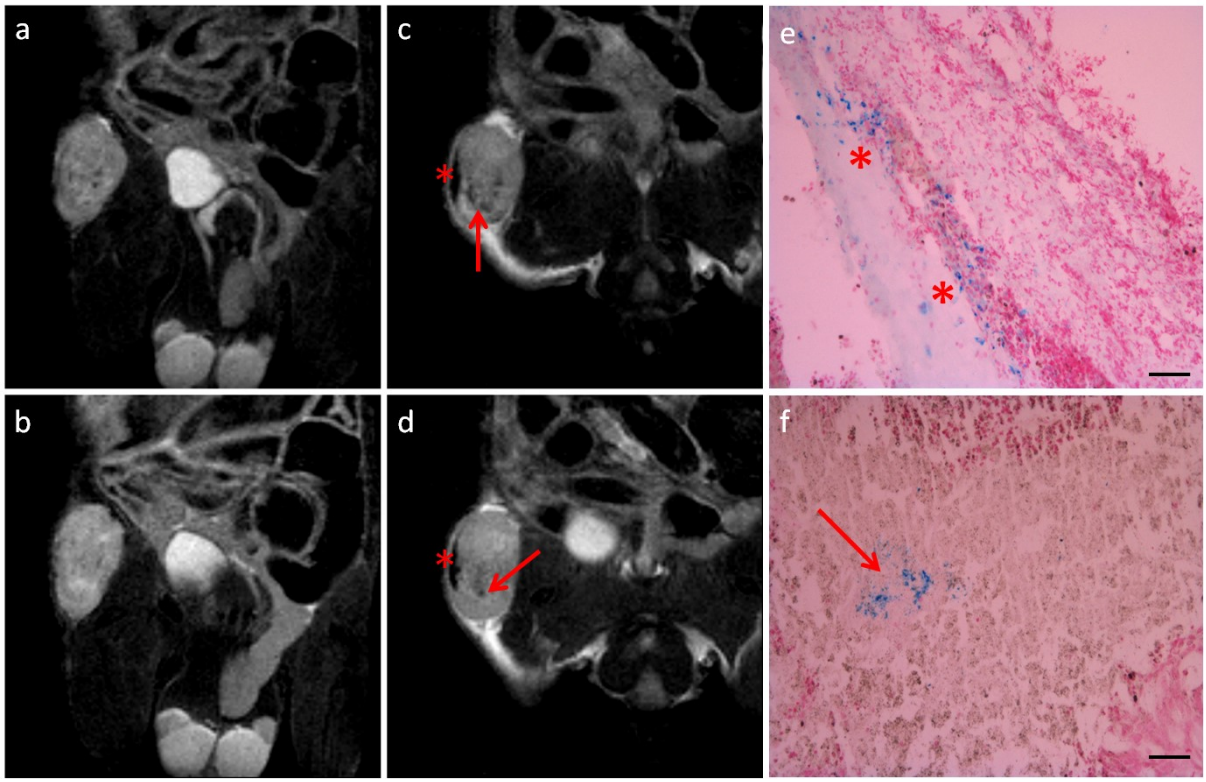

Figure 4.11. Consecutive T2W MRI slices acquired in vivo before (a-b) and after (c-d) intratumor injection of PEG-NE@IONIC; the presence of PEG-NE@IONIC is clearly detectable in slices acquired after the injection of the contrast agent as hypointense areas (frames c-d, asterisks and arrows). The tumor mass was excised for histological examination with Prussian Blue staining; representative histological slices from the excised tumor tissue with Prussian blue stained are reported in frames e-f: blue stained areas at tumor periphery (e, asterisk) and inside the tumor tissue (f, arrows) confirmed the presence of iron (magnification ×10, scale bar 50 µm).

4.3 Conclusions

Nano-emulsions represent a promising system for drug delivery and diagnostic, because of their ability to convey lipophilic compounds. In this work, oil-core/PEG-shell nano-capsules with a narrow size distribution have been successfully prepared. The synthetic strategy is based on a one-pot process in which a PEG shell is grown directly at the oil nano-droplet interface, exploiting the radical polymerization of poly(ethylene glycol) diacrylate. This core-shell nano-system retains an average size ranging from 100 to 200 nm, as a result of the polymerization time, but the increase in size does not affect the narrow size distribution. Moreover, a lipophilic contrast agent (IONC) has been preloaded in the oil core with no effects in the average size. Then, *in vitro* and *in vivo* MRI analysis have also assessed the possible use of PEG-NE for this kind of imaging. Additionally, thanks to the presence of this contrast agent it was demonstrated a relevant *in vitro* photoacoustic response with a synergistic mechanism when combined with a water-soluble contrasting agent, namely ICG. Therefore, we believe that PEG-NE represents an innovative, easy, low cost and green nanocarrier and that has the potentiality to be used as powerful tool for diagnostic.

4.4 Materials and Methods

Soy-bean oil (density at 20 °C of 0.922 g mL^{-1}), and Lipoid E80 Lecithin (egg lecithin powder 80–85% enriched with phosphatidylcholine (PC) and 7–9.5% content in phosphatidylethanolamine (PE) as per the manufacturer's specifications), were both purchased from Lipoid and used without further purification. Poly(ethylene glycol) diacrylate (PEGDA, 700 MW) and Fluorescein 5(6)-isothiocyanate (FITC) were purchased from Sigma Aldrich. Crosslinking reagent Darocur 1173 was purchased from Ciba. The dye Methacryloxyethyl thiocarbonyl rhodamine B was obtained from Polyscience Inc. Paclitaxel was purchased from Discovery Fine Chemicals Ltd.

Nanocarrier synthesis. Nano-emulsions were prepared through a three-step process, as already described.[8] Briefly, the initial step involved the preparation of a homogeneous oil phase by simply adding a certain amount of surfactant (Lipoid E 80, Lecithin (2.4g)) to a predetermined volume of soy-bean oil (20 mL) at 60 °C followed by sonication for a few minutes to homogenize and mix. In the second step a pre-emulsion was prepared by a step-by-step addition of the as-prepared oil phase to a weighed amount of aqueous phase (Milli-Q water), so as to obtain a final concentration of 20 wt% in the oil phase. The mixture was thoroughly mixed using an immersion sonicator for a few minutes in a beaker. A low temperature was maintained throughout the process by keeping this assembly inside a larger beaker containing ice in the form of a continuous ice jacket. Finally, in the third step the pre-emulsions were passed at 2000 bar through a high-pressure homogenizer

(Microfluidics M110PS) with a combination of individual cycles and continuous steps until minimum size and PDI were reached. For dye loading, 5 mL of an ethanol solution (Fluorescein 0.6% w/v in ethanol) were added to the oil phase before the pre-emulsion preparation step and the alcoholic solvent was evaporated at 60 °C for 30 minutes. Similarly, to prepare PEG-NE@IONC, 0.42 mL of IONC suspension in toluene (2.137 g/L of Fe) were added to the oil phase (20 mL) before the pre-emulsion preparation step and the aromatic solvent was evaporated at 60 °C for 90 minutes.
PEGylate shell was prepared through a simple procedure (see Figure 4.1). A saturated water solution of photoinitiator was prepared by adding 20 μL of Darocur to 1 mL of MilliQ water, mixing thoroughly (Vortex) and allowing the phase separation to occur. Equal volumes (500 μL) of photoinitiator supernatant solution and O/W nano-emulsion (5 wt%) were mixed (Vortex) and the resulting suspension was stored for 15 minutes. A water solution of PEGDA (3% w/v, 500 μL) was added to the suspension and mixed thoroughly (Vortex). After further 15 minutes of storage, the final suspension was irradiated with an UV source (Blak-Ray® Lamp with an intensity long-wave - 365nm – ultraviolet light) for 20 minutes at 5 cm distance. The resulting nano-capsules suspension was stored without any shielding for the ambient light. The photo-polymerization proceed till a dialysis against water was performed.

Synthesis of cubic iron oxide nanoparticles. Iron oxide nano-cubes (IONC) with edge size length of 14±2 nm were prepared accordingly to a procedure developed by the authors and previously reported.[19,31] Briefly, iron (III) acetylacetonate (Acros 99.9%, 0.353 g, 1 mmol) Decanoic Acid (Acros, 1.03 g, 6 mmol) Dibenzyl ether (Acros, 15 mL) and Squalane (Alfa Aesar, 10 mL) were mixed together in a three-neck flask of 100 mL, equipped with a water cooled Allhin condenser. The synthesis was conducted under nitrogen gas. After degassing the mixture at 65 °C for 120 minutes (29 $x10^{-3}$ mbar), the mixture was heated-up from 65 to 200 °C in 40 minutes and kept at this temperature for 2.5 hours. The temperature was further increased at 305 °C at a heat rate of 7°C/min and maintained at this temperature for 1 hour. After cooling, 10 mL of Chloroform were added to the crude of the reaction and the content was transferred in 3 falcon tubes of 50 mL in volume. To each falcon, acetone was added to a final volume of 50 mL. The tubes were centrifuged at 4000 rpm for 20 minutes. The supernatant was replaced with 5 mL chloroform for each falcon tube. After sonication, the sample was fully dispersed and the washing step with acetone was repeated two more time. As last step, the sample was re-dispersed in 10 mL toluene, ready to be used.

Particle Size and ζ-Potential measurements. Suspensions were characterized using a laser dynamic light scattering (DLS) instrument (Zetasizer zs nano series ZEN 3600, Malvern Instruments Ltd.,

Malvern, U.K., λ = 632.8 nm). All the samples were diluted up to a droplet concentration of approximately 0.025 wt% by using Milli-Q water. A detecting angle of 173° was used. A default refractive index ratio (1.5900) and 5 runs for each measurement (1 run lasting 100 s) were used in the calculations of the particle size distribution. ζ -potential analysis was carried out by setting 50 runs for each measurement.

Electron microscopy characterizations. Samples for TEM characterization were previously exposed for not less than 4 h to the vapour of an OsO_4 solution (1% w/v in water) as an oil core dopant that enhances the contrast of the images and confers robustness to the nano-capsules. About 5 μL of the sample was spread on a 200-mesh copper grid with carbon membrane (TED Pella, USA). After carefully removing the excess of solution the grids were left to dry overnight.
Frozen hydrated samples for Cryo-TEM characterizations were prepared by applying a 3 μL aliquot to a 200-mesh holey carbon grids (Ted Pella, USA). Each grid was blotted for 1.5 s in a chamber at 4 °C and 90% humidity using a FEI Vitrobot Mark IV (FEI company, the Netherlands) and then immersed into nitrogen cooled liquid ethane. The particles were imaged using a Tecnai G2 F20 transmission electron microscope (FEI company, the Netherland) and recorded at low dose with a 2 k × 2 k Ultrascan (Gatan, USA) CCD camera TEM and Cryo-TEM images were obtained using a TECNAI 20 G2: FEI Company (CRYO-TEM-TOMOGRAPHY, Eindhoven) equipped with a Schottky field emission gun operating at an acceleration voltage of 200 kV. TEM image were recorder with a camera Eagle 2HS; Cryo-TEM images were recorded with a Ultrascan (Gatan, USA) CCD camera; camera exposure time: 1 s; size 2048 × 2048.

Confocal and STED Microscopy. For Confocal Laser Scanning Microscope studies we followed the same procedure followed by our research work[7] MCF-7 cells were cultured in Dulbecco's Modified Eagle's Medium (Gibco) containing 10% v/v FBS, 1% v/v Pen-Strep at 37 °C in a humidified 5% CO_2 atmosphere. After, $5x10^3$ cells/well were seeded in a 24-well plate and allowed to grow for 24 h. For imaging studies, the medium was then replaced with fluorescent PEG-NE (at 0.05 % of oil) suspension in culture medium and incubated for 0.5, 4h, 8h and 24 h. After incubation time, cancer cells were thoroughly rinsed three times with PBS and fixed with a 2.5% glutaraldehyde in PBS for 20 min. Membrane staining was obtained by using Concanavalin A Tetramethylrhodamine Conjugate (Invitrogen, Life Technology) at a final concentration of 100 μg/mL. After washing in PBS, cells were blocked with 1% BSA in PBS for 20 min and washed three times with PBS. Using a Confocal Microscope (C1 Nikon) equipped with a EZ-C1 Software for data acquisition and 60x or 100x oil

immersion objective, the fluorescent PEG-NE was imaged through excitation/emission at 492/518 nm for, and the cell membrane with excitation/emission at 555/580 nm.

For STED/confocal analysis of fluorescent PEG-NE, a FC3510 dish was first washed with ethanol and dried. Then 200 μL of an aqueous solution of Poly-L-lysine (0.1 wt%, from Sigma Aldrich) were added in order to positively charge the dish surface. After 10 minutes, the dish was washed replacing the poly-lysine solution twice with 120 μL of water and then 120 μL of the sample (diluted 1:20 with water) were poured onto it. The excess of PEG-NE that not adhere to the glass surface was washed out replacing the solution twice with 120 μL of water and in the end with 120 μL of 5% (w/v) DABCO antifade solution (from Sigma Aldrich), taking care to left the central part of the dish always full of water. DABCO antifade was needed to reduce the bleaching effects on the dyes. Laser sources of 488 and 543 nm were used to excite the oil core with FITC from one side and PEG-shell with rhodamine B from the other side. The samples were imaged with a Leica TCS STED-CW microscope (Leica-Microsystems, Mannheim, Germany).

In Vitro cytotoxicity tests. Cytotoxicity of nanoemulsions was evaluated on hormone dependent human breast cancer cell line MCF-7 looking at their mitochondrial dehydrogenase activity by means of a modified MTT [3-(4,5-dimethyldiazol-2-yl)-2,5-diphenyltetrazolium bromide] method according to the manufacturer's instructions (Dojindo Molecular Technologies Inc., Rockville, MD). Breast cancer cells were seeded in 96-well plates at a density of 10000 cells per well in Dulbecco's Modified Eagle's Medium (Gibco) containing 10% v/v FBS, 1% v/v Pen-Strep at 37°C in a humidified 5% CO_2 atmosphere. After 24 h of appropriate growth, we tested PEG-NE at different concentration ranged from 0.001 up to 0.05 % w/v of oil in full medium and added them to the cells after washing them with PBS. Cells were then incubated from 2 up to 24 h under standard conditions. At the end of the incubation period MCF-7 cells were washed three times with PBS at pH 7.4 and incubated with 100 μL of a MTT solution (0.5 mg/L in cell culture medium) for 4 h at 37°C. The absorbance readings were acquired at a wavelength of 450 nm with the Tecan Infinite M200 plate-reader using I-control software. The relative cell viability (%) was calculated by the formula $[A]_{test}/[A]_{control}\times 100$, where "$[A]_{test}$" is the absorbance of the test sample, and "$[A]_{control}$" is the absorbance of the control cells incubated solely within culture medium. After evaluating cell cytotoxicity, the total protein content was measured by using the Micro BCA protein assay kit (Pierce). Briefly, cells were washed with ice-cold PBS, and incubated for 15 min in 150 μL cell lysis buffer (0.5% v/v Triton X-100 in PBS), to which 150 μL of Micro BCA protein assay kit reagent (prepared following the instructions of the manufacturer) were added. The absorbance at 562 nm was

finally measured on a plate reader. The cytotoxicity measurements were then normalized by the amount of total protein content in each well.

Cellular uptake. MCF-7 human breast cancer cells were grown in Dulbecco's Modified Eagle's Medium (Gibco) containing 10% v/v FBS, 1% v/v Pen-Strep at 37 °C in a humidified 5% CO_2 atmosphere. For cellular uptake experiments, $5x10^3$ cells/well were seeded in 24-well plate and allowed to grow for 24h. The medium was then replaced with 0.1 mL of a fluorescent PEG-NE (at 0.05 % w/v of oil) suspension and allowed to incubate for a time comprised between 0.5 and 24 h. Cells were then washed twice with PBS (pH 7.4), and after specified time intervals, the experiments were terminated by removing the supernatant, washing the cells three times with 10 mM PBS and lysing the cells with 0.1 ml of 0.5 % Triton X-100 in 0.2 N NaOH. The membrane-bound and internalized PEG-NE were quantified by analyzing the fluorescence of the cell lysate (λ_{exc} = 485 nm, λ_{em} = 535 nm), employing a calibration with 0.001 – 0.05 % of oil related on PEG-NE dispersed in a cell lysate solution (10^6 untreated cells dissolved in 1 mL of the Triton X-100/0.2 N NaOH solution). Nuclear staining was obtained by using TO-PRO 3 Iodide (Invitrogen, Molecular Probes Eugene, Oregon, USA) diluted 1/1000 after 1 h of contact.

For qualitative analysis of the intracellular iron, by means of light microscopy, cells were treated with PEG-NE@IONC for 30 min, 4h, 8h and 24 h. After the incubation time, cells were washed three times with PBS, in order to remove the non-internalized NE@IONC and then were fixed with a 2.5% glutaraldehyde in PBS for 20 min. Internalized NPs were stained incubating cells at room temperature for 1 h with Prussian blue working solution (1:1 mixture of 5% hydrochloric acid aqueous solution and 5% potassium ferrocyanide (II) trihydrate). After that, cells were washed twice with PBS and counterstained with Nuclear Fast Red solution at room temperature for 1 h. Each sample was then washed three times with PBS and images were acquired using a light microscope.

In vitro photo-acoustic analysis.

For photo-acoustic analysis, acquisitions were performed by using the VEVO-2100 LAZR (VisualSonics – Fujifilm System) photo-acoustic system. As the first step, a threshold value has been detected, to discriminate the photo-acoustic signal from the background noise. This operation has been carried out with a phantom, studied and performed with specific material characterized by acoustic impedance interfaces.[6] For PA acquisitions a 20 Hz tunable laser was used, with a wavelength range of 680-970 nm, a resolution of 40 μm and US transducer (LZ-250) which operates between 13 and 24 MHz. The values of parameters such as frequency, power output, gain, and height have been set constant for all PA acquisitions. To increase the statistic significance of *in vitro* scan

results, five measurements for each sample were performed in different points of a silicone tube, with internal diameters of 0.3 mm. Phantom structure and its features are compatible with the physics ultrasound and laser interaction. Samples consisting of PEG-NE@IONC were tested with this technique. Subsequent dilutions obtained different concentrations of PEG-NE@IONC with PBS and blood, respectively. The blood used was obtained from a mouse donor – Balb/C mouse in compliance with the protocols set by the Ethics Committee of IRCCS Hospital Pascale in Naples.

In vivo MRI analysis: Cancer cells culture and xenograft tumor model induction.

Human Colon Carcinoma cells (HT-29) purchased by ATCC (Manassas, VA), were cultured using Dulbecco's Modified Eagle's Medium with 10% fetal bovine serum (FBS), 100 U/mL penicillin, and 100 µg/mL streptomycin (all from GIBCO, Life Technologies, USA) and incubated at 37°C/5% CO_2 in 25 cm^2 plates. When at confluence, cells were washed twice with phosphate-buffered saline (PBS), treated with trypsin-EDTA 1% (GIBCO, Life Technologies, USA) and centrifuged at 1200 rpm for 5 min. The supernatant was discarded and cells pellet was resuspended in 2 mL of complete medium and counted. For xenograft tumor model induction, four nude homozygote male mice (Harlan Laboratories, Udine, Italy) were used. Mice were maintained under standard environmental conditions (temperature, humidity, 12 hours/12 hours light/dark cycle, with water and food *ad libitum*) and veterinarian assistance. The experimental plan received authorization from the Italian Ministry of Health (approval numbers 27/2012-B) and was approved by the Animal Care and Use Committee of the University of Verona. One million HT-29 cells, resuspended in 200 µL of sterile PBS, were subcutaneously injected in the right flank of anesthetized mice. Two weeks after tumor cells inoculation, mice were monitored by MRI to measure the tumor size and when tumor volumes ranged between 0.4 and 0.5 cm^3, PEG-NE@IONIC was injected intra-tumorally. MR images were acquired using a Bruker Tomograph (Bruker Optik GmbH, Ettlingen, Germany) equipped with a 4.7 T, 33 cm bore horizontal magnet (Oxford Ltd, Oxford, UK) having a maximum gradient strength of 40 G/cm. Animals were anesthetized by 1% isofluorane inhalation in a mixture of oxygen and nitrogen, placed in a prone position over a heated bed and inserted into a 3.5-cm internal diameter birdcage radiofrequency coil. T_2 weighted images were acquired before and after intratumoral injection (200 µL, 11% w/v of oil in water emulsion containing iron nanocubes at concentration of ~20 ng/mL corresponding to ~ 0.4 µmol of Fe) of PEG-NE@IONIC to detect the tumor mass and the presence of nanoparticles. T_2 weighted images were acquired in the coronal plane using a RARE sequence with TR=5000 ms, TE_{eff}=47.5 ms, NEX=1, field of view =3.5x7 cm^2, matrix size=140x280, slice thickness =1mm, flip angle =180°, Number of slices =10.

Histological analysis of tumor tissue. After *in vivo* MRI, the presence of PEG-NE@IONIC in the tumor tissues was confirmed by histological analysis. Mice were sacrificed and the tumor mass was dissected out, washed with PBS 0.1 M and fixed in 10% formalin for 4 hours. Tissues were embedded in paraffin and cut in 5 μm thick sections with a microtome and dried at 37°C for 24 h. In order to evaluate the presence of iron nanoparticle in the tissue, Prussian Blue (PB) staining was performed: sections were incubated with PB solution (5% hydrochloric acid and 5% potassium ferrocyanide) for 40 minutes and counterstained with nuclear fast red (Bioptica) for 10 minutes. Sections were examined under a light microscope (Olympus BXS1) equipped with a charge-coupled device camera.

Statistical Analysis. In Figure 4.3 data are presented as Mean ± SD, n = 3. Graphs of Figure 4.9 are obtained by the average over 5 scans in the spectral range of 650-1000 nm; SEM = 9.5%, n = 5. Cellular uptake has been performed in triplicate (n=3) in order to check eventual statistical differences. The difference between experimental groups was investigated by a one-way analysis of variance (ANOVA) and by a subsequent Turkey's multiple comparison test in Sigma Plot Software. For statistical analysis of all data, $p < 0.05$ was regarded as the lowest acceptable threshold for significance. All statistical analysis has been performed using Origin software (OriginPro 2017, OriginLab Corporation).

Supporting Information

DLS measurements.

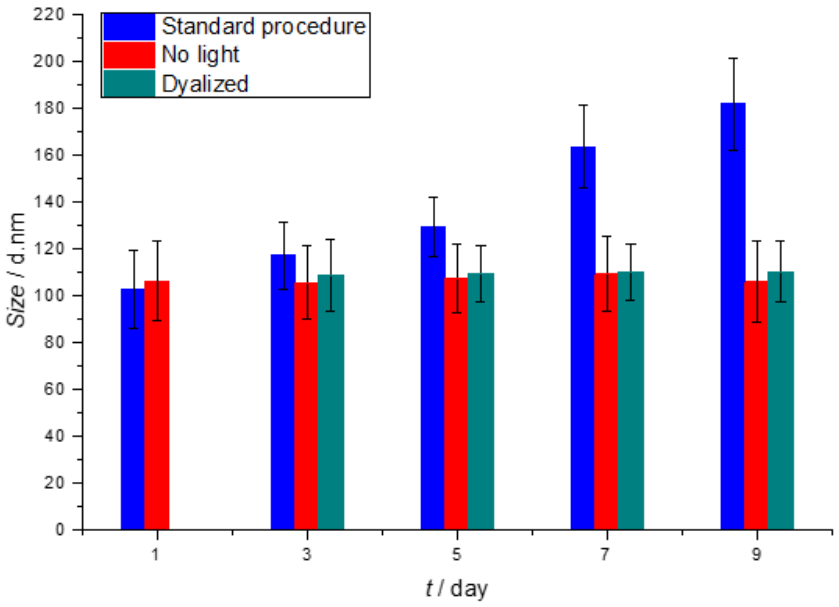

Figure S1. Comparison of the particle size growth between samples obtained with a standard procedure (blue bars), obtained by shielding the natural light (red bars) and by dialyzing the sample after 3 days (green bar). The sample dialyzed has been tracked for only 7 days because, due to the very thin shell, it resulted unstable for longer time. Error bars are derived from PDI value (PDI = $(SD/d)^2$) over 3 measurements of the same sample; see Tables below for the complete DLS reports.

Table S1. Size distribution (mean diameter, PDI and SD, n = 3) as a function of the time of PEG-NE prepared by the conventional method.

Time [days]	Size [d.nm]	PDI	SD [d.nm]
1	102.9	0.106	33.5
3	117.0	0.073	29.0
5	129.2	0.053	25.1
7	163.6	0.047	35.4
9	181.8	0.048	39.6
11	202.4	0.032	36.0
13	211.5	0.034	39.0
15	209.2	0.012	22.6
17	221.7	0.040	44.3
19	224.7	0.046	48.2
21	235.4	0.028	38.4
23	225.1	0.018	30.2
25	218.2	0.050	48.9
27	214.2	0.055	50.0

Table S2. Size distribution (mean diameter, PDI and SD, n = 3) as a function of the time of PEG-NE prepared by adding an acrylate dye (Methacryloxyethyl thiocarbonyl rhodamine B).

Time [days]	Size [d.nm]	PDI	SD [d.nm]
1	113.4	0.041	23.0
3	128.2	0.035	24.0
5	174.5	0.014	20.6
7	179.0	0.022	26.3
9	186.1	0.008	16.1
11	206.2	0.025	32.6
13	228.0	0.050	51.0
15	242.9	0.035	45.2
17	251.9	0.024	39.3
19	256.9	0.062	64.1
21	336.5	0.209	153.7
23	264.8	0.028	44.3
25	269.7	0.025	42.9
27	303.1	0.156	119.9

Table S3. Size distribution (mean diameter, PDI and SD, n = 3) as a function of the time of PEG-NE prepared by shielding the ambient light and by dialyzing the sample after 3 days of polymerization. The sample dialyzed has been tracked for only 7 days because, due to the very thin shell, it resulted unstable for longer time.

	No light			Dyalized		
Time [days]	Size [d.nm]	PDI	SD [d.nm]	Size [d.nm]	PDI	SD [d.nm]
1	106.3	0.099	33.5			
3	105.5	0.086	31.0	108.8	0.080	30.8
5	107.2	0.075	29.4	109.5	0.050	24.4
7	109.2	0.087	32.3	110.2	0.048	24.1
9	105.7	0.107	34.5	110.1	0.048	26.2
11	110.5	0.107	36.1			
13	110.5	0.112	37.0			
15	110.8	0.084	32.1			
17	110.5	0.089	33.0			
19	110.2	0.065	28.1			

TEM micrographs.

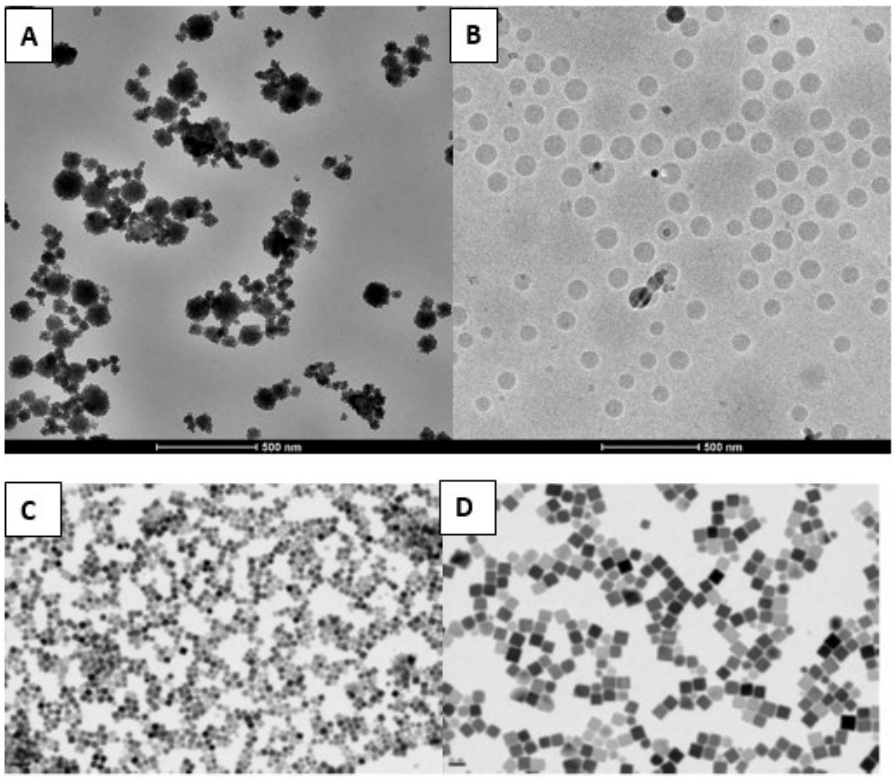

Figures S4. A: TEM micrograph of PEG-NE, stained with OsO_4, obtained after 30 days of shell growth. B: Cryo-TEM micrograph of the starting nano-emulsion. C and D: TEM micrographs of Iron Oxide Nano-Cube (IONC).

STED image.

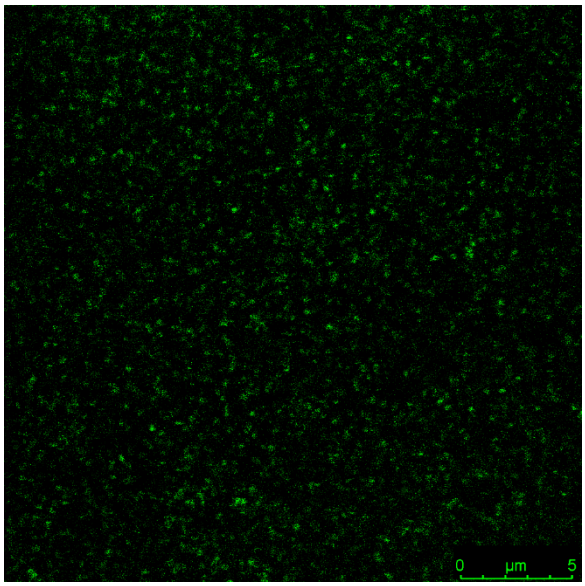

Figure S5. STED image of nano-capsules containing FITC in the oil-core. Scale bar 5 µm.

Photoacoustic spectra.

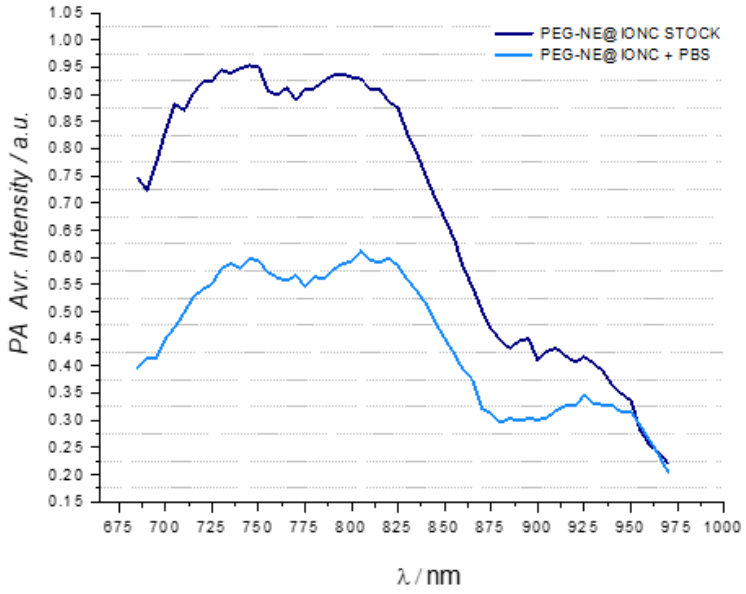

Figure S6. *In vitro* experiments showing the PA response of PEG-NE@IONC, in the stock formulation and in PBS (50 µL + 50 µL). Studying trends spectra with different dilutions can help to identify the smaller signal that PA system could detect.

4.6 References

1. V. Wagner, A. Dullaart, A.-K. Bock, A. Zweck, *Nat. Biotechnol*., **2006**, 24, 1211.
2. P. K. Jain, X. Huang, I. H. El-Sayed, M. A. El-Sayed, *Acc. Chem. Res.,* **2008**, 41, 1578.
3. J. Fang, H. Nakamura, H. Maeda, *Adv. Drug Del. Rev*., **2011**, 63, 136.
4. M. Longmire, P. L. Choyke, H. Kobayashi, *Nanomedicine (London, England),* **2008**, 3, 703.
5. B. Ballou, L. A. Ernst, S. Andreko, T. Harper, J. A. Fitzpatrick, A. S. Waggoner, M. P. Bruchez, Bioconj. *Chem.,* **2007**, 18, 389.
6. R. Vecchione, V. Quagliariello, P. Giustetto, D. Calabria, A. Sathya, R. Marotta, M. Profeta, S. Nitti, N. Silvestri, T. Pellegrino, *Nanomed. Nanotechnol. Biol. Med.,* **2017**, 13, 275.
7. R. Vecchione, V. Quagliariello, D. Calabria, V. Calcagno, E. De Luca, R. V. Iaffaioli, P. A. Netti*, J. Controlled Release,* **2016**, 233, 88.
8. R. Vecchione, U. Ciotola, A. Sagliano, P. Bianchini, A. Diaspro, P. Netti, *Nanoscale,* **2014**, 6, 9300.
9. S. S. Yu, C. M. Lau, S. N. Thomas, W. G. Jerome, D. J. Maron, J. H. Dickerson, J. A. Hubbell, T. D. Giorgio, *Int J Nanomedicine,* **2012**, 7, 799.
10. M. D. Howard, M. Jay, T. D. Dziubla, X. Lu, *Journal of Biomedical Nanotechnology* **2008**, 4, 133; R. A. Petros, J. M. DeSimone, *Nature reviews Drug discovery* **2010**, 9, 615.
11. V. P. Torchilin, *Adv. Drug Del. Rev*. **2012**, 64, 302.
12. S. Schöttler, G. Becker, S. Winzen, T. Steinbach, K. Mohr, K. Landfester, V. Mailänder, F. R. Wurm, *Nature nanotechnology,* **2016**, 11, 372.
13. S. Zalipsky, *Adv. Drug Del. Rev.,* **1995**, 16, 157.
14. S. B. Lim, A. Banerjee, H. Önyüksel, *J. Controlled Release,* **2012**, 163, 34.
15. D. Bhadra, S. Bhadra, P. Jain, N. Jain, *Die Pharmazie,* **2002**, 57, 5.
16. M. N. Khalid, P. Simard, D. Hoarau, A. Dragomir, J.-C. Leroux, *Pharm. Res.,* **2006**, 23, 752.
17. J. Rossi, S. Giasson, M. N. Khalid, P. Delmas, C. Allen, J.-C. Leroux, *Eur. J. Pharm. Biopharm.,* **2007**, 67, 329.
18. M. Talekar, S. Ganta, A. Singh, M. Amiji, J. Kendall, W. A. Denny, S. Garg, *Pharm. Res*., **2012**, 29, 2874.
19. P. Guardia, A. Riedinger, S. Nitti, G. Pugliese, S. Marras, A. Genovese, M. E. Materia, C. Lefevre, L. Manna, T. Pellegrino, *Journal of Materials Chemistry B,* **2014**, 2, 4426.
20. F. Alexis, E. Pridgen, L. K. Molnar, O. C. Farokhzad, *Mol. Pharm.,* **2008**, 5, 505.
21. J. Segurola, N. S. Allen, M. Edge, A. McMahon, S. Wilson, *Polym. Degradation Stab.,* **1999**, 64, 39; C. Decker, T. N. T. Viet, D. Decker, E. Weber-Koehl, *Polymer,* **2001**, 42, 5531.
22. E. Choe, D. B. Min, *Comprehensive reviews in food science and food safety,* **2006**, 5, 169.

23. M. Li, *Organic chemistry of drug degradation, Royal Society of Chemistry,* **2012**.
24. R. Vecchione, G. Luciani, V. Calcagno, A. Jakhmola, B. Silvestri, D. Guarnieri, V. Belli, A. Costantini, P. A. Netti, *Nanoscale,* **2016**, 8, 8798.
25. A. Jakhmola, R. Vecchione, D. Guarnieri, V. Belli, D. Calabria, P. A. Netti, *Adv. Healthcare Mater.,* **2015**, n/a.
26. A. B. Lowe, *Polymer Chemistry,* **2010**, 1, 17; C.-C. Lin, A. T. Metters, K. S. Anseth, *Biomaterials,* **2009**, 30, 4907.
27. L. V. Wang, S. Hu, *Science,* **2012**, 335, 1458; C. Zou, B. Wu, Y. Dong, Z. Song, Y. Zhao, X. Ni, Y. Yang, Z. Liu, *International journal of nanomedicine,* **2017**, 12, 179.
28. M. Xu, L. V. Wang, *Rev. Sci. Instrum.,* **2006**, 77, 041101.
29. S. Zanganeh, H. Li, P. D. Kumavor, U. Alqasemi, A. Aguirre, I. Mohammad, C. Stanford, M. B. Smith, Q. Zhu, *Journal of biomedical optics,* **2013**, 18, 096006.
30. E. Valero, S. Tambalo, P. Marzola, M. Ortega-Muñoz, F. J. López-Jaramillo, F. Santoyo-González, J. de Dios López, J. J. Delgado, J. J. Calvino, R. Cuesta, J. M. Domínguez-Vera, N. Gálvez, *J. Am. Chem. Soc,.* **2011**, 133, 4889–4895
31. P. Guardia, R. Di Corato, L. Lartigue, C. Wilhelm, A. Espinosa, M. Garcia-Hernandez, F. Gazeau, L. Manna, T. Pellegrino, *ACS nano,* **2012**, 6, 3080.

Appendix.

Future perspectives using a molecular formulation of Fe (III) in O/W nanoemulsion for MRI applications.

This work is performed in collaboration with Dr. Luca Menichetti (CNR-IFC, National Research Council Institute of Clinical Physiology) and Dr. Alessandra Flori ("G. Monasterio" Foundation - Regione Toscana - CNR Research Area)

Starting idea, preliminary results and outlooks.

As discussed in Chapter 1 and just demonstrated in Chapter 4, known the benefits of MRI as diagnostic tools and the safety of iron based nanoparticles as contrast agents, we are moving to explore a new design of our O/W LbL nanoemulsions. In this new strategy, we wish to study the possibility to prepare O/W LbL nanoemulsions encapsulating a molecular form of Fe(III), Fe(III)-oleate as contrast agent, and to study its MRI performance. Being a reddish-brown viscous oil, it is soluble in soyben oil, the oil core of our nanoemulsion. Furthermore, being a molecule, it permits us to scale more our nanoemulsion dimensions, improving their bioavailability. Fe(III)-oleate synthesis recalls some works in which it had applied to obtain with specific procedures iron nanoparticles.[1,2] The principal advantage of this protocol is the use of non-toxic and economical reagents, such as metal chloride and sodium oleate. We had followed this approach to synthetize Fe(III)-oleate but stopping before the subsequent preparation of iron nanoparticles. In fact, as said, our aim is to exploit the magnetic properties of iron in a molecular safe form able to be encapsulated in our smallest nanoemulsion formulation (less than 100 nm). In this appendix, we show some preliminary results, in terms of synthesis of Fe(III)-oleate, its encapsulation in our O/W nanoemulsions and the first MRI results of the O/W nanoemulsion loaded with it as contrast agents. This work is in coming and new experiments to encapsulate higher concentrations of Fe(III)-oleate, the MRI response of the new formulated O/W nanoemulsions and ICP characterizations of the synthetized molecule are in progress.

Preparation on the iron oleate complex loaded in O/W nanoemulsion.

Synthesis of iron oleate complex. The followed protocol was taken from literature, with slight modifications, in particular the use of $FeCl_3$ anhydrous (M_w=162.20 g mol^{-1}) to a better control of ferric environment as compared to an iron chloride hydrated ($FeCl_3 \bullet 6H_2O$).[1,2] Briefly, 20 mg of anhydrous iron chloride (0.123mmol) and sodium oleate (3.3eq, M_w=304.44) are dissolved within a solvent mixture of 147 µL ethanol, 110 µL Milli Q water and 257 µL hexane. Each reagent and solvent were purchased from Sigma-Aldrich. The resulting solution was heated at 70°C in reflux for 4 h under controlled atmosphere conditions. After that, to help the workup phase, 28mL of hexane were added to the resulting product. Then, the mixture was put in a separatory funnel and washed 3 times with 6 mL of MilliQ water. The organic phase containing the iron oleate mixture was then treated with $MgSO_4$ anhydrous and then hexane was evaporated by rotary evaporator. Then iron oleate complex was dried in a vacuum oven at 30°C overnight.

O/W nanoemulsion loaded with iron oleate complex.

As previously described,[3] 5.8 g of Lipoid E 80 (egg lecithin powder 80-85% enriched with phosphatidylcholine and 7–9.5% content in phosphatidylethanolamine) was dissolved in 24 mL of soy-bean oil (density at 20 °C of 0.922 g mL^{-1}) at 60 °C. To obtain the control empty nanoemulsion, the oil phase was then added dropwise to the aqueous phase (Milli-Q water) and mixed using the immersion sonicator (Ultrasonic Processor VCX500 Sonic and Materials). The obtained pre-emulsion was then homogenized at 2000 bar by a high-pressure homogenizer (110P series microfluidizer) to obtain the final 20% wt oil in water nanoemulsion. In the case of iron loaded nanoemulsion, the nanoemulsion was loaded with around 78 mg of iron oleate complex, dissolved in 4-5 mL of ethanol, adding it in the oil phase in the pre-emulsion step, after lecithin. This mixture was left under stirring at 70°C for 1 h to allow ethanol evaporation before continuing the pre-emulsion preparation with the addiction of the oil phase to the aqueous phase. The rest of the procedure was the same. By DLS analysis, the prepared samples were in accordance with our typical monodispersed nanoemulsion. No-loaded 20 %wt O/W nanoemulsion was characterized by: 98.61nm (st.dev.1.19), PDI 0.102 (st.dev. 0.022), ζ-Potential -24.9mV (st.dev. 0.7); Iron oleate loaded 20 %wt O/W nanoemulsion was characterized by: 98.23nm (st.dev. 1.30), PDI 0.079 (st.dev. 0.014), ζ-Potential -30.8mV (st.dev. 5.2)

Evaluation of relaxation performance of the O/W nanoemulsion at 3 and 7 T

Samples preparation. First of all the no-loaded and iron oleate complex loaded O/W nanoemulsions were manually resuspended using the pipette and by vortex for a few seconds. Then, dilutions of such samples are prepared at different final concentrations (dilution factors: 1:5, 1:10, 1:20, 1:40, 1:80, 1:160) using Milli Q water. In order to proceed with MRI measurements, dilutions were prepared inside wells of a Cell culture plate (24 wells), taking appropriate volumes of nanoemulsions from the stock solutions and adding Milli Q water up to the volume of 2 mL for each well. In order to obtain a homogeneous distribution within the wells, the solutions were manually resuspended with the pipette.

MRI analysis. The study of the relaxivity of the O/W nanoemulsion containing iron oleate complex was conducted both at clinical field strength (3 T) and high magnetic field (7 T). For the 3 T study, the plate containing the nanoemulsions in aqueous solution was placed in the center of the bore of the clinical scanner (GE HDxT, GE Healthcare, USA). Acquisitions was made using a commercial coil of head coil type (GE HDxT, GE Healthcare, USA) for neurological imaging. For the measurement

of relaxation times it was used respectively Fast Spin Echo Inversion Recovery sequences for the measurement of T_1 and T_2 map Spin Echo for T_2,[4-6] with the following acquisition parameters:

- *T_1 inversion recovery*: FOV = 16 cm; slice thick = 5 mm; 2NEX; 256x256; TR = 8 s; TE = 7ms; Echo Train Length = 24; Bandwidth = 62.5; inversion times (TI) = 50, 100, 300, 500, 700, 900, 1100, 1300, 1500, 1700, 1900, 2100, 2500 ms
- *T_2 map spin echo*: FOV = 16 cm; slice thick = 5 mm; 2NEX; 256x256; TR = 8 s; Echo Train Length = 24; Bandwidth = 62.5; Echo Times (TE) = 10, 20, 40, 60, 80, 100, 160, 200 ms

The images obtained were analyzed with the Matlab software (the Mathword Inc.).

For the 7 T study, the previously analysed iron oleate loaded nanoemulsions solutions were transferred in 5 mm diameter NMR glass tubes, in turn inserted into a larger tube (diameter = 30 mm), in order to acquire more solutions at the same time. Acquisitions were carried out with a NMR Bruker AVANCE III 7-T wide bore (Bruker, Rheinstetten, Germany) 300 MHz spectrometer, operated by the ParaVision 6.0.1.software. The images were acquired using a 30 mm diameter microimaging quadrature coil (Bruker, Rheinstetten, Germany).

FAIR RARE sequences for the measurement of T_1 and Spin Echo (MSME) for T_2 were used respectively for the measurement of relaxation times, with the following acquisition parameters:

- *FAIR RARE*: FOV = 29x29 mm; slice thick = 2 mm; 4 NEX; 256x256; TR = 5 s; TE = 45 ms; Echo Train Length = 16; inversion times (TI) = 50, 200, 350, 500, 650, 800, 950, 1100, 1250, 1400, 1550, 1700 ms, flat resolution = 113x113 μm.
- *MSME*: FOV = 30x30 mm; slice thick = 2 mm; 2 NEX; 256x256; TR = 5 s; Echo Times (TE) = da 8 a 1600 ms con ΔTE = 8 ms, flat resolution = 117x117 μm.

Post Processing of images.

The images obtained at 3 T were analysed with the Matlab software (the Mathword Inc.) in the following procedure:

a) On MRI images, a region-of-interest (ROI) is selected for each nanoemulsion dilution value and the average value of the signal within the ROI is estimated;
b) The value of T_1 is estimated by the fit of the curve of the average signal in ROI as a function of the TI, according to the following equation: $M=M0*(1-2*exp(-TI/T_1))+c$, where M indicates the signal value;
c) The value of T_2 is estimated by the fit of the curve that shows the average of the signal in the ROI according to the different times of eco (TE) used during the acquisitions, according to

the following equation: $M=M0*exp(-TE/T_2)+c$, where M indicates the signal value (Figure 1).

The same approach was followed for the analysis of the images obtained at 7 T, using the ParaVision software.

Once obtained the values of T_1 and T_2 for the different dilution values, some parameters representative of the relaxometric capacities and of the transverse (r_2) and longitudinal relaxivity (r_1) can be estimated by the slope of the regression R_i line compared to nanoemulsions volumes for each dilution, according to the equation: $R_i - R_i(H_2O) = r_i * V, \quad i = 1, 2$, where R_i is the relaxation rate (= 1/Ti) and V is the volume in µL.

We cannot talk about real relaxation values because the latter are obtained from the slope of the regression line $R_{1,2}$ [s^{-1}] compared to the concentration values of Fe-equivalent [in mM], they are in fact expressed in units of $mM^{-1} \cdot s^{-1}$.[7,8] In this preliminary analysis, ICP measurements to evaluate Fe concentration value are in progress, so not having the concentration values, we use a representative parameter.

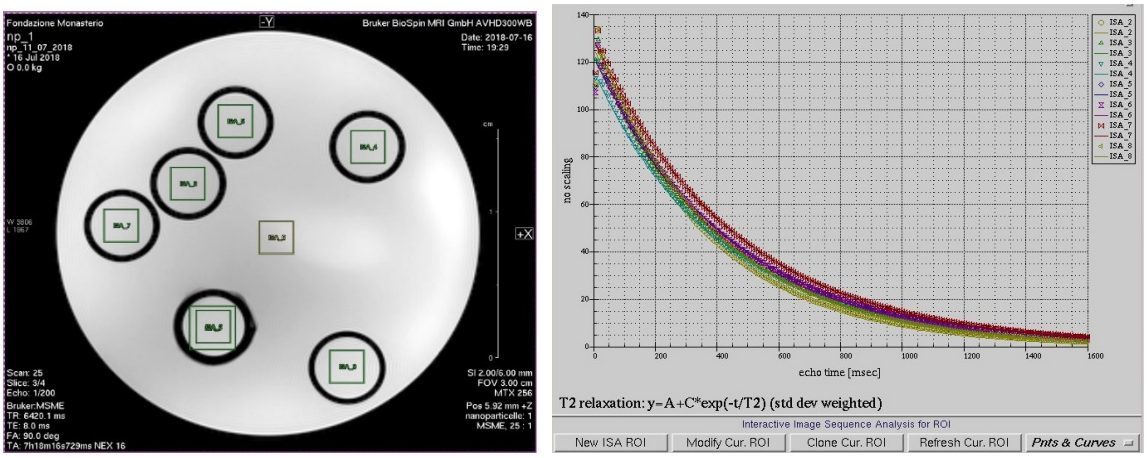

Figure 1: Analysis of the MRI images at 7 T for the estimation of the transverse relaxation time (T_2).

Preliminary MRI results.

Figure 2 shows the fit of the R_2 (s^{-1}) curves according to the nanoemulsions (NE) volume in the solution (in µL) for both the no-loaded and iron oleate complex loaded nanoemulsions; for the fitting it was eliminated the first value of TE (probable saturation).

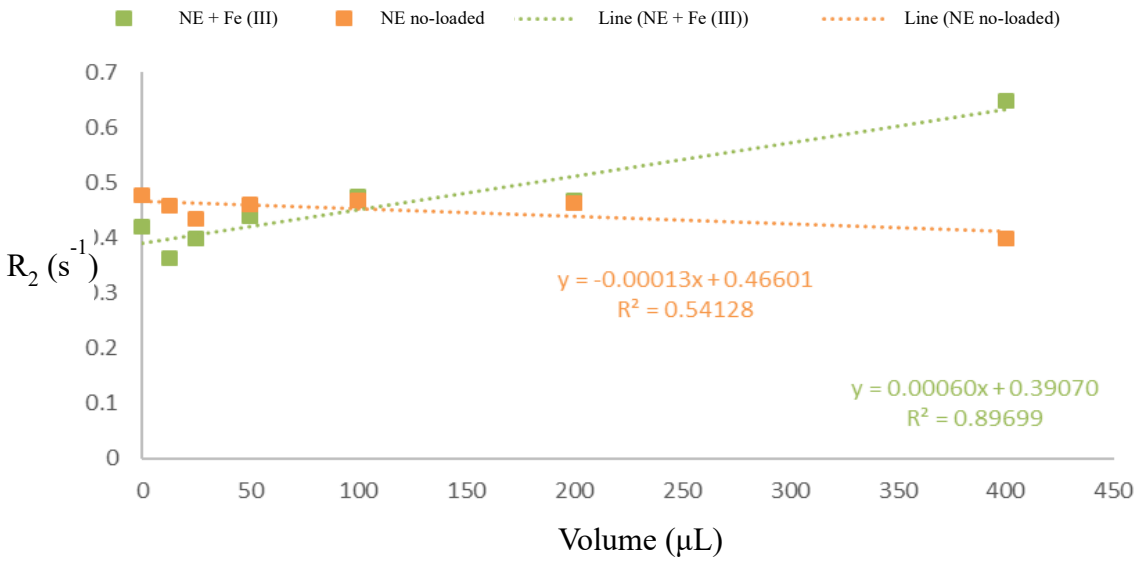

Figure 2. Fit of the trasversal-relaxation curves R_2 according to the nanoemulsions volume in the solution, obtained at 3 T for the non-loaded and iron oleate complex loaded O/W nanoemulsions.

It is observed that nanoemulsions called no-loaded have no effect on the relaxation T_2 while the iron oleate loaded nanoemulsions seem to have an effect on the relaxation T_2. To be able to correctly estimate the value of relaxivity and compare it to that of other commercial systems or similar, it would be necessary to have the Fe equivalent concentration values of the nanoemulsions.

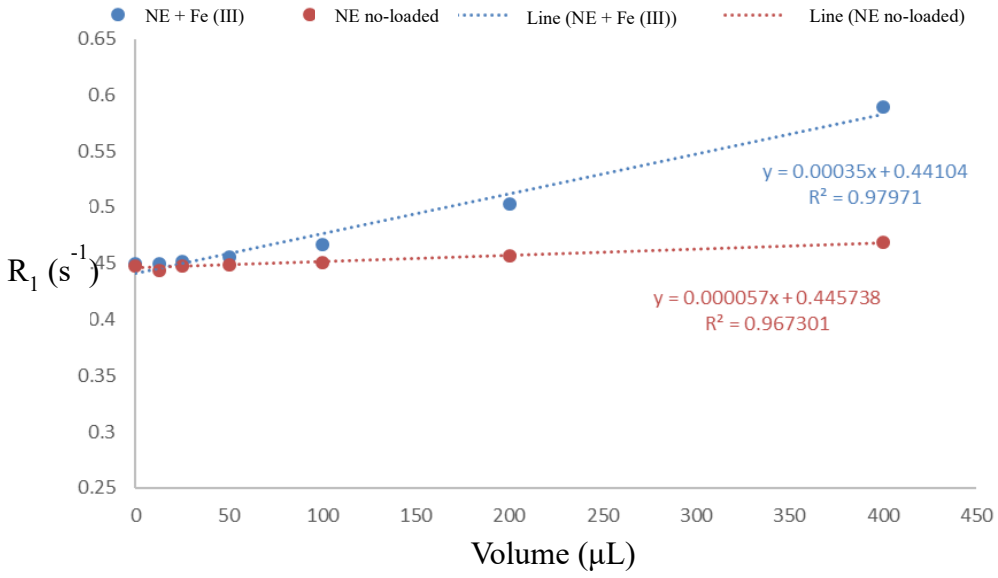

Figure 3. Fit of the longitudinal relaxation curves R_1 as a function of the nanoemulsions volume in the solution, obtained at 3 T for no-loaded and iron oleate loaded nanoemulsions.

Figure 3 shows the fit of the R_1 (s^{-1}) curves according to the nanoemulsions volume in the solution (in µL) for both the no-loaded and iron oleate complex loaded nanoemulsions. Also in this case it is

observed that nanoemulsions called no-loaded have no effect on the T_1 relaxation while the iron oleate complex loaded systems have an effect on the relaxation T_2 leading to a reduction of the T_1 relaxation time to the increase of the concentration. In this case it would be advisable to have the Fe equivalent concentration values of the nanoemulsions to be able to correctly estimate the value of relaxivity.

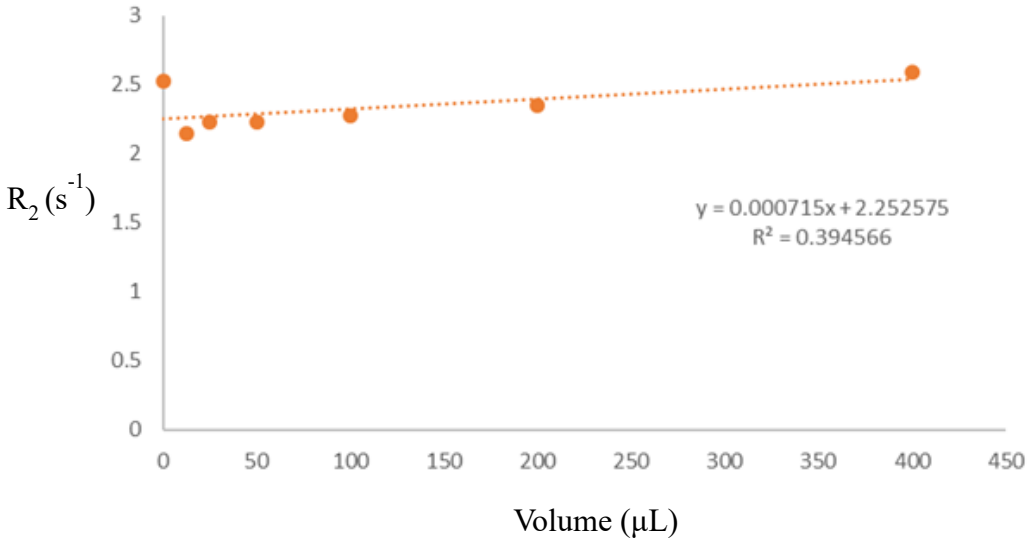

Figure 4. Fit of the trasversal relaxation curve R_2 as a function of the nanoemulsions volume in the solution, obtained at 7 T for the iron oleate complex loaded nanoemulsions.

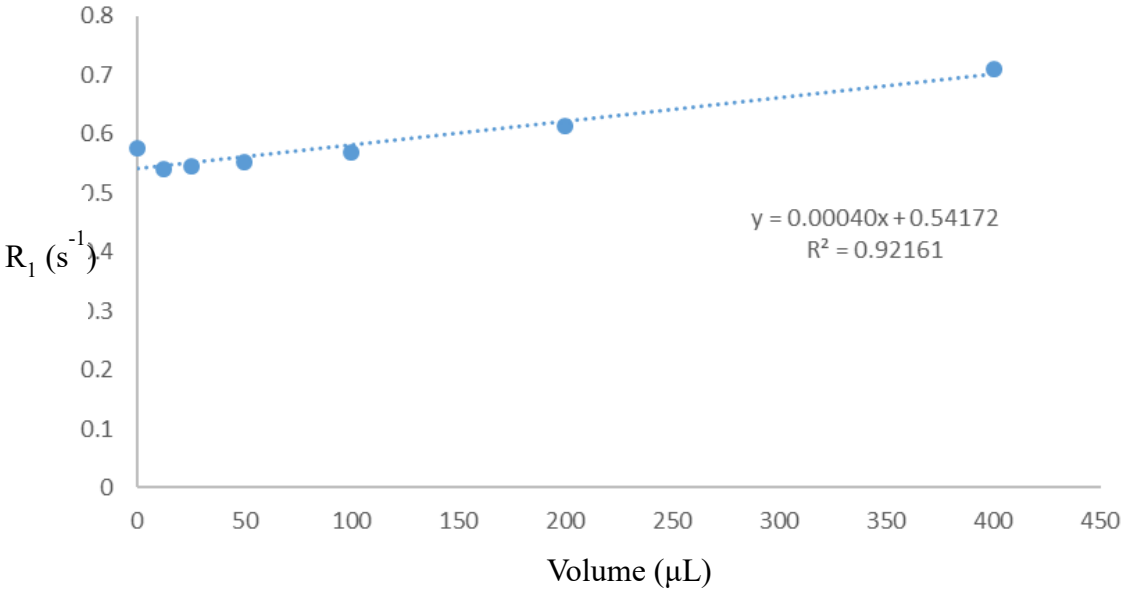

Figure 5. Fit of the longitudinal relaxation curve R_1 as a function of nanoemulsions volume in the solution, obtained at 7 T for the iron oleate complex nanoemulsions.

The fit of the lines of R_2 and R_1 respectively as a function of nanoemulsions volume in the solution (in μL) for the iron oleate complex loaded nanoemulsions are shown in Figure 4 and 5, for the images obtained at 7 T. These graphs substantially confirm the observed trend for 3 T acquisitions, with a decrease in the time of relaxation T_1 and T_2 as the concentration of nanoemulsions increases.

Conclusion

For MRI application, we have started studying a new contrast agent, synthesising molecule of ferric oleate which are soluble in soybean oil, safe and economic. In this way, we have the possibility to increase the Fe(III) concentrations in our O/W nanoemulsion and to scale their size to improve Fe(III) bioavailability. Nanoemulsion and ferric oleate characterizations are in progress, being this a new strategy started very recently. Meanwhile, we have started preliminary MRI analysis to evaluate if these nanocarriers could be interesting systems in such applications. We have observed that in general there is an increase of the values of r_1 and r_2 at 7 T compared to 3 T and the ratio between the parameters is comparable for the two magnetic field intensities employed. In general, for paramagnetic nanostructured systems, such as nanoparticles with magnetite cores, we expect a linear increase in the values of the relaxation rate as the concentration increases, particularly with regard to R_2. ICP analysis and O/W nanoemulsion with higher ferric concentrations are in phase of preparation. The aim is to obtain systems with ratio r_2/r_1 greater than 10.[9] Therefore, our systems seems to be promising.

References

1. Lyudmila M. Bronstein et al., *Chem. Mater.,* **2007**, 19, 3624-3632.
2. Jongnam Park at al., *Nature Materials*, **2004**, 3.
3. R. Vecchione, U. Ciotola, A. Sagliano, P. Bianchini, A. Diaspro and P. A. Netti, *Nanoscale*, **2014**, 6, 9300-9307.
4. I. Monaco, P. Armanetti, E. Locatelli, A. Flori, M. Maturi, S. Del Turco, L. Menichetti and M. Comes Franchini, *J. Mater. Chem. B*, **2018**, 6, 2993.
5. Piccionello, A.P., Menichetti, L., Armanetti, P. et al., *J Nanopart Res,* **2018,** 20:259.
6. A. Boni, G. Bardi, A. Bertero, V. Cappello, M. Emdin, A. Flori, M. Gemmi, C. Innocenti, L. Menichetti, C. Sangregorio, S. Villa and V. Piazza, *Nanoscale*, **2015**, 7, 7307.
7. S. Laurent et al., *Chemical reviews*, **2008**, 108(6), 2064-2110.
8. Na, H. Bet al., *Advanced materials*, **2009**, 21(21), 2133-2148.
9. Carver et al. *Chemical Reviews*, **1999**, 99(9), 2295.

Chapter 5

Conclusions

Nanomedicine is the field of action of this PhD project with particular attention to cancer therapy and prevention. In particular, we focused on drug delivery systems, as photo-stimuli responsive oil core polymer nanocapsules built via LbL technique. Moreover, the encapsulation in the oil core of drugs or contrast agents expand the use of these nanocarriers in specific therapeutic or diagnostic fields. At the same time, the synergistic use of photo-stimuli responsive loaded both with drugs and contrast agents open the door for interesting engineered nanocapsules for theranostic purpose. As discussed previously, LbL nanocarriers are of particular interest to reduce side effects and improve drug efficiency and bioavailability. Moreover, another strong point is the use of safe materials in our preparations in terms of biocompatible polymers, natural drugs and safe contrast agents reducing much more the undesirable effects for the patient. Additionally, the functionalized polymers have never shown toxicity and so seem to be in accordance with our biocompatible systems.

As explained in 'Aim of the PhD project' (Chapter 1) to improve clinical performance and cancer detection, we have manipulated our oil core LbL multilayer shell by chemical modifications in the polymeric compositions and/or in the oil core formulations.

Therefore, in **Chapter 2** we have reported the fabrications and the functionality of cross-linked photo-responsive LbL trilayer built on oil in water nanoemulsions, loaded with a natural drug, curcumin. In particular, we performed a chemical functionalization of the polymers of the shell, to engineer a photo-responsive nanocarrier with *spatio-temporal* control in the release of the drug. Starting from a biocompatible photoinitiator free '*click'* reaction, already demonstrated in our group, we have stabilized our nanocarriers by a cross-linkage between an allylated heparin and a N-acetyl cysteine-*o*-nitrobenzyl moiety on glycol chitosan. In different tests, including viability tests on melanoma cells, we also demonstrated that the photo-responsive moiety permits a nanocarriers' destabilization by UV light and a more efficient release of the drug. This maybe a promising approach for the treatment of cancer skin or for the treatment of cancer tissues during surgery applications. On the other hand, in terms of use of natural drugs but in the field of oral delivery, in **Chapter 3** we reported our recent published article, which is part of this PhD project. In this work, we studied curcumin and lycopene loaded in O/W nanoemulsions coated or no coated with chitosan. *In vitro* tests on cardiomyoblasts in presence of doxorubicine has demonstrated the cardioprotection and anti-inflammatory activity of these nutraceutical drugs.

As pure diagnostic application of our O/W nanoemulsions, in **Chapter 4** we reported a study on oil-core-PEG shell nanocarriers encapsulating nanocubic iron oxide nanoparticles, as safe contrast agent. We have demonstrated their goodness in *in vitro* photoacoustic and *in vitro* and *in vivo* magnetic resonance imaging. Moreover, in the **Appendix** to Chapter 4, we showed a new approach that we are developing. It is about the use of a molecule, safe and economic, as contrast agent, ferric oleate and

in this Appendix we reported the preliminary data about simple synthesis, its loading into our nanoemulsions and the first MRI results. This is also an approach meant to allow scaling down of the size of our oil core nanocarrier since in this way the nanocarrier size is not limited by the size of contrast agents in nanoparticle version.

On one hand, each part of this PhD project could be a single tool to apply in a single field but on the other hand, all the tools may be combined in a very flexible and open-minded way. We may think to induce a specific route of our nanocarrier in the desired diseased tissue by magnetic field or just wait a spontaneous accumulation; we could follow the nanocapsules accumulation by MRI, and induce a controlled release by a light external source. Furthermore, the cross-linkage of our nanocapsules can guaranty stability and no loss of their cargo, until they arrive in the specific sites. Engineering a photo-responsive nanocarrier co-loaded with natural drugs and safe contrast agents, opens the doors to a promising theranostic approach. In the next future, our purpose is the preparation of those theranostic nanocapsules to prove *in vitro* ad *in vivo* their efficiency.